

Full-shape analysis with simulation-based priors: cosmological parameters and the structure growth anomaly

Mikhail M. Ivanov,^{1,*} Andrej Obuljen,² Carolina Cuesta-Lazaro,^{3,4,5,†} and Michael W. Toomey^{1,‡}

¹*Center for Theoretical Physics, Massachusetts Institute of Technology, Cambridge, MA 02139, USA*

²*Department of Astrophysics, University of Zurich,
Winterthurerstrasse 190, 8057 Zurich, Switzerland*

³*The NSF AI Institute for Artificial Intelligence and Fundamental Interactions, Cambridge, MA 02139, USA*

⁴*Department of Physics, Massachusetts Institute of Technology, Cambridge, MA 02139, USA*

⁵*Center for Astrophysics — Harvard & Smithsonian,
60 Garden Street, MS-16, Cambridge, MA 02138, USA*

We explore full-shape analysis with simulation-based priors, which is the simplest approach to galaxy clustering data analysis that combines effective field theory (EFT) on large scales and numerical simulations on small scales. The core ingredient of our approach is the prior density of EFT parameters which we extract from a suite of 10500 galaxy simulations based on the halo occupation distribution (HOD) model. We measure the EFT parameters with the field-level forward model, which enables us to cancel cosmic variance. On the theory side, we develop a new efficient approach to calculate field-level transfer functions using *time-sliced perturbation theory* and the logarithmic fast Fourier transform. We find that the cosmology dependence of EFT parameters of galaxies is approximately degenerate with the HOD parameters, and hence it can be ignored for the purpose of prior generation. We use neural density estimation to model the measured distribution of EFT parameters. Our distribution model is then used as a prior in a reanalysis of the BOSS full-shape galaxy power spectrum data. Assuming the Λ CDM model, we find significant ($\approx 30\%$ and $\approx 60\%$) improvements for the matter density fraction and the mass fluctuation amplitude, which are constrained to $\Omega_m = 0.315 \pm 0.010$ and $\sigma_8 = 0.671 \pm 0.027$. The value of the Hubble constant does not change, $H_0 = 68.7 \pm 1.1$ km/s/Mpc. This reaffirms earlier reports of the structure growth tension from the BOSS data. Finally, we use the measured EFT parameters to constrain the galaxy-dark matter connection.

1. INTRODUCTION

The nature of dark matter, dark energy, and the origin of the Universe (cosmic inflation) remain some of the greatest puzzles of fundamental physics. Ongoing and future galaxy surveys such as DESI [1], Euclid [2], LSST [3], and Roman Space Telescope [4] aim to deliver data that can shed light on these mysteries. However, extracting information from the maps of our Universe created by these surveys will not be an easy task. It will require a detailed understanding of structure formation in the non-linear regime.

Historically, there have been two leading approaches to this problem. The first one relies on cosmological perturbation theory, which proved to be extremely successful in

the description of cosmological fluctuations in the linear regime. The non-linear extension of cosmological perturbation theory relevant for structure formation have been developed over the last fifty years [5]. Most recently, this program culminated with the development of the effective field theory of large scale structure (EFT) [6–8]. EFT provides a systematic and consistent program to describe galaxy clustering on scales larger than few Megaparsecs. The main practical advantages of EFT are its low computational cost and flexibility. This made it a useful tool for tests of the standard cosmological model¹ and its various extensions with full-shape analyses of galaxy clustering data from BOSS and DESI, see e.g. [9–14].

Powerful as it is, EFT has important limitations. First, it breaks down on small scales, which contain signifi-

* ivanov99@mit.edu

† cuestalz@mit.edu

‡ mtoomey@mit.edu

¹ Based on the cosmological constant Λ and cold dark matter (CDM), Λ CDM.

cant information as measured by the number of Fourier modes. Second, even on large scales, the EFT predictions depend on a large number of free (nuisance) parameters, which have to be marginalized over in order to obtain cosmological constraints. The number of free parameters proliferates as one pushes to higher orders in perturbation theory, see e.g. [15–17]. This leads to a significant degradation of constraining power. In particular, the constraints on single field inflation degrade by orders of magnitude due to the degeneracy between EFT nuisance parameters and the physical inflationary signal [18–20]. On the one hand, the EFT provides the most conservative framework that is absolutely agnostic about galaxy formation. On the other hand, this approach ignores years of intense theoretical and observational efforts that significantly improved our understanding of galaxy formation. The rapid progress in this field is evidenced by the success of numerical simulations to model galaxies, see e.g. with the EAGLE, IllustrisTNG and MillenniumTNG simulations [21–23].

This brings our discussion to the second approach to model the cosmic web: numerical simulations. For pure dark matter clustering, numerical simulations provide a complete first principle solution to the problem of cosmological structure formation. In particular, the N-body simulations show that the collapse of matter leads to the formation of dark matter halos. However, the key challenge is to describe the observed luminous objects, such as galaxies, for which the first principle models may not be available. A number of approaches, ranging from theoretical to purely empirical, have been proposed, see [24] for a review. In this work, we focus on the halo occupation distribution (HOD) framework [25–28]. The HOD models are based on a well established fact that galaxies reside inside dark matter halos. The HOD then assigns galaxy positions based on the matter distribution within dark matter halos. From the EFT perspective, the HOD provides an ultraviolet (UV) complete galaxy clustering model, which is formally applicable even on small scales.

Extracting information from large-scale structure data with simulations is part of a general “simulation-based inference” (SBI) approach of fitting data without explicit analytic models. Various HOD-based SBI pipelines have been successfully tested in blind challenges [29] and applied to actual data, see e.g. [30–34]. This success raises the questions: How to improve EFT by incorporating galaxy formation information [35–37]? And how to com-

bine the benefits of both EFT and SBI [38, 39]?²

In this work, we pursue possibly the simplest and least computationally expensive way to combine EFT and SBI: use simulation-based priors in EFT analysis [35–37, 44]. In particular, we use priors based on HOD models, as this approach offers great flexibility in galaxy modeling at a very modest computation cost (as compared e.g. to the hydrodynamic simulations).

A typical HOD model uses $O(10)$ parameters to describe the clustering of galaxies in redshift space on all scales. However, the EFT power spectrum model depends on roughly the same number of parameters already at next-to-leading (one-loop) order. Formally, EFT expansion involves an infinite number of parameters. Hence, if one assumes that the HOD is a true underlying model, the EFT parameters must be highly correlated. These correlations should bring additional information that can improve usual EFT full-shape analyses.

A useful analogy here is provided by nuclear physics. The strong interaction at low energies is described by chiral perturbation theory (ChPT) (see e.g. [45, 46] for reviews). Being an EFT, ChPT at any given order formally depends on many unknown low energy constants. One can match these constants from UV complete models. A textbook example is given by matching ChPT to the linear sigma model, which produces tight constraints on combinations of ChPT parameters. More realistic examples are provided by matching ChPT to results of numerical lattice simulations (see e.g. [47–49] and references therein) or bootstrap calculations [50, 51], based on UV complete quantum chromodynamics (QCD). In this context, an HOD model with some free parameters is equivalent to a QCD model whose free parameters are the gauge group, coupling constant, quark flavors and masses.

Our approach follows the one outlined by us in ref. [36]. There, we have produced HOD-based priors for EFT parameters, and applied them to the search of single field inflation primordial non-Gaussianity (PNG) in the BOSS data. There are two simplifications that take place in this particular analysis. First, the underlying cosmological parameters of Λ CDM are kept fixed, which is customary in PNG searches [52]. Second, the PNG constraints de-

² In some sense, this question is addressed in phenomenological hybrid EFT models [40–43]. In our work, however, we apply EFT strictly within the range of its mathematical validity.

pend primarily on the bias parameters in real-space (i.e. in the galaxy rest frame) [18, 19, 53]. Given these reasons, the HOD-based priors of ref. [36] were produced for a fixed cosmology and only in real space. In this work we go beyond these simplifications. We derive priors on EFT parameters in redshift space, and also study its cosmology dependence (although eventually we find it to be negligible for the purpose of EFT prior generation). This allows us to explore the sensitivity of the full-shape analysis to priors on redshift space counterterms. This is especially relevant in the context of the structure growth tension, i.e. the discrepancy between the measurements of the mass fluctuation amplitude parameter σ_8 (or the lensing parameter $S_8 = (\Omega_m/0.3)^{0.5}\sigma_8$) between cosmic microwave background and large-scale structure, e.g. in Baryon Oscillation Spectroscopic Survey (BOSS) data [54]. Some evidence for low σ_8 has been reported by several independent analyses of galaxy clustering data [9, 11–13, 55–59], see however [30, 32, 60–62].

Our paper is structured as follows. We start with a summary of main results in Sec. 2. Then we discuss the simulations that we use here in Sec. 3. The details of our field-level EFT technique and the theoretical calculations are presented in Sec. 4. Section 5 presents our study of the cosmology dependence of dark matter halos, and the final distribution of EFT parameters from the HOD. There we also discuss the modeling of the EFT parameter density with machine learning tools. Section 6 describes the re-analyses of the BOSS galaxy clustering data with our HOD-based priors. Sec. 7 draws conclusions. Details of our theoretical calculations and additional tests are reported in appendices.

2. MAIN RESULTS

The key goal of our paper is to produce a distribution of EFT parameters from galaxy formation simulations that can be used as a prior in EFT-based full-shape analyses. We focus on the HOD-based models here, noting that our approach is more general and in principle can be applied to other types of simulations.

We produce a large sample of mock galaxy catalogs and extract their EFT parameters. We use neural density estimators called normalizing flows to obtain a model for the resulting distribution of EFT parameters that can accurately capture intricate correlations between them.

Finally, we apply this priors in the actual analysis of publicly available galaxy clustering data.

In the process of producing simulation-based priors, we have resolved a number of theoretical and practical problems, which are summarized in this Section, together with our key discoveries and results.

1. Redshift space field-level transfer functions.

We use the field-level technique to measure EFT parameters from simulated galaxy catalogs. Specifically, we use the field-level EFT model of [63, 64] based on transfer functions and the shifted operators (see also refs. [38, 65] for the application to HI maps, and [40, 66–76] for additional references on field-level EFT). The field-level method allows for cosmic variance cancellation, and hence a precision measurement of EFT parameters from computationally cheap small box simulation. To measure the EFT parameters, we need to fit the shape of the field-level transfer functions. Specifically, we are mostly interested in the transfer function of the matter density field β_1 , which contains the bulk of the information on the EFT parameters. Schematically, the latter is defined as

$$\delta_g(\mathbf{k})\Big|_{\text{EFT, field-lvl}} = \beta_1(\mathbf{k})\tilde{\delta}_1(\mathbf{k}) + \dots, \quad (1)$$

where $\tilde{\delta}_1$ is the shifted linear density field,³ δ_g is the forward model, while the above dots stand for higher order operators. The model (1) is a simple extension of the linear galaxy bias model $\delta_g = b_1\delta_1$. However, in eq. (1) b_1 is promoted to be a scale-dependent transfer function in order to capture higher order corrections (cubic operators and counterterms). The typical galaxy density snapshots in real space and redshift space, as well as the best-fit field-level EFT models and the residuals between them are shown in fig. 1. These are generated with the publicly available code `Hi-Fi mocks`⁴.

The one-loop perturbation theory predictions for β_1 in real space have been derived in ref. [63]. In this work, for the first time, we calculate the one-loop model for the redshift space generalization of β_1 proposed in [64]. Although the initial model of [64] is formulated in Lagrangian space, we carry out our calculation in Eulerian

³ i.e. the linear density field shifted by the linear Zel’dovich displacement, see Section 4 for more detail.

⁴ https://github.com/andrejobuljen/Hi-Fi_mocks

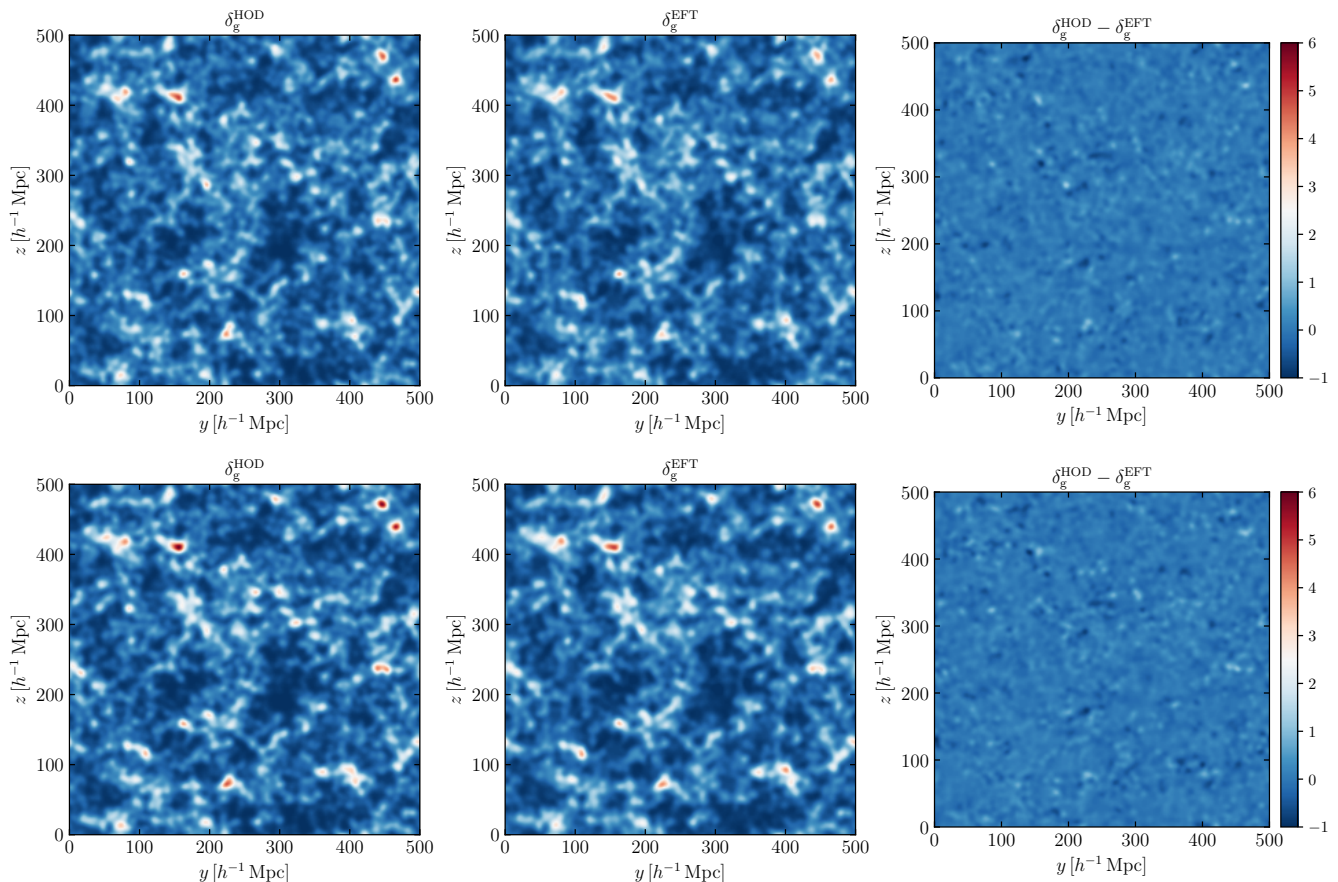


FIG. 1. A typical HOD mock galaxy distribution in real space (upper panel) and redshift space (lower panel) from our set (left), field-level EFT fit to it (center), and the residuals (right). The overdensity field has been smoothed with a $R = 4 h^{-1} \text{Mpc}$ 3D Gaussian filter, the depth of each panel is $\approx 60 h^{-1} \text{Mpc}$, while the redshift space distortions are along the z -axis.

space, which is more directly connected to physical observables.

2. Efficient theoretical computation of field-level transfer functions. The redshift-space model for β_1 uses shifted operators that are defined in Lagrangian space using the Zel'dovich displacements. Thus, the most natural setup for their calculation is Lagrangian perturbation theory [63]. This approach, however, is relatively expensive in terms of computational time and makes it hard to connect the field-level results with Eulerian EFT codes such as CLASS-PT [77]. The computation speed is crucial for one of our main goals here: the application of EFT to a large ensemble of cosmological models. To overcome these problems, we develop an equivalent, but more computationally efficient way to obtain all necessary one-loop corrections to β_1 in redshift space in ~ 1 second per CPU per single cosmological model. Our approach is based on the fact that Lagrangian perturbation theory is

equivalent to infrared (IR) resummed Eulerian perturbation theory. The latter can be efficiently formulated with *time-sliced perturbation theory* (TSPT) [78–81].

TSPT is a formulation of EFT which makes manifest the IR safety of Eulerian correlation functions and allows for an efficient description of the non-linear evolution of baryon acoustic oscillations (BAO), known as IR resummation [82–84]. We use TSPT to resum the IR displacements in the Eulerian expansion for the shifted correlation functions. As a result, we obtain an expression that accounts for the non-linear BAO and that can be easily evaluated with the standard tools of Eulerian perturbation theory loop integrals, such as the logarithmic Fast Fourier Transform (FFTLog) [77, 85]. As an example, we develop an external module for the CLASS-PT code that evaluates the TSPT expressions for shifted power spectra in redshift space. This model plays a central role in our exploration of the cosmology dependence of EFT

parameters.

3. Cosmology dependence of EFT parameters for dark matter halos. We extract EFT parameters of dark matter halos for 2000 cosmological Λ CDM models simulated within the Quijote project [86]. These samples include, for the first time, redshift space EFT counterterms and redshift-space stochastic contributions. We have found that EFT parameters depend on cosmology mostly through the “peak height” parameter $\nu = \delta_c/\sigma_M(z)$, where $\delta_c \approx 1.686$ is the spherical collapse threshold overdensity, and σ_M^2 is the mass variance at the Lagrangian size of the halo of mass M . This dependence can be understood as a consequence of the approximate universality of the halo mass function.

As a result, the cosmology dependence is approximately degenerate with the halo mass. In particular, simulation-based correlations between EFT parameters, e.g. functions $b_2(b_1)$ etc., are nearly cosmology-independent as the variation of σ_M^2 that produces them can be mimicked with an appropriate variation of M .

4. Cosmology dependence of EFT parameters for galaxies. In the HOD models, the EFT parameters of galaxies are derived from those of halos assuming an HOD. In particular, the galaxy bias parameters are given by integrals over the halo mass function weighted by the HOD [87, 88]. We have found both analytically and numerically that the cosmology dependence encoded by the HMF can be approximately absorbed by modest shifts of the basic HOD parameters [27] such as the minimal halo mass to host a central galaxy. Since the cosmology dependence of EFT parameters of galaxies is approximately degenerate with the HOD parameters, it can be accounted for by choosing wide enough prior ranges.

In addition, we have found that the variation of parameters of the “decorated” HOD models [28] produces a much wider spread of the EFT parameter distribution than the variation of cosmology and the basic HOD parameters. This makes the distribution of EFT parameters sampled from HOD models largely cosmology-independent.

We have done additional checks of the cosmology-independence of the HOD-based EFT parameter distribution. These include an explicit comparison of our priors with EFT samples from two different cosmologies, and tests of our priors on PT Challenge simulations [89] based on a cosmology different from the one used to generate our priors.

Our analysis implies that our HOD-based priors can be used to analyze extensions of Λ CDM, which alter structure formation primarily via the underlying linear matter power spectrum, e.g. spatial curvature, dynamical dark energy [90], and models with modified pre-recombination histories [91–94].⁵

5. EFT parameters for HOD galaxies. We have generated a sample of EFT parameters from 10,500 HOD models that match the properties of luminous red galaxies (LRGs). We assume flat wide priors on HOD parameters in our sampling procedure. Our sample is the largest and the most complete sample of bias and EFT parameters studied to date. The redshift space EFT counterterms, including the stochastic one, are analysed in detail for the first time.

An important observation is a high degree of correlation between the EFT parameters from HOD models. This is expected as the EFT by definition makes no assumptions about the small scale physics. Hence, strictly speaking, the EFT depends on an infinite tower of free parameters. Thus, within any particular small-scale model, such as the HOD, the EFT parameters inevitably sample some low dimensional parameter space. Importantly, the correlations that we find are different from those that appear when fitting the EFT parameters directly from the power spectrum, bispectrum etc.⁶ Hence, field level simulation-based information efficiently breaks parameter degeneracies, leading to sizeable improvements of parameter constraints.

We have produced an accurate model for the distribution of the EFT parameters with the normalizing flows. This distribution can be used as simulation-based priors (SBP) in actual full-shape analyses of LRG samples from BOSS [54] and DESI [100].

6. Application to BOSS data. We have re-analyzed publicly available redshift space galaxy cluster-

⁵ Note that this approximation works well even in other cases, such as e.g. massive neutrinos [9, 95], ultralight axion [96], and light massive relics [97], where it is the standard practice in EFT analyses to consider only the modification of the linear matter power spectrum and neglect dynamical nonlinear effects due to nontrivial clustering properties. It will be interesting to understand to what extent our priors can be used in these models.

⁶ For instance, the contributions from the stochastic $k^2\mu^2$ operator and the deterministic $k^4\mu^4 P_{11}$ term (P_{11} is the linear matter power spectrum) are degenerate at the galaxy power spectrum level [98, 99], but completely independent at the field level.

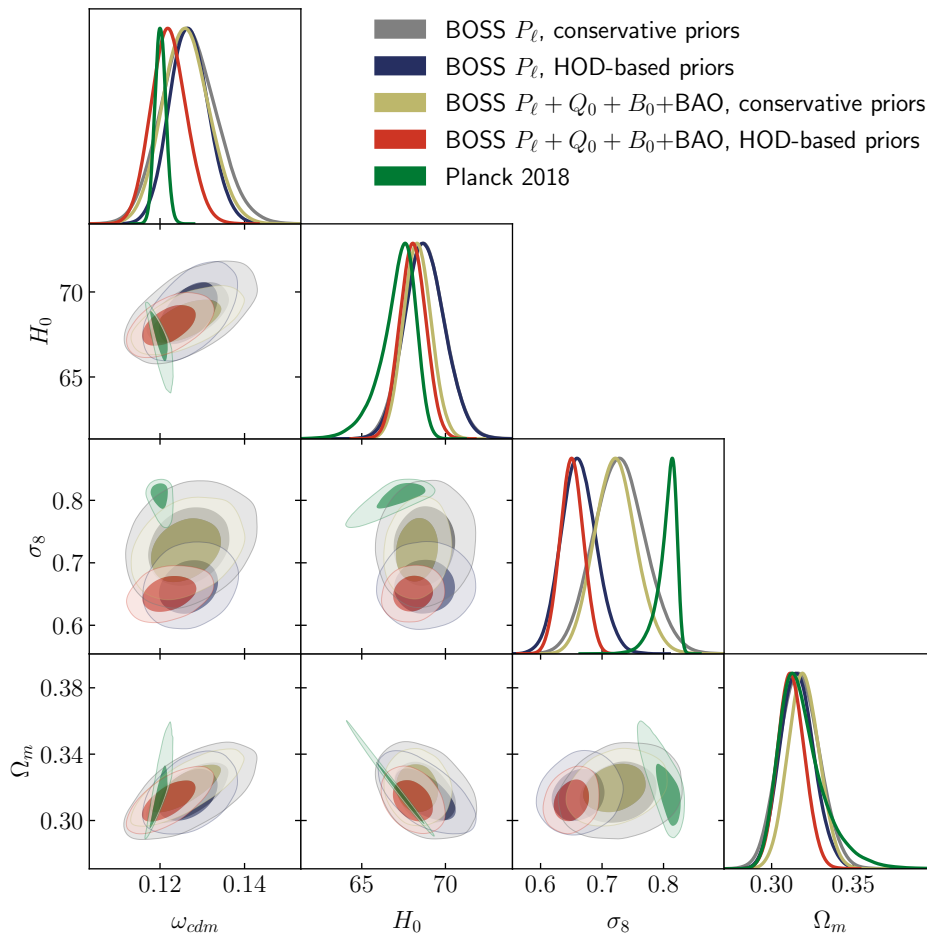


FIG. 2. Cosmological parameters from the EFT-based full shape analysis of the BOSS power spectrum with conservative and informative simulation-based priors on EFT parameters. Additionally, we show results from an extended data vector that includes the real space power spectrum proxy Q_0 , BAO, and the bispectrum monopole B_0 . For comparison, the *Planck* 2018 results for $\Lambda\text{CDM}+m_\nu$ are also shown.

ing data from BOSS DR12 [54] with SBP. Effectively, most of the EFT parameters are then determined by the priors conditioned to information extracted from the data, such as the linear bias b_1 measured from (linear) redshift space distortions. In turn, tighter EFT parameters reduce the freedom in fitting the small scale part of the power spectrum thereby allowing us to extract more cosmological information. As a result, we found significant improvements on σ_8 and ω_{cdm} , by 60% and 30%, respectively, from the power spectrum only analysis. This improvement is equivalent to doubling the survey volume.

Our final parameter estimates are presented in fig. 2. There we show the posteriors of cosmological parameters from three BOSS analyses: the galaxy power spectrum with conservative priors of [12], which is our benchmark, and SBP analyses of the galaxy power spectrum and of

the full BOSS dataset from ref. [12], including the bispectrum monopole, BAO, and the real space power spectrum proxy Q_0 . The *Planck* 2018 constraints are displayed for comparison.

Our analysis confirms earlier reports of the σ_8 tension in the BOSS data, see e.g. [13]. We find the tension nominally at the $\approx 5\sigma$ level from the galaxy power spectrum alone, which is the strongest evidence reported to date. Note that previous analyses such as [13] were performed with uninformative priors on EFT parameters. Therefore, we additionally confirm that the BOSS σ_8 tension is not driven by the choice of priors, see e.g. [11–13] for earlier detailed discussions.

7. Constraining galaxy – dark matter connection from EFT parameters. Our joint sample of EFT and HOD parameters (θ_{EFT} and θ_{HOD} , respectively) can

be used to build a conditional distribution $p(\theta_{\text{HOD}}|\theta_{\text{EFT}})$, allowing one to translate the measured values of EFT parameters from data into HOD parameters. This way one can get insights into the galaxy – dark matter connection using large-scale clustering information. We have implemented this approach in practice using appropriate normalizing flow models for the conditional distribution $p(\theta_{\text{HOD}}|\theta_{\text{EFT}})$. We have obtained constraints on the threshold host halo masses from BOSS, which are consistent with SBI analyses based on HODs e.g. [60]. Notably, in agreement with these works, we have found evidence for environment-based assembly bias of central galaxies in the BOSS data.

8. Implications for the choice of priors in full-shape analyses. Our HOD-based priors are consistent with the conservative priors associated with the CLASS-PT [77] and `velocileptor` [101, 102] codes. This confirms that these priors reflect well both our current understanding of galaxy formation physics and EFT naturalness arguments. In contrast, the priors associated with the `PyBird` code [103] appear to be overoptimistic, which can bias cosmological parameter estimates.

An important observation is that HOD models predict strong correlations between the EFT parameters. It will be interesting to “orthogonalize” the basis of EFT parameters to reflect the physics of HOD parametrizations, or other galaxy formation models, better. This may lead to new insights relevant for the understanding of the physics of galaxy formation.

3. SIMULATIONS

We discuss now the N-body simulations that we use in our work.

Quijote-LH. The first type of simulations we use is a latin-hypercube `Quijote` suite that samples 2000 Λ CDM cosmologies [86]. Each cosmology is sampled from the following flat distributions,

$$\begin{aligned} \Omega_m &\in [0.1, 0.5], & \Omega_b &\in [0.03, 0.07], & h &\in [0.5, 0.9], \\ n_s &\in [0.8, 1.2], & \sigma_8 &\in [0.6, 1.0]. \end{aligned} \quad (2)$$

The neutrino mass is set to zero. Note that these ranges significantly exceed the actual constraints on these parameters coming e.g. from *Planck* [104]. We use the high-resolution `Quijote-LH` suite where in simulation was run with 1024^3 particles. Each box has a site length of 1000

h^{-1} Mpc. We use the snapshots at $z = 0.5$. Note that even the high-resolution `Quijote-LH` suite is limited in terms of resolving low mass halos. In particular, the Rockstar halo catalogs feature a saturation and a cutoff already for $\log_{10}(M_{\text{halo}}/[M_{\odot}/h]) < 13$. The limited resolution is the main reasons why we do not use `Quijote-LH` for the HOD catalog production.

The generation of dark matter halo parameters for a fixed cosmology is done with the fiducial high-resolution `Quijote` simulation.

AbacusSummit small. Our main HOD samples are based on the `AbacusSummit small` [105], or covariance suite, with box site length $500 h^{-1}$ Mpc. Each box was run with 1728^3 particles, which provides an excellent resolution even for small halos. The fiducial cosmology of `AbacusSummit small` is the *Planck* 2018 Λ CDM cosmology [106] with a single massive neutrino of the minimal mass $M_{\nu} = 0.06$ eV. Our baseline redshift is $z = 0.5$ as before. We use halo catalogs computed from the full particle set using the CompaSO halo finder [107].

AbacusSummit base. Additional tests of the cosmology (in)dependence of EFT parameters are done with the `AbacusSummit base` suite. Each box in the suite has 6912^3 particles and $2000 h^{-1}$ Mpc site length. The suite covers 139 different cosmological models. The cosmological models that we use for our validation tests are `abacus_cosm000`, `abacus_cosm003`, and `abacus_cosm004` from <https://abacussummit.readthedocs.io/en/latest/cosmologies.html>. The `cosm003` and `cosm004` cosmologies have $\sigma_8 = 0.86$ and $\sigma_8 = 0.75$, respectively, which allow us to explore a large range of the cosmological parameter most relevant for structure formation.

4. EFT AT THE FIELD LEVEL

In this section, we give a theoretical background on the field-level EFT technique of refs. [63, 64]. The basis for the field level technique is the Eulerian bias model [108, 109],

$$\begin{aligned} \delta_g^{\text{EFT}} \Big|_{\text{n-pf}}(\mathbf{k}) &= b_1 \delta + \frac{b_2}{2} \delta^2 + b_{\mathcal{G}_2} \mathcal{G}_2 \\ &+ b_{\Gamma_3} \Gamma_3 - b'_{\nabla^2 \delta} \nabla^2 \delta + \epsilon, \end{aligned} \quad (3)$$

where δ is the non-linear matter density field, \mathcal{G}_2 is the tidal operator,

$$\begin{aligned} \mathcal{G}_2(\mathbf{k}) &= \int_{\mathbf{p}} F_{\mathcal{G}_2}(\mathbf{p}, \mathbf{k} - \mathbf{p}) \delta(\mathbf{p}) \delta(\mathbf{k} - \mathbf{p}), \\ F_{\mathcal{G}_2}(\mathbf{k}_1, \mathbf{k}_2) &= \frac{(\mathbf{k}_1 \cdot \mathbf{k}_2)^2}{k_1^2 k_2^2} - 1, \end{aligned} \quad (4)$$

$\int_{\mathbf{k}} \equiv \int \frac{d^3 \mathbf{k}}{(2\pi)^3}$ and Γ_3 is the Galileon tidal operator,

$$F_{\Gamma_3} = \frac{4}{7} \left(1 - \frac{(\mathbf{k}_1 \cdot \mathbf{k}_2)^2}{k_1^2 k_2^2} \right) \left(\frac{((\mathbf{k}_1 + \mathbf{k}_2) \cdot \mathbf{k}_3)^2}{(\mathbf{k}_1 + \mathbf{k}_2)^2 k_3^2} - 1 \right). \quad (5)$$

Here and in what follows we use the following notation for a general cubic operator $\mathcal{O}^{(3)}$

$$\mathcal{O}^{(3)} = \int_{\mathbf{k}_1} \int_{\mathbf{k}_2} \int_{\mathbf{k}_3} \left(\prod_{i=1}^3 \delta(\mathbf{k}_i) \right) (2\pi)^3 \delta_D^{(3)}(\mathbf{k} - \mathbf{k}_{123}) F_{\mathcal{O}^{(3)}}. \quad (6)$$

In our forward model we will replace δ in the above integral expressions with the linear matter over-density $\delta_1(\mathbf{k}, z)$, which is appropriate in perturbation theory. $b_1, b_2, b'_{\nabla^2 \delta}, b_{\Gamma_3}$ are Eulerian bias parameters. The field ϵ captures stochastic contributions to the observed galaxy density. By definition, it does not correlate with any perturbative field.

The model (3) requires a proper treatment of bulk flows (IR resummation). At the field level, it means we have to keep the large-scale displacement resummed. If $\delta_1(\mathbf{k}, z)$ is the initial density field, the associated linear Zel'dovich displacement field in Fourier space is given by

$$\psi_1(\mathbf{k}, z) = \frac{i\mathbf{k}}{k^2} \delta_1(\mathbf{k}, z). \quad (7)$$

Note that the power spectrum of δ_1 by definition is the linear matter power spectrum,

$$\langle \delta_1(\mathbf{k}) \delta_1(\mathbf{k}') \rangle = (2\pi)^3 \delta_D^{(3)}(\mathbf{k}' + \mathbf{k}) P_{11}(k). \quad (8)$$

In what follows it will be convenient to use the primed correlators with the Dirac delta function stripped off,

$$\langle \delta_1(\mathbf{k}) \delta_1(\mathbf{k}') \rangle' = P_{11}(k). \quad (9)$$

The field level model for galaxies is obtained by writing down the perturbative bias expansion, and shifting all terms in it by the Zel'dovich displacement. The corresponding perturbative operators are dubbed ‘‘shifted’’ and denoted with tildas. In real space they are given by

$$\tilde{\mathcal{O}}_{\text{real}}(\mathbf{k}) = \int d^3 \mathbf{q} \mathcal{O}(\mathbf{q}) e^{-i\mathbf{k} \cdot (\mathbf{q} + \psi(\mathbf{q}))}. \quad (10)$$

In redshift space, one has to add an additional displacement along the line of sight \hat{z} ,

$$\tilde{\mathcal{O}}(\mathbf{k}) = \int d^3 \mathbf{q} \mathcal{O}(\mathbf{q}) e^{-i\mathbf{k} \cdot (\mathbf{q} + \psi(\mathbf{q}) + f \hat{z}(\psi(\mathbf{q}) \cdot \hat{z}))}, \quad (11)$$

where $f = d \ln D_+ / d \ln a$ is the logarithmic growth factor, D_+ is the growth factor and a is the metric scale factor. Note that our model with the exponentiated Zel'dovich field is equivalent to IR resummed Eulerian or Lagrangian EFT.

Another important ingredient of the forward model is the orthogonalization of the relevant operators. Without orthogonalization, we have large operator mixing effects that make the measurements of bias parameters at the field level strongly cutoff-dependent. In order to reduce operator mixing, following [63, 64, 68] we use the orthogonalized operators \mathcal{O}_a^\perp that satisfy

$$\langle \mathcal{O}_m^\perp \mathcal{O}_n^\perp \rangle = 0 \quad \text{if } n \neq m. \quad (12)$$

Once the set of operators is determined, they are orthogonalized using the Gram-Schmidt procedure. For instance, the first three generic operators $\mathcal{O}_1, \mathcal{O}_2, \mathcal{O}_3$ are orthogonalized as

$$\begin{aligned} \mathcal{O}_1^\perp &= \mathcal{O}_1, \\ \mathcal{O}_2^\perp &= \mathcal{O}_2 - \frac{\langle \mathcal{O}_2 \mathcal{O}_1 \rangle'}{\langle \mathcal{O}_1 \mathcal{O}_1 \rangle'} \mathcal{O}_1, \\ \mathcal{O}_3^\perp &= \mathcal{O}_3 - \frac{\langle \mathcal{O}_3 \mathcal{O}_1 \rangle'}{\langle \mathcal{O}_1 \mathcal{O}_1 \rangle'} \mathcal{O}_1 - \frac{\langle \mathcal{O}_3 \mathcal{O}_2^\perp \rangle'}{\langle \mathcal{O}_2^\perp \mathcal{O}_2^\perp \rangle'} \mathcal{O}_2^\perp. \end{aligned} \quad (13)$$

The operators that we will use are those that appear in the perturbative bias expansion. Explicitly, our field-level model will depend on the set of operators

$$\{1, \delta_1, \delta_2 \equiv \delta^2 - \sigma_1^2, \mathcal{G}_2, \delta_3 \equiv \delta_1^3\},$$

where \mathcal{G}_2 is defined in (4), and σ_1^2 is the mass variance,

$$\sigma_1^2 = \int_{\mathbf{k}} P_{11}(k). \quad (14)$$

Note that the first operator in our set, the unity, after shifting, produces the Zel'dovich field which is relevant for the redshift space model.

4.1. Real space

The real space density model is given by

$$\begin{aligned} \delta_g^{\text{EFT}}(\mathbf{k}) &= \beta_1(k) \tilde{\delta}_1(\mathbf{k}) + \beta_2(k) (\tilde{\delta}_1^2)^\perp(\mathbf{k}) \\ &\quad + \beta_{\mathcal{G}_2}(k) \tilde{\mathcal{G}}_2^\perp(\mathbf{k}) + \beta_3(k) (\tilde{\delta}_1^3)^\perp(\mathbf{k}), \end{aligned} \quad (15)$$

where the tidal operator is defined by eq. (4) but using the linear density field, and $\beta_i(k)$ are transfer functions. Their shape is fitted from the simulation snapshots δ_g^{HOD} ,

$$\beta_i(k) = \frac{\langle \mathcal{O}_i^{*\perp}(\mathbf{k}) \delta_g^{\text{HOD}}(\mathbf{k}) \rangle'}{\langle |\mathcal{O}_i^\perp(\mathbf{k})|^2 \rangle'}. \quad (16)$$

In general, the transfer functions have a complicated scale dependence. Their low- k limit, however, can be predicted in perturbation theory. Matching the two provides a practical way to extract the EFT parameters. The simplest way to do it is to replace δ_g^{HOD} with the usual EFT model density field $\delta_g^{\text{EFT}}|_{\text{n-pf}}$ in eq. (16). In contrast to eq. (15) with the transfer functions, $\delta_g^{\text{EFT}}|_{\text{n-pf}}$ is the usual perturbative model that is used in n -point function calculations. At the one-loop order, one has

$$\begin{aligned} \beta_1(k) &= b_1 + (-b_1 c_s + b'_{\nabla^2 \delta}) k^2 + \frac{b_2 \langle \tilde{\delta}_1 \tilde{\delta}_2 \rangle'}{2 \langle \tilde{\delta}_1 \tilde{\delta}_1 \rangle'} - b_1 \frac{\langle \tilde{\delta}_1 \tilde{\mathcal{S}}_3 \rangle'}{\langle \tilde{\delta}_1 \tilde{\delta}_1 \rangle'} \\ &+ \left(b_{\mathcal{G}_2} + \frac{2b_1}{7} \right) \frac{\langle \tilde{\delta}_1 \tilde{\mathcal{G}}_2 \rangle'}{\langle \tilde{\delta}_1 \tilde{\delta}_1 \rangle'} + \left(b_{\Gamma_3} + \frac{b_1}{6} + \frac{5}{2} b_{\mathcal{G}_2} \right) \frac{\langle \tilde{\delta}_1 \tilde{\Gamma}_3 \rangle'}{\langle \tilde{\delta}_1 \tilde{\delta}_1 \rangle'} \end{aligned} \quad (17)$$

where $b_1, b'_{\nabla^2 \delta}, b_2, b_{\mathcal{G}_2}, b_{\Gamma_3}$ are the usual Eulerian bias parameters. c_s is the dark matter speed of sound. In what follows we will use a definition

$$b'_{\nabla^2 \delta} = -b_1 c_s + b'_{\nabla^2 \delta}, \quad (18)$$

since only this combination appears in the galaxy density counterterm. The extra operator that appears in the r.h.s of eq. (17) is characterized by the kernel

$$F_{\mathcal{S}_3} = -\frac{3}{14} \left(1 - \frac{(\mathbf{k}_1 \cdot \mathbf{k}_2)^2}{k_1^2 k_2^2} \right) \frac{((\mathbf{k}_1 + \mathbf{k}_2) \cdot \mathbf{k}_3)}{|\mathbf{k}_1 + \mathbf{k}_2|^2}, \quad (19)$$

which is defined as in eq. (6). As far as other transfer functions are concerned, one can show that in the $k \rightarrow 0$ limit

$$\begin{aligned} \beta_2(k) &= \frac{b_2}{2} + \mathcal{O}(k^2/k_{\text{NL}}^2), \\ \beta_{\mathcal{G}_2}(k) &= b_{\mathcal{G}_2} + \frac{2}{7} b_1 + \mathcal{O}(k^2/k_{\text{NL}}^2), \\ \beta_3(k) &= \frac{b_3}{6} + \mathcal{O}(k^2/k_{\text{NL}}^2), \end{aligned} \quad (20)$$

where k_{NL} is the non-linear scale of perturbation theory, satisfying $k_{\text{NL}}^3 P_{11}(k_{\text{NL}}) \sim 1$. The power spectrum of the error between the simulation and the perturbative model is defined as

$$P_{\text{err}}(k) = \langle |\delta^{\text{EFT}}(\mathbf{k}) - \delta^{\text{HOD}}(\mathbf{k})|^2 \rangle'. \quad (21)$$

In perturbation theory, by definition⁷ P_{err} should be equal to the power spectrum of the stochastic field ϵ . The EFT prediction for it reads

$$P_{\text{err}} = \frac{1}{\bar{n}} \left(1 + \alpha_0 + \alpha_1 \left(\frac{k}{0.45 \text{ hMpc}^{-1}} \right)^2 \right), \quad (22)$$

where \bar{n} is the true number density of galaxies or halos. Note that here we use the convention consistent with the EFT analysis pipeline based on the CLASS-PT code.

4.2. Efficient calculation of the β_1 transfer function

The shapes that appear in eq. (17) require loop calculations in Lagrangian space. In order to calculate them efficiently using the available tools for fast loop integration, it is convenient to work directly within the equivalent framework of IR resummed Eulerian perturbation theory. As a first step, we rewrite the model (15) as

$$\delta_g^{\text{EFT}} = \sum_{\mathcal{O}_a = \tilde{\delta}_1^2, \tilde{\mathcal{G}}_2, \tilde{\delta}_1^3} \beta_a(k) \mathcal{O}_a^\perp = \beta_1(k) \tilde{\delta}_1. \quad (23)$$

This representation is useful as the sum over non-linear operators in the l.h.s. above vanishes after correlating it with $\tilde{\delta}_1$. Adding and subtracting $b_1 \tilde{\delta}_1$ to the l.h.s. of the above equation, multiplying everything by $\tilde{\delta}_1(\mathbf{k}')$ and taking the expectation values we get

$$\langle \delta_g^{\text{EFT}} - b_1 \tilde{\delta}_1 | \tilde{\delta}_1 \rangle' + b_1 P_{\tilde{\delta}_1 \tilde{\delta}_1} = \beta_1(k) P_{\tilde{\delta}_1 \tilde{\delta}_1}, \quad (24)$$

where $P_{\tilde{\delta}_1 \tilde{\delta}_1}(k) = \langle \tilde{\delta}_1(\mathbf{k}) \tilde{\delta}_1(\mathbf{k}) \rangle'$. Recall that primes denote stripping off the Dirac delta functions. The equation above is useful because its leftmost term starts with the second order in perturbation theory, i.e. at the linear level (equivalently $k \rightarrow 0$) we have $\beta_1(k) = b_1$. At the non-linear level, the leftmost term above is the cross-spectrum between $\tilde{\delta}_1$ and a new field $\Delta \delta_g$ defined as

$$\Delta \delta_g \equiv \delta_g^{\text{EFT}} - b_1 \tilde{\delta}_1. \quad (25)$$

Both $P_{\tilde{\delta}_1 \tilde{\delta}_1}$ and $P_{\Delta \delta_g \tilde{\delta}_1} \equiv \langle \Delta \delta_g \tilde{\delta}_1 \rangle'$ can be computed in Eulerian perturbation theory. To this end, we start with the Eulerian kernel expansion for $\tilde{\delta}_1$,

$$\tilde{\delta}_1 = \sum_{m=1}^3 \left(\prod_{n=1}^m \int_{\mathbf{k}_n} \delta_1(\mathbf{k}_n) \right) (2\pi)^3 \delta_D^{(3)}(\mathbf{k} - \mathbf{k}_{1\dots n}) \tilde{K}_n, \quad (26)$$

⁷ Note that P_{err} also absorbs the cutoff-dependent part of the auto-spectrum of δ^2 . This part, however, is negligibly small for our choice of the grid smoothing and we will ignore it in what follows.

where we suppressed the explicit momentum dependence of \tilde{K}_n above, and in real space

$$\begin{aligned}\tilde{K}_1(\mathbf{k}) &= 1, \\ \tilde{K}_2(\mathbf{k}_1, \mathbf{k}_2) &= 1 + \frac{1}{2} \left(\frac{(\mathbf{k}_2 \cdot \mathbf{k}_1)}{k_1^2} + \frac{(\mathbf{k}_1 \cdot \mathbf{k}_2)}{k_2^2} \right), \\ \tilde{K}_3 &= \frac{1}{2} \frac{(\mathbf{k}_2 \cdot \mathbf{k})(\mathbf{k}_3 \cdot \mathbf{k})}{k_2^2 k_3^2}.\end{aligned}\quad (27)$$

\tilde{K}_3 above should be symmetrized w.r.t. individual momenta. Note that the kernels above have poles as one of their momentum arguments becomes very soft. This is because by construction they are produced by the Taylor expansion over the linear displacement. The auto spectrum of $\tilde{\delta}_1$ at one loop order is given by

$$\begin{aligned}P_{\tilde{\delta}_1} &= P_{11} + 2 \int_{\mathbf{p}} \tilde{K}_2^2(\mathbf{k} - \mathbf{p}, \mathbf{p}) P_{11}(|\mathbf{k} - \mathbf{p}|) P_{11}(p) \\ &+ 6 \tilde{K}_1(\mathbf{k}) P_{11}(k) \int_{\mathbf{p}} \tilde{K}_3(\mathbf{p}, -\mathbf{p}, \mathbf{k}) P_{11}(p),\end{aligned}\quad (28)$$

where P_{11} is the linear matter power spectrum.

Using the kernels in eq. (27) we can obtain a series expansion for $\Delta\delta_g$ similar to eq. (26) but with the new kernels

$$\begin{aligned}\tilde{F}_1^b &= F_1^b - b_1 \tilde{K}_1 = 0, \\ \tilde{F}_2^b &= F_2^b - b_1 \tilde{K}_2 = \frac{b_2}{2} + \left(b_{\mathcal{G}_2} + \frac{2}{7} b_1 \right) F_{\mathcal{G}_2}, \\ \tilde{F}_3^b &= F_3^b - b_1 \tilde{K}_3,\end{aligned}\quad (29)$$

where F_n^b are usual Eulerian bias kernels (i.e. the Z_n kernels from [98] with $f \equiv 0$). Note that the Zel'dovich shifts cancel in the new kernels \tilde{F}_n^b by construction.

Now one can calculate the cross-spectrum between $\tilde{\delta}_1$ and $\tilde{\delta}_g^{\text{EFT}}$ in Eulerian perturbation theory:

$$\begin{aligned}P_{\tilde{\delta}_1 \Delta g} &= 3 \tilde{K}_1(\mathbf{k}) P_{11}(k) \int_{\mathbf{p}} \tilde{F}_3^b(\mathbf{p}, -\mathbf{p}, \mathbf{k}) P_{11}(p) \\ &+ 2 \int_{\mathbf{p}} \tilde{K}_2(\mathbf{k} - \mathbf{p}, \mathbf{p}) \tilde{F}_2^b(\mathbf{k} - \mathbf{p}, \mathbf{p}) P_{11}(|\mathbf{k} - \mathbf{p}|) P_{11}(p).\end{aligned}\quad (30)$$

Note that we need to supplement this expression with appropriate counterterms $P_{\tilde{\delta}_1 \Delta g}^{\text{ctr}}$, which will be discussed shortly. Loop integrals in both expressions (28) and (42) can be evaluated with FFTLog.

As a last step, one can use the formalism of time-sliced perturbation theory to perform IR resummation directly at the level of the correlation function $P_{\tilde{\delta}_1 \Delta g}$ and $P_{\tilde{\delta}_1}$. The details of this calculation are summarized in Appendix A.

The result of this calculation is identical to the resummation of usual correlators in Eulerian perturbation theory:

$$\begin{aligned}P_{\tilde{\delta}_1 X} &= P_{\tilde{\delta}_1 X}^{\text{tree}} [e^{-k^2 \Sigma^2} (1 + k^2 \Sigma^2) P_w + P_{nw}] \\ &+ P_{\tilde{\delta}_1 X}^{1\text{-loop}} [e^{-k^2 \Sigma^2} P_w + P_{nw}],\end{aligned}\quad (31)$$

where $X = \{\tilde{\delta}_1, \Delta g\}$ and P_w and P_{nw} correspond to wiggled and de-wiggled parts of the linear power spectrum. The damping function is defined as

$$\Sigma^2 \equiv \frac{1}{6\pi^2} \int_0^{\Lambda_{\text{IR}}} dp P_{11}(p) [1 - j_0(rs p) + 2j_2(rs p)], \quad (32)$$

where r_s is the position space BAO scale, $j_\ell(x)$ are spherical Bessel functions, and Λ_{IR} is the IR separation scale which we choose $\Lambda_{\text{IR}} = 0.2 \text{ hMpc}^{-1}$ following [79].

4.3. Redshift-space model

The redshift space model takes the following form,

$$\begin{aligned}\delta_g^{\text{EFT}}(\mathbf{k}, \hat{\mathbf{z}}) &= \delta_Z(\mathbf{k}, \hat{\mathbf{z}}) - \frac{3}{7} \mu^2 f \tilde{\mathcal{G}}_2 \\ \beta_1(k, \mu) \tilde{\delta}_1(\mathbf{k}, \hat{\mathbf{z}}) &+ \beta_2(k, \mu) (\tilde{\delta}_1^2)^\perp(\mathbf{k}, \hat{\mathbf{z}}) \\ &+ \beta_{\mathcal{G}_2}(k, \mu) \tilde{\mathcal{G}}_2^\perp(\mathbf{k}, \hat{\mathbf{z}}) + \beta_3(k, \mu) (\tilde{\delta}_1^3)^\perp(\mathbf{k}, \hat{\mathbf{z}}),\end{aligned}\quad (33)$$

where μ is the cosine between the wavevector and the unit line-of-sight direction vector \mathbf{z} :

$$\mu = (\mathbf{k} \cdot \hat{\mathbf{z}}) / k. \quad (34)$$

One observes two new terms: the Zel'dovich field δ_Z and the term proportional to the tidal operator \mathcal{G}_2 . These terms are needed to ensure that the low- k limits of the transfer functions do not depend on μ at the lowest order in perturbation theory. On intermediate scales the transfer functions explicitly depend on μ .

Another important point is that the error field in redshift space is also μ -dependent. Its power spectrum is given by

$$P_{\text{err}}(k, \mu) = \langle |\delta^{\text{EFT}}(\mathbf{k}, \hat{\mathbf{z}}) - \delta^{\text{HOD}}(\mathbf{k}, \hat{\mathbf{z}})|^2 \rangle'. \quad (35)$$

In EFT, the theoretical prediction for the error power spectrum at the first order in derivatives is given by [77, 110]

$$P_{\text{err}}(k, \mu) = \frac{1}{\bar{n}} \left(\alpha_0 + \alpha_1 \left(\frac{k}{k_S} \right)^2 + \alpha_2 \mu^2 \left(\frac{k}{k_S} \right)^2 \right), \quad (36)$$

where $k_S \sim k_{\text{NL}}$, and $\alpha_{0,1,2}$ are EFT constants. In what follows we set $k_S = 0.45 \text{ hMpc}^{-1}$ following [12]. A typical set of transfer functions and P_{err} measurements from our fits are shown in fig. 3.

4.4. Redshift space transfer functions

To measure EFT parameters, we need to understand the low- k limit of the transfer functions. For $\beta_1(k, \mu)$, one can use the same strategy as in the real space case. We rewrite the model (33) as

$$\beta_1(k, \mu) \tilde{\delta}_1 = \delta_g^{\text{EFT}} - \delta_Z + \frac{3}{7} f \mu^2 \tilde{\mathcal{G}}_2 - \sum_{\tilde{\mathcal{O}}_a = \tilde{\delta}_1^2, \tilde{\mathcal{G}}_2, \tilde{\delta}_1^3} \beta_a(k, \mu) \tilde{\mathcal{O}}_a^\perp. \quad (37)$$

Then we add and subtract $(b_1 - 1) \tilde{\delta}_1$ from the r.h.s. above, and correlate the resulting expression with $\tilde{\delta}_1$, which yields

$$\beta_1(k, \mu) = b_1 - 1 + \frac{1}{P_{11}(k, \mu)} \langle \delta_g^{\text{EFT}} - \delta_Z - (b_1 - 1) \tilde{\delta}_1 + \frac{3}{7} f \mu^2 \tilde{\mathcal{G}}_2 | \tilde{\delta}_1 \rangle'. \quad (38)$$

We see that on large scales β_1 does not depend on μ and it is given by $b_1 - 1$. This simplicity was achieved by adding the Zel'dovich field to the model (33). The second important observation is that the shape of β_1 in perturbation theory is controlled by the cross spectrum of $\tilde{\delta}_1$ and

$$\Delta \delta_g = \delta_g^{\text{EFT}} - \delta_Z - (b_1 - 1) \tilde{\delta}_1 + \frac{3}{7} f \mu^2 \tilde{\mathcal{G}}_2. \quad (39)$$

This field by construction starts only at the quadratic order in $\tilde{\delta}_1$. Let us discuss now how to calculate loop corrections in eq. (38). We first calculate perturbative kernels for $\tilde{\delta}_1$ in redshift space:

$$\begin{aligned} \tilde{K}_1(\mathbf{k}) &= 1, \\ \tilde{K}_2(\mathbf{k}_1, \mathbf{k}_2) &= \frac{\mathbf{k} \cdot \mathbf{k}_1}{2k_1^2} + \frac{\mathbf{k} \cdot \mathbf{k}_2}{2k_2^2} \\ &\quad + \frac{(f\mu k)}{2} \left(\frac{k_{1z}}{k_1^2} + \frac{k_{2z}}{k_2^2} \right), \\ \tilde{K}_3 &= \frac{1}{2} \left(\frac{(\mathbf{k}_2 \cdot \mathbf{k})(\mathbf{k}_3 \cdot \mathbf{k})}{k_2^2 k_3^2} + f \frac{(\mathbf{k}_2 \cdot \mathbf{k}) k_z k_{3z}}{k_2^2 k_3^2} \right. \\ &\quad \left. + f \frac{(\mathbf{k}_3 \cdot \mathbf{k}) k_z k_{2z}}{k_2^2 k_3^2} + f^2 \frac{k_z^2 k_{2z} k_{3z}}{k_2^2 k_3^2} \right), \end{aligned} \quad (40)$$

where $k_{iz} = (\mathbf{k}_i \cdot \hat{\mathbf{z}})$, and $\mathbf{k} \equiv \mathbf{k}_1 + \dots + \mathbf{k}_n$ for the n 'th kernel. This allows us to compute the power spectrum $\tilde{\delta}_1$ using the same expression (28) but with the above kernels. The perturbative kernels for the ‘‘subtracted’’ galaxy density (39) are given by

$$\begin{aligned} \tilde{Z}_1 &= Z_1 - F_1^Z - (b_1 - 1) \tilde{K}_1 = 0, \\ \tilde{Z}_2 &= Z_2 - F_2^Z - (b_1 - 1) \tilde{K}_2 + \frac{3}{7} f \mu^2 F_{\mathcal{G}_2}, \\ \tilde{Z}_3 &= Z_3 - F_3^Z - (b_1 - 1) \tilde{K}_3 \\ &\quad + \frac{3}{7} f \mu^2 F_{\mathcal{G}_2}(\mathbf{k}_1, \mathbf{k}_2) \left(\frac{(\mathbf{k} \cdot \mathbf{k}_3)}{k_3^2} + f \mu k \frac{k_{3z}}{k_3^2} \right), \end{aligned} \quad (41)$$

where Z_n are the usual redshift-space non-linear kernels in Eulerian standard perturbation theory [98, 111], and F_n^Z are the Zel'dovich redshift space kernels in standard perturbation theory [111–114]. The cross-spectrum $P_{1\Delta g}$ is given by

$$\begin{aligned} P_{1\Delta g} &= 3 \tilde{K}_1(\mathbf{k}) P_{11}(k) \int_{\mathbf{p}} \tilde{Z}_3(\mathbf{p}, -\mathbf{p}, \mathbf{k}) P_{11}(p) \\ &\quad + 2 \int_{\mathbf{p}} \tilde{K}_2(\mathbf{k} - \mathbf{p}, \mathbf{p}) \tilde{Z}_2(\mathbf{k} - \mathbf{p}, \mathbf{p}) P_{11}(|\mathbf{k} - \mathbf{p}|) P_{11}(p). \end{aligned} \quad (42)$$

Note again that we also need to add appropriate counterterms to renormalize the above loop integrals. The loop integrals in eq. (42) are easy to compute with FFTLog using the expansion over powers of μ^2 developed in [77].

Finally, one can IR-resumm the infrared displacements using the redshift space version of TSPT. The details are provided in Appendix A. The final expression is given by

$$\begin{aligned} P_{1X} &= P_{1X}^{\text{tree}} [e^{-\mathcal{S}(k, \mu)} (1 + \mathcal{S}(k, \mu)) P_w + P_{nw}] \\ &\quad + P_{1X}^{1\text{-loop}} [e^{-\mathcal{S}(k, \mu)} P_w + P_{nw}], \end{aligned} \quad (43)$$

where the redshift-space variant of the damping function is given by:

$$\begin{aligned} \mathcal{S}(k, \mu) &= k^2 (\Sigma^2 (1 + f \mu^2 (2 + f)) + \delta \Sigma^2 f^2 \mu^2 (\mu^2 - 1)), \\ \delta \Sigma^2 &= \int_0^{\Lambda_{1R}} \frac{dp}{2\pi^2} P_{11}(p) j_2(pr_s). \end{aligned} \quad (44)$$

In practice, we have found that the redshift-space corrections to the IR resummation formula for redshift-space one-loop spectra are negligible for the purpose of fitting the transfer functions. Given that, our main results are obtained with approximate templates in which the loops are evaluated with the isotropic (real space) exponential damping. If a better precision is required, it is

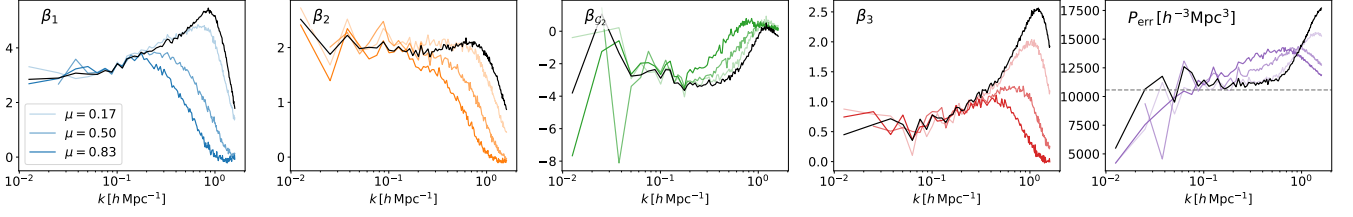


FIG. 3. Typical forward model transfer functions and noise power spectra for HOD galaxies in real space (black lines) and in redshift space, for three μ bins. Note that we subtract 1 and 0.5 from the real space transfer functions for β_1 and $\beta_{\mathcal{G}_2}$ to match the low- k limit of the redshift space transfer functions. Dashed line in the rightmost panel depicts the \bar{n}^{-1} Poisson prediction.

straightforward to implement the templates with the full redshift-space corrections as in eq. (43).

As for the other transfer functions, one can obtain that in the low- k limit they are μ -independent, and proportional to the real space ones, c.f. eq. (20),

$$\begin{aligned}\beta_2(k, \mu) &= \frac{b_2}{2}, \\ \beta_{\mathcal{G}_2}(k, \mu) &= b_{\mathcal{G}_2} + \frac{2}{7}b_1 - \frac{1}{2}, \\ \beta_3(k, \mu) &= \frac{b_3}{6}.\end{aligned}\quad (45)$$

The corrections to these expressions are both scale and μ -dependent.

4.5. Counterterms

In EFT, the leading order higher-derivative contributions to the galaxy density field in redshift space is given by [110, 115]

$$\delta_g^{\text{EFT}} \Big|_{k^2} = (-b_1 c_s + b'_{\nabla^2 \delta} + f c_{s2} \mu^2 + f^2 c_{s4} \mu^4) k^2 \delta_1, \quad (46)$$

where c_{s2}, c_{s4} are redshift space counterterms (Wilson coefficients). c_{s4} above comes from the renormalization of the velocity field. The equivalence principle dictates that this counterterm be the same for galaxies and dark matter [110]. c_s is the real space dark matter counterterm. $b_{\nabla^2 \delta}$ and c_{s2} are higher-derivative bias and μ^2 galaxy counterterms. These are expected to depend on the galaxy population. Plugging this into $\Delta \delta_g$ and correlating with δ_1 produces the following contribution to the transfer function β_1 :

$$\beta_1(k, \mu) \Big|_{k^2} = (-b_1 c_s + b'_{\nabla^2 \delta} + f c_{s2} \mu^2 + f^2 c_{s4} \mu^4) k^2. \quad (47)$$

Let us discuss now how these counterterms are related to the actual physical observables. The leading order coun-

terterms in eq. (46) produce the following power spectrum contribution

$$P_g^{\text{ctr}} = 2(b_1 + f\mu^2)(b_{\nabla^2 \delta} + f c_{s2} \mu^2 + f^2 c_{s4} \mu^4) P_{11}(k). \quad (48)$$

This can be re-arranged as:

$$P_g^{\text{ctr}} = 2(\tilde{c}_0 + \tilde{c}_2 f \mu^2 + \tilde{c}_4 f^2 \mu^4 + \tilde{c}_6 f^3 \mu^6) k^2 P_{11}, \quad (49)$$

with

$$\begin{aligned}\tilde{c}_0 &= b_{\nabla^2 \delta} b_1, & \tilde{c}_2 &= (b_1 c_{s2} + b_{\nabla^2 \delta}), \\ \tilde{c}_4 &= (b_1 c_{s4} + c_{s2}), & \tilde{c}_6 &= c_{s4}.\end{aligned}\quad (50)$$

The CLASS-PT code uses the following convention for the counterterms appearing in front of the redshift space multipoles,

$$P_\ell^{\text{ctr}} = -2c_\ell \frac{2\ell + 1}{2} \int_{-1}^1 d\mu \mathcal{L}_\ell(\mu) f^{\ell/2} \mu^\ell (k^2 P_{11}) . \quad (51)$$

Comparing this with eq. (49) we get the following map between the field level coefficients and the counterterms used to fit the actual data:

$$\begin{aligned}c_0 &= -\left(\tilde{c}_0 + \frac{f}{3}\tilde{c}_2 + \frac{f^2}{5}\tilde{c}_4 + \frac{f^3}{7}\tilde{c}_6\right), \\ c_2 &= -\left(\tilde{c}_2 + \frac{6f}{7}\tilde{c}_4 + \frac{5f^2}{7}\tilde{c}_6\right), \\ c_4 &= -\left(\tilde{c}_4 + \frac{15f}{11}\tilde{c}_6\right), \\ c_6 &= -\tilde{c}_6,\end{aligned}\quad (52)$$

where \tilde{c}_ℓ are given in eq. (50).

Note that in redshift space the naive one-loop EFT model breaks down at relatively small $k_{\text{max}} \lesssim 0.1 \text{ hMpc}^{-1}$ because the non-linear scale in redshift space is lower than that in real space. The reach of the one-loop model can be increased at the expense of introducing one additional fitting parameter b_4 (also denoted as \tilde{c}) [98, 99, 116, 117]. It is a coefficient in front of the

following higher order power spectrum counterterm contribution

$$P_{\nabla_{\mathbf{z}}^4 \delta} = -b_4 k^4 \mu^4 f^4 (b_1 + f\mu^2)^2 P_{11} \quad (53)$$

that can be used as a proxy for two-loop effects. The presence of this term in the power spectrum model translates into an additional field level counterterm

$$\delta_g^{\text{EFT}} \Big|_{k^4} = -\frac{b_4}{2} k^4 \mu^4 f^4 (b_1 + f\mu^2) \delta_1, \quad (54)$$

which gives the following correction to the transfer function:

$$\beta_1(k, \mu) \Big|_{k^4} = -\frac{b_4}{2} k^4 \mu^4 f^4 (b_1 + f\mu^2). \quad (55)$$

4.6. Corrections for cutoff dependence

The EFT parameters are scheme and cutoff dependent. The CLASS-PT code that we employ here uses dimensional regularization (dim. reg.) implemented via the FFTLog method. All converging loop integrals are computed exactly, while the diverging ones are set to zero. For the one-loop power spectrum integrals that we encounter in our calculation, the only divergent part is given by the mass variance integral

$$\sigma_\Lambda^2 = \int_{|\mathbf{k}| \leq \Lambda} P_{11}(k). \quad (56)$$

One can show that the corresponding corrections to the transfer functions are removed at the field level after applying the orthogonalization [63, 68]. Thus, we can ignore corrections proportional to eq. (56) on both the power spectrum side and the field level side. In practice, however, we measure EFT transfer functions at a finite cutoff provided by the grid resolution. Let us argue now, that even if this cutoff is formally present, it does not require any additional adjustments of the fitting procedure.

Let us discuss now the cutoff dependence of the transfer functions that affects the matching of the converging loop integrals. On the field level side, our transfer function measurements are subject to grid resolution effects that arise due to the clouds in cells (CIC) interpolation. Although we apply the standard algorithm for the compensation of the CIC window, there is a residual bias that effectively acts as a soft low pass filter whose characteristic scale is proportional to the Nyquist frequency $k_{\text{Ny}} = \pi N_{\text{mesh}}/L_{\text{box}}$ [118]. Thus, our EFT parameter

measurements are taken, technically, at a finite cutoff $\Lambda \sim k_{\text{Ny}}$. To obtain their values at $\Lambda \rightarrow \infty$, consistent with dim. reg., we need to add the missing UV pieces, i.e. to “run” the EFT constants up to infinity.

The first relevant transfer function is β_1 . Let us start our discussion with the dark matter at the field level. In this case, the only relevant EFT parameter is the sound speed c_s , which renormalizes the $k^2 P_{11}$ contribution to the total power spectrum. The physical coefficient in front of this term is independent of the cutoff, i.e.

$$\begin{aligned} & -2c_s(\Lambda) - \frac{61}{630\pi^2} \int_0^\Lambda dp P_{11}(p) \\ & = -2c_s(\Lambda = \infty) - \frac{61}{630\pi^2} \int_0^\infty dp P_{11}(p). \end{aligned} \quad (57)$$

where for the sake of the argument we approximated the low-pass filter as a sharp cutoff. $c_s(\Lambda = \infty) = c_s$ is the value from the fit of the power spectrum without any cutoff that reproduces the usual measurement from the power spectrum with CLASS-PT. Eq. (57) shows that if one were to fit data with the one-loop integrals evaluated all the way to infinity, this would give $c_s(\Lambda = \infty)$ without the need to additionally “run” it from Λ . This is true even if the actual fields have a cutoff, which is always the case in simulations.

The sound speed also enters the k^2 correction to the $\beta_1(k)$ transfer function at the field level. In order to fit it, we have to compute the shape of β_1 in perturbation theory. At the one loop order this calculation is identical to the usual power spectrum calculation [69]. It will give us the exact same expression for the cutoff-dependence of c_s as in eq. (57). Hence, if one chooses $\Lambda = \infty$ in the theory model for the transfer function, this will produce the sound speed in the desired $\Lambda \rightarrow \infty$ limit. This argument is also true for bias tracers and in redshift space.

All in all, we conclude that if one fits the β_1 transfer function with perturbation theory shapes computed without an explicit cutoff in dim. reg., the results will be the same as if our fields did not have an explicit cutoff. This implies that we can ignore the cutoff altogether in our PT calculations, and the EFT parameters extracted from β_1 should match those of the n -point functions.

As for the β_2 and β_{G_2} transfer functions, they must approach the dim. reg. values of $b_2/2$ and b_{G_2} on large scales thanks to the auto-spectrum of δ^2 , which will suppress the loop corrections on large scales [63]. Hence, one can ignore the cutoff dependence of these terms pro-

vided that the field-level cutoff is reasonably small, such that the auto-spectrum of δ^2 is saturated. This is the case for our baseline choice of the Nyquist frequency $k_{\text{Ny}} = 1.6 \text{ hMpc}^{-1}$ which we use both for *Quijote* and *Abacus*.

4.7. Fitting procedure

Let us discuss our fitting procedure to extract the EFT parameters from the transfer functions and the error spectra. Let us start with the real space transfer functions $\beta_2, \beta_{\mathcal{G}_2}, \beta_3$. Based on eqs. (20) and (45) we use the following template to fit them:

$$\beta_X = a_0^X + a_1^X k^2 + a_2^X k^4, \quad X = \{\delta^2, \mathcal{G}_2, \delta^3\}. \quad (58)$$

Then we take a_0^X as a measurement of the corresponding bias parameter. Since by construction our redshift space transfer functions do not bring additional information on the nonlinear bias parameters, we extract them from the real space measurements only. It will be interesting to predict these transfer functions in perturbation theory. We have found that the fit in eq. (58) is stable up to $k_{\text{max}} = 0.4 \text{ hMpc}^{-1}$. This is our baseline choice in redshift space.

As far as b_1, b_{Γ_3} and $b_{\nabla^2 \delta}$ are concerned, we fit them from the shape dependence of $\beta_1(k)$ in real space, given by

$$\beta_1(k) = b_1 + \frac{P_{1\Delta g}(k)}{P_{11}(k)} + b_{\nabla^2 \delta} k^2. \quad (59)$$

$P_{1\Delta g}$ above depends on $\{b_1, b_{\mathcal{G}_2}, b_2, b_{\Gamma_3}\}$. In principle, one could fit these parameters from $\beta_1(k), \beta_2(k), \beta_{\mathcal{G}_2}(k)$ simultaneously, but in practice b_2 and $b_{\mathcal{G}_2}$ measurements are always dominated by the corresponding transfer functions. For our main analysis, we fix b_2 and $b_{\mathcal{G}_2}$ to the transfer function best-fit values when fitting β_1 , which gives us $\{b_1, b_{\Gamma_3}, b_{\nabla^2 \delta}\}$.

The real space stochasticity EFT parameters are extracted by fitting P_{err} with the EFT prediction eq. (22). The redshift space P_{err} measurements give us the $\mu^2 k^2$ counterterm (36), which we fit from the μ^2 -dependence of the noise having fixed α_0 and α_1 to their real space values, as required by the consistency of the EFT. Note that the non-linear corrections are larger in redshift space due to virialized motions of galaxies and dark matter particles, known as fingers-of-God [119]. For that reason, we

use $k_{\text{max}} = 0.2 \text{ hMpc}^{-1}$ in our fits to the redshift space transfer functions and $P_{\text{err}}(k, \mu)$. This choice is based on the observation that the scaling of the stochastic noise in redshift space starts deviating from the $k^2 \mu^2$ behaviour for $k > 0.2 \text{ hMpc}^{-1}$. We have also found that this choice minimized the scale-dependence of α_2 , which otherwise becomes significant for $k_{\text{max}} > 0.2 \text{ hMpc}^{-1}$. Details of this analysis can be found in Appendix B. Note that our baseline value $k_{\text{max}} = 0.2 \text{ hMpc}^{-1}$ for redshift-space is consistent with the scale cut extracted from high fidelity simulations and the actual data [12, 89].

Finally, we fit the redshift space transfer function $\beta_1(k)$ in PT:

$$\beta_1(k, \mu) = b_1 - 1 + \frac{P_{1\Delta g}(k)}{P_{11}(k)} + \beta_1 \Big|_{k^2} + \beta_1 \Big|_{k^4}, \quad (60)$$

where $\beta_1 \Big|_{k^2, k^4}$ are the higher derivative counterterms defined in eq. (47) and eq. (55). Then we convert the measured values of the redshift space counterterms to the counterterms used in CLASS-PT with eq. (52).

Before we move on, let us note that for our final HOD-based priors we fit the universal counterterm c_{s4} from dark matter transfer functions in redshift space. In this case, we use $k_{\text{max}} = 0.15 \text{ hMpc}^{-1}$ consistent with the EFT fits to redshift space dark matter from [99, 117]. We have checked that raising it up to $k_{\text{max}} = 0.2 \text{ hMpc}^{-1}$ does not have a significant impact on our results.

5. SIMULATION-BASED PRIORS

5.1. Cosmology dependence of EFT parameters for dark matter halos and galaxies

We start our investigation of the cosmology dependence of the EFT parameters with dark matter halos. This is a natural first step given that the cosmology-dependence of EFT parameters for HOD galaxies is ‘‘inherited’’ from that of the underlying dark matter halos, up to corrections due to assembly bias. Indeed, for the linear galaxy bias $b_{1,g}$ we have [109, 120]

$$b_{1,g} = \bar{n}_g^{-1} \int d \ln M \frac{d\bar{n}_h}{d \ln M} \langle N_c \rangle_M [1 + \langle \mathcal{N}_s \rangle_M] b_1(M), \quad (61)$$

where $b_1(M)$ is the linear bias of halos, $\langle N_c \rangle_M, \langle \mathcal{N}_s \rangle_M = \langle N_c N_s \rangle_M$ are expectation values for numbers of central and satellite galaxies in halos of mass M , and \bar{n}_g is the

galaxy number density. We will use $\langle N_g \rangle$ to denote the total HOD,

$$\langle N_g \rangle_M = \langle N_c \rangle_M [1 + \langle \mathcal{N}_s \rangle_M]. \quad (62)$$

The number density of halos of mass M , $d\bar{n}_h/d\ln M$, or the halo mass function (HMF), can be modeled analytically,

$$\frac{d\bar{n}_h}{d\ln M} = \frac{\bar{\rho}_m}{M} \left| \frac{d\ln \sigma_M}{d\ln M} \right| f\left(\frac{\delta_c}{\sigma_M}\right), \quad (63)$$

where the function $f(\nu)$ captures the fraction of the mass of the Universe locked up in halos. Its simplest form is given by the Press-Schechter theory [121],

$$f_{\text{PS}}(\nu) = \sqrt{\frac{2}{\pi}} \nu e^{-\nu^2/2}, \quad (64)$$

where we introduced the ‘‘peak height’’ parameter

$$\nu \equiv \frac{\delta_c}{\sigma_M(z)}, \quad (65)$$

where $\delta_c = 1.686$ is the threshold overdensity,⁸ and σ_M^2 is the mass variance in spherical cells whose radius is equal to the Lagrangian radius of the protohalo,

$$\sigma_M^2(z) = \int_{\mathbf{k}} P_{11}(k, z) W_R^2(kR[M]), \quad (66)$$

where $W_R(x)$ is the Fourier image of the position space spherically symmetric top-hat window function, and $R[M] = (3M/(4\pi\bar{\rho}_m))^{1/3}$ is the comoving Lagrangian radius, with $\bar{\rho}_m$ standing for the background matter density at redshift zero,

$$\bar{\rho}_m \equiv \rho_c \Omega_m, \quad \rho_c = 2.77 \cdot 10^{11} h^2 M_\odot \text{Mpc}^{-3}. \quad (67)$$

Note that we measure distances and masses in units of $h^{-1}\text{Mpc}$ and $h^{-1}M_\odot$, in which case the critical density above is constant for all **Quijote** LH catalogs.

While other parametrization exist for $f(\nu)$ in the literature [123, 124], the key property relevant for our discussion is that $f(\nu)$ depends only on the peak height, i.e. it is universal to the changes of cosmology, redshift, and the halo mass. HMFs with this property are called universal. Our arguments given below will apply to any universal

HMF. Note that the universality of the HMF is a basic assumption of the analytic halo models [87, 88].

Within the halo model, expressions analogous to eq. (61) can be derived for other deterministic EFT parameters as well. Namely, the EFT parameters defined via,

$$\delta_h = \sum_{a=1} b_{\mathcal{O}_a}^h \mathcal{O}_a(\mathbf{x}), \quad \delta_g = \sum_{a=1} b_{\mathcal{O}_a}^g \mathcal{O}_a(\mathbf{x}), \quad (68)$$

where $\mathcal{O}_a = \{\delta, \frac{1}{2}\delta^2, \mathcal{G}_2, \dots\}$, satisfy

$$b_{\mathcal{O}_a}^g = \bar{n}_g^{-1} \int d\ln M \frac{d\bar{n}_h}{d\ln M} \langle N_g \rangle_M b_{\mathcal{O}_a}^h(M). \quad (69)$$

The universality of the HMF suggests that the EFT parameters of halos should depend on mass and cosmology via the peak height parameter in eq. (65),

$$b_{\mathcal{O}_a}^h(M) = b_{\mathcal{O}_a}^h(\nu[M]). \quad (70)$$

Analytic results for $b_1(\nu)$ and $b_2(\nu)$ following from the HMF are available in the literature [109, 125]. Under the assumption of the HMF universality the stochastic EFT parameters are also expected to primarily depend on cosmology via the peak height, as follows from halo exclusion models [126]. Eq. (70) suggests that the cosmology-dependence of the EFT parameters of halos should be degenerate with the halo mass. Let us investigate to what extent this is supported by direct measurements.

We perform EFT-based field-level fits of snapshots from **Quijote** LH catalogs that cover 2000 different cosmological models. Due to the limited mass resolution of **Quijote**, we focus on the halo mass range $\log_{10}(M/[M_\odot/h]) = 13 - 13.5$ for all catalogs at our baseline redshift $z = 0.5$. We produce two sets of EFT parameters for friends-of-friends (FoF) and Rockstar halo-finders. In principle, one should treat the halo finder as a parameter of our UV model during the production of priors. We will comment on it in detail shortly. Our results are shown in figs. 4, 5.

First, we see that the bias parameters and real space counterterms for FoF and Rockstar are quite consistent. There are differences only at the level of the stochasticity parameters α_0 and α_1 . In addition, the RSD counterterms are also somewhat different, which is expected given differences in the velocity assignments between the two halo finders.

As far as cosmology dependence is concerned, we see a noticeable correlation only with (Ω_m, σ_8) parameters.

⁸ In principle, δ_c depends on cosmology, but this dependence is quite weak, $\lesssim 1\%$, see e.g. [122], so this effect is negligible for prior generation.

Another important observation is that EFT parameter samples with a fixed halo mass and varied cosmology-dependence that we study here are quite similar to EFT parameter samples for a fixed cosmology and varied halo masses, in line with the above expectations based on the halo model. To illustrate this better, we measured EFT parameters from FoF halo catalogs based on the **Quijote** fiducial simulation. The (overlapping) halo mass bins we consider are

$$\begin{aligned} \log_{10}(M/[h^{-1}M_{\odot}]) \in & [12, 12.5], [12.5, 13], \\ & [13.2, 13.8], [13.4, 14], [13, 13.5], [13.5, 14], \\ & [13.6, 14.2], [13.8, 14.4], [14, 14.5]. \end{aligned} \quad (71)$$

These results for the bias parameters $b_1, b_2, b_{G_2}, b_{\Gamma_3}$ and $b_{\nabla^2\delta}$ and the corresponding peak heights ν are shown in fig. 6. The picture is similar for other EFT parameters, see Appendix E. In addition, we plot the EFT parameters for the same halo mass bins from the baseline **Abacus** simulation.⁹ This allows us to bracket the uncertainty in the EFT parameters due to the use of the CompaSO halo finder [107] (discussed shortly), which we find to be comparable to that of the FoF-Rockstar difference.

Fig. 6 demonstrates that the variation of the halo mass at a fixed cosmology acts like a variation of cosmology for a given halo mass. This confirms the expectation that the cosmology dependence of the samples, to a large extent, is degenerate with the halo mass, as predicted within the halo model. Comparing the **Quijote** and **Abacus** halo results we note that the exact dependence of bias parameters on the peak height is halo-finder dependent. Nevertheless the functions such as $b_2(b_1)$ appear to be the virtually the same for the galaxy bias parameters. We do find some differences at the level of $b_{\nabla^2\delta}$ and other counterterms (see Appendix E for more detail), but these differences are much smaller than the width of the HOD distributions for these parameters.

In figs. 4, 5, we display the correlation between bias parameters and $\sigma_M(z=0.5)$ for $M=10^{13}M_{\odot}/h$. First, we see that ν is naturally highly correlated with Ω_m and σ_8 . Second, it is strongly correlated with the EFT parameters. In fact, it appears to be more correlated with the halo parameters than σ_8 and Ω_m themselves. Note

⁹ We have added two additional bins, $\log_{10}(M/[h^{-1}M_{\odot}]) \in [11, 11.5], [11.5, 12]$, which we could not extract from **Quijote** because of the limited resolution.

that the halo number density is additionally correlated with Ω_m through the normalization in eq. (63).

All in all, our measurements confirm the analytical argument that the cosmology-dependence of the EFT parameters should be approximately captured by the peak height ν and hence is degenerate with the halo mass. Hence, to the first approximation, one can simply fix cosmology and vary the halo mass in order to generate the samples for EFT parameters.

Having established that EFT parameters of halos are approximately cosmology-independent, let us now discuss the implications for the cosmology-dependence of the HOD galaxies. Eq. (69) can be rewritten as

$$b_{\mathcal{O}_a}^g = \bar{n}_g^{-1} \int d\nu \frac{d\bar{n}_h(\nu)}{d\nu} \langle N_g \rangle_{M[\nu]} b_{\mathcal{O}_a}^h(\nu). \quad (72)$$

From this expression it is clear that the EFT parameters of galaxies can acquire cosmology-dependence only through the mapping $\nu[M]$. We argue now that for the standard HOD functions such as [27], the bulk of this cosmology-dependence can be absorbed by re-defining the HOD parameters themselves.

In the basic HOD models for galaxies, we integrate over the halo mass distribution a with the HOD weights

$$\begin{aligned} \langle N_c \rangle_M &= \frac{1}{2} \left[1 + \text{Erf} \left(\frac{\log_{10} M - \log_{10} M_{\text{cut}}}{\sqrt{2}\sigma} \right) \right], \\ \langle \mathcal{N}_s \rangle_M &= \Theta_H(M - \kappa M_{\text{cut}}) \left(\frac{M - \kappa M_{\text{cut}}}{M_1} \right)^\alpha, \end{aligned} \quad (73)$$

where $\Theta_H(x)$ is the Heaviside step function, and $M_{\text{cut}}, \sigma, M_1, \kappa$ and α are free parameters. The above HOD saturates the relevant bias parameter integrals at M_{cut} , which effectively acts as a cutoff that determines the lower range of halos hosting the relevant galaxies. As we vary this parameter, we effectively vary the mass of the host halo. The latter, as we showed, is equivalent to varying cosmology. Hence, the variation of the halo mass captures the bulk of cosmology dependence.

To make this argument more precise, we explicitly show in Appendix C that the cosmology dependence of EFT parameters of HOD galaxies can be almost entirely absorbed by re-defining the HOD parameters. We prove this analytically for a power-law cosmology with the linear matter power spectrum $P_{11} \propto k^n$, noting that our conclusions in fact apply to more realistic dependencies. Interestingly, we find that the satellite HOD in eq. (73) introduces a mild cosmology dependence on the slope of the linear matter power spectrum n when $M \sim \kappa M_{\text{cut}}$.

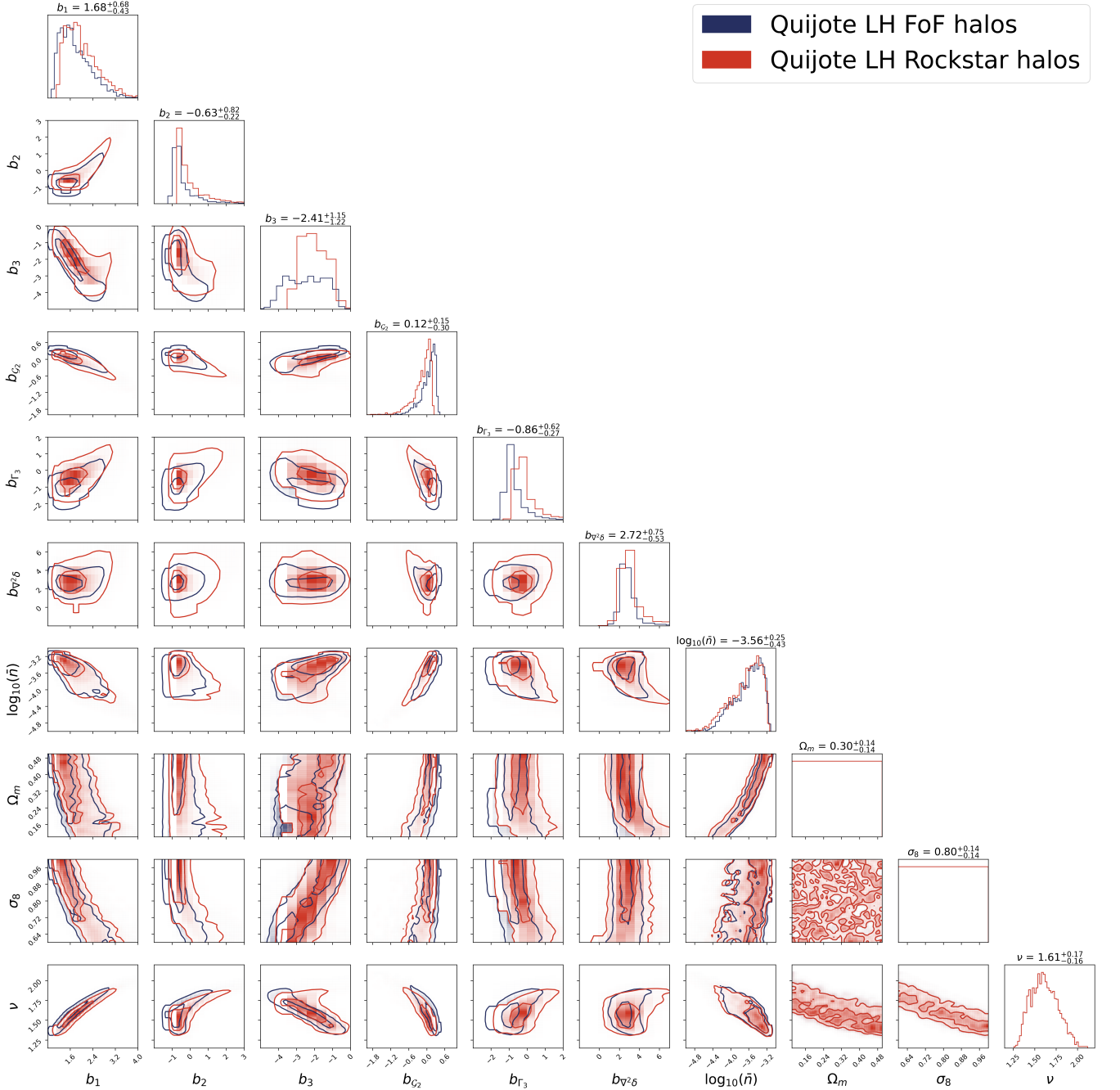


FIG. 4. The joint distribution of EFT parameters and number densities of dark matter halos with masses in range $\log_{10}(M/[M_{\odot}/h]) = 13 - 13.5$ from 2000 *Quijote* LH simulations at $z = 0.5$. We show results of both FoF and Rockstar halo finders. For cosmological parameters, we only show the correlation with σ_8 and Ω_m , and the halo peak height ν . The correlation with other cosmological parameters varied in *Quijote* LH mocks, (n_s, h, Ω_b) is negligible. Density levels correspond to two-dimensional $1\text{-}\sigma$ and $2\text{-}\sigma$ intervals (i.e. 39.3% and 86.5% of samples).

However, the dependence on the mass fluctuation amplitude at the redshift of the sample $\sigma_8(z)$ can be absorbed by the HOD parameters exactly even for a realistic ΛCDM cosmology. For instance, a $\approx 15\%$ shift in

σ_8 , similar to the difference between the σ_8 of *Abacus* and our best-fit from BOSS is equivalent to a shift of $\Delta \log_{10} M_{\text{cut}} \approx 0.3$. In what follows, we use sufficiently wide ranges of HOD priors to account for such shifts.

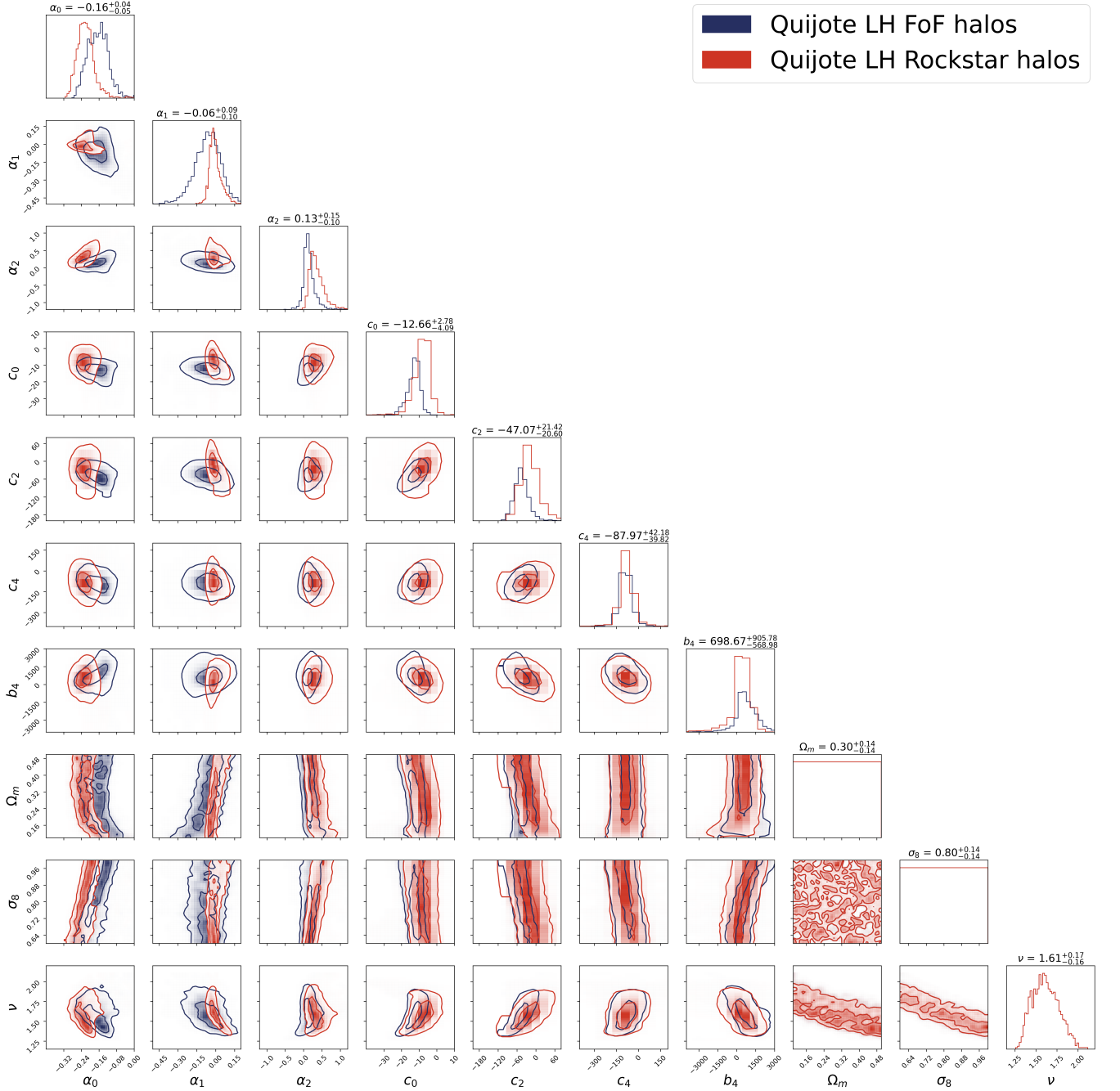


FIG. 5. Same as fig. 4 but for the stochastic EFT parameters and redshift-space counterterms. The number density is omitted.

In addition, variations of other HOD parameters beyond the basic ones, e.g. assembly bias, will generate an extra scatter around the halo relations between the EFT parameters. As can be seen from comparing figs. 4, 5 for halos and Fig. 2 of [36], this scatter is stronger than the variation of cosmology itself, at least for the real space parameters. We will see shortly that this is also the case for the redshift space counterterms.

Given these arguments, we will ignore the explicit cosmology dependence in what follows. We will generate EFT distributions by varying HOD parameters at a fixed cosmology. We choose this cosmology to be the *Abacus* fiducial cosmology consistent with the *Planck* 2018 best-fit Λ CDM model.

Before closing this section, let us note that the statement about cosmology-independence of EFT parameters

is approximate. It relies on several crucial approximations. First, we have assumed the universality of HMF. This approximation is accurate to $\lesssim 5\%$ [127]. Second, based the halo model arguments, we have assumed that the EFT parameters of halos depend only on the peak height, which is consistent with our *Quijote* measurements, but is still a simplification. Third, our proof of the degeneracy between cosmology and the HOD parameters was carried out for the power-law cosmology. Although our proof of the cosmology-independence is formally exact for the mass fluctuation amplitude $\sigma_8(z)$, it remains approximate for the parameters controlling the effective slope of the linear matter power spectrum. Fourth, our proof relied on the standard HOD parametrization and did not include velocity bias, assembly bias, or other parameters of the “decorated” HOD extensions. In general, one may expect that departures from these approximations generate a residual cosmology dependence of the EFT parameters. However, our explicit tests of the residual cosmology-dependence in Appendix D suggest that it is negligible for the purpose of generating the ensemble of EFT parameters. Thus, our semi-analytic arguments provide a basic explanation for the approximate cosmology-independence suggested by simulations.

We note however that the residual dependence of EFT parameters may be important if one wants to systematically connect small and large scales via a conditional distribution between the EFT and cosmological parameters [36, 39]. This task is beyond the scope of our paper, which primarily focuses on producing priors distributions for EFT parameters.

5.2. HOD-based priors

Having shown that the cosmology dependence of EFT parameters should have a negligible effect in the context of HOD models, we now generate HOD mock galaxy catalogs based on the *AbacusSummit* simulation (referred to as *Abacus* for compactness in what follows) and extract their parameters at the field level. We use the HOD models and code described in [128].

We generate 10500 HOD galaxy snapshots at $z = 0.5$ using the fiducial cosmology of *Abacus*. Each catalog is characterized by a set of HOD parameters which we

randomly sample from the following flat distribution:

$$\begin{aligned} \log_{10} M_{\text{cut}} &\in [12, 14], & \log_{10} M_1 &\in [13, 15], \\ \log \sigma &\in [-3.5, 1.0], & \alpha &\in [0.5, 1.5], \\ \alpha_c &\in [0, 1], & \alpha_s &\in [0, 2], & s &\in [0, 1], & \kappa &\in [0.0, 1.5], \\ A_{\text{cen}} &\in [-1, 1], & A_{\text{sat}} &\in [-1, 1], \\ B_{\text{cen}} &\in [-1, 1], & B_{\text{sat}} &\in [-1, 1]. \end{aligned} \tag{74}$$

We use the spherical overdensity CompaSO halo finder to identify dark matter halos from our snapshots. We have found that the CompaSO halo finder produces results very similar to the other halo finders, see Appendix E. In general, the variance between different halo finders is much smaller than the width of the HOD priors for galaxies. This implies that the choice of the halo finder does not produce a significant uncertainty during prior generation.

The EFT parameters extracted from these samples are shown in figs. 7, 8, along with the *Quijote* halo samples from figs. 4, 5. The first relevant observation is that the HOD densities are much wider than the halo ones. This confirms our expectation that the variation of HOD parameters is much more important for distribution of EFT parameters than the variation of cosmology. Note that the tails of the halo distributions for certain parameters, see e.g. the upper part of the $b_3 - b_1$ plane, “leak” outside the regions covered by the HOD densities. These “leaks” can be explained by the fact that the HOD bias parameters are given by the integrals over the halo biased weighted with the HOD and HMF, see eq. (69). This weighting effectively shifts the bias parameters of galaxies away from the halo values [129].

Also note that unlike our previous work [36], here we do not condition our samples on the number density to match BOSS. We do so in order for our priors to be applicable to both BOSS and DESI. This also allows us to produce a wider, more conservative, distribution of EFT parameters. The histogram with the number densities of our samples can be seen in the lower panel of fig. 7. The total range covered is $[8.3 \cdot 10^{-3}, 1.1 \cdot 10^{-5}] [h\text{Mpc}^{-1}]^3$. The median of the distribution is $1.1 \cdot 10^{-3} [h\text{Mpc}^{-1}]^3$, while the 16th and 84th percentiles are $5.4 \cdot 10^{-3} [h\text{Mpc}^{-1}]^3$ and $1.3 \cdot 10^{-4} [h\text{Mpc}^{-1}]^3$, enclosing both the typical number densities of BOSS LRGs, $\bar{n}_g \approx 3.5 \cdot 10^{-4} [h\text{Mpc}^{-1}]^3$ [130] and DESI LRGs, $\bar{n}_g \approx 5 \cdot 10^{-4} [h\text{Mpc}^{-1}]^3$ [131].

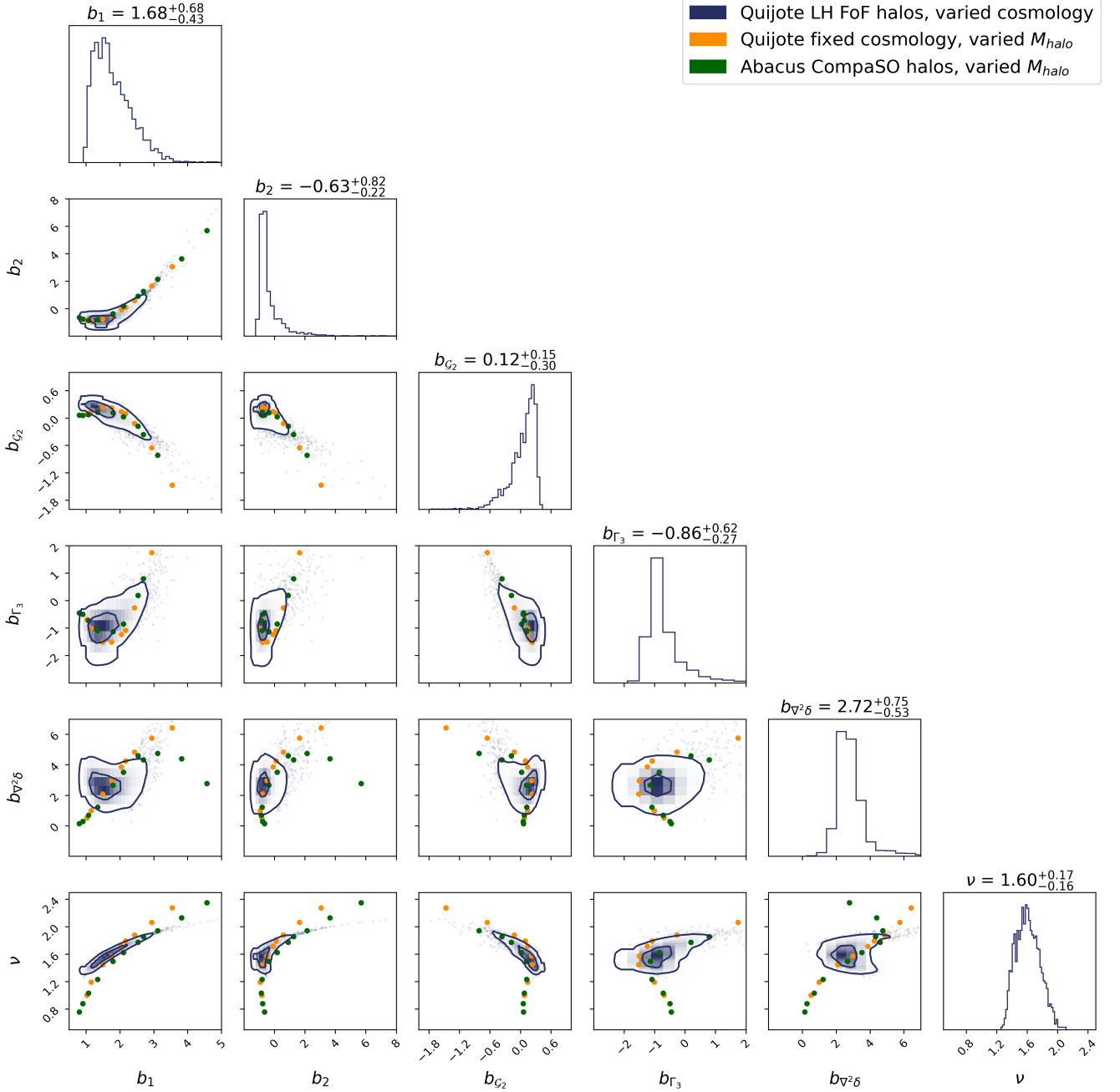


FIG. 6. The distribution of EFT parameters from the FoF halo catalogs of the **Quijote** fiducial cosmology simulation at $z = 0.5$ versus the **Quijote** halo samples from Fig. 4 with fixed halo mass, but varied cosmology. In addition, we also show results for **Abacus** halos at fixed cosmology.

As an additional test, we produced several HOD catalogs where we vary both HOD and cosmological parameters. To that end we select two cosmologies with larger and smaller values of σ_8 from the large **Abacus** boxes. The analysis of large boxes is significantly more expensive than the baseline **Abacus** mocks, so we use the large

boxes with varied cosmology only to test our baseline distribution. The details of this test are given in Appendix D. This analysis confirms that variations of cosmology are negligible compared to the variations of HOD parameters.

Before closing this section, let us discuss some inter-

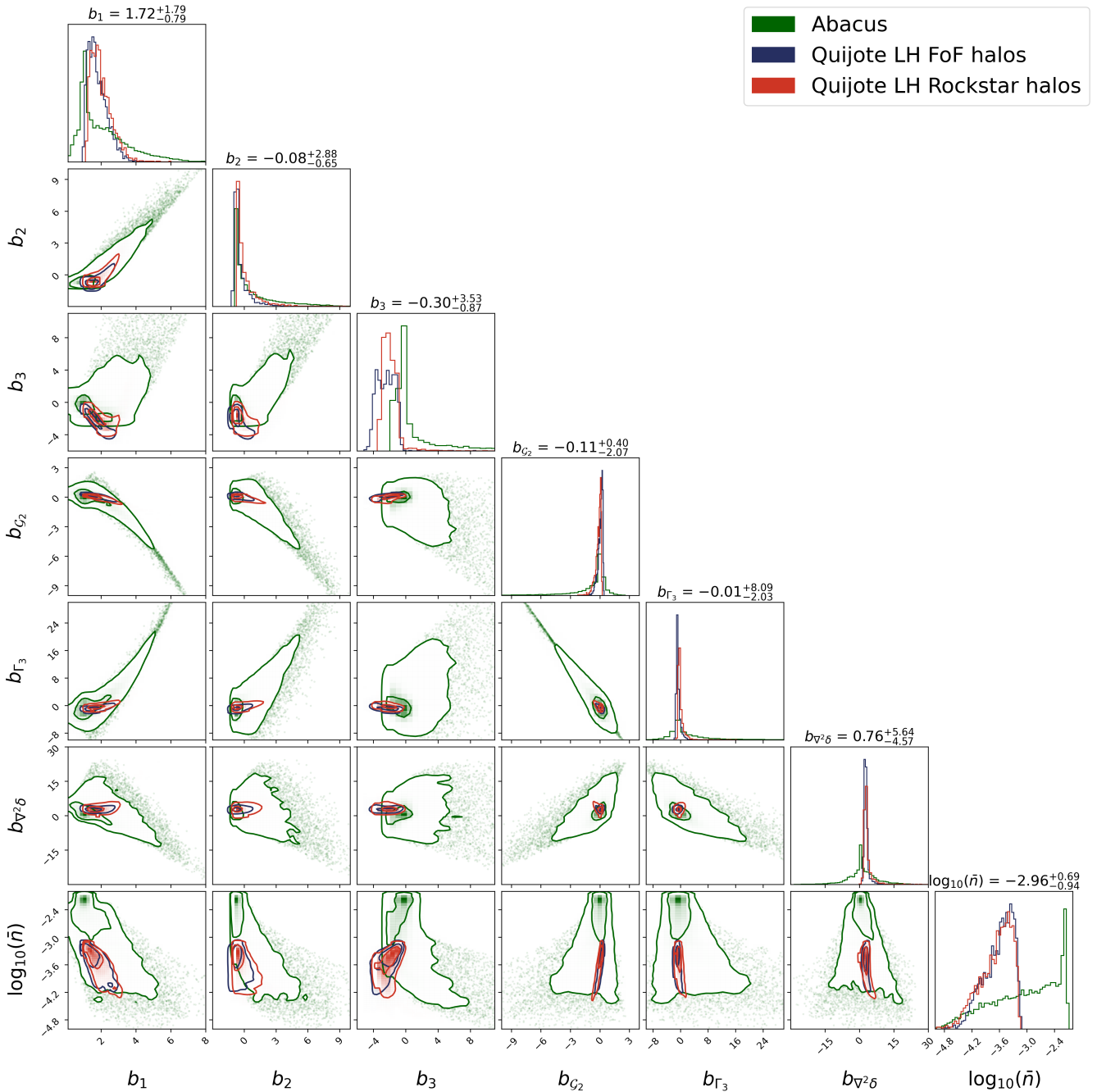


FIG. 7. The distribution of EFT galaxy bias parameters and number densities of 10500 HOD galaxy models based on the Abacus fiducial cosmology simulation $z = 0.5$ versus the halo samples from Fig. 4.

esting correlations between the EFT parameters. While the dependencies of non-linear bias parameters on the linear bias, e.g. $b_2(b_1)$, trace the halo ones very well, for stochasticity parameters we see some interesting correlations that appear specific to galaxies.

For halos, the stochastic counterterm α_0 is quite close to zero, see fig. 5, with $\sim 10\%$ deviations consistent

with the halo exclusion estimates [126, 132]. For galaxies, however, α_0 can be as large as $\mathcal{O}(10)$. This is because galaxies trace dark matter halos, and hence their P_{err} is close to that of the halos on large scales [126], which can be much larger than \bar{n}_g^{-1} . Indeed, in agreement with [126], we found that large α_0 are specific to HODs with large M_{cut} and low M_1 , which correspond to

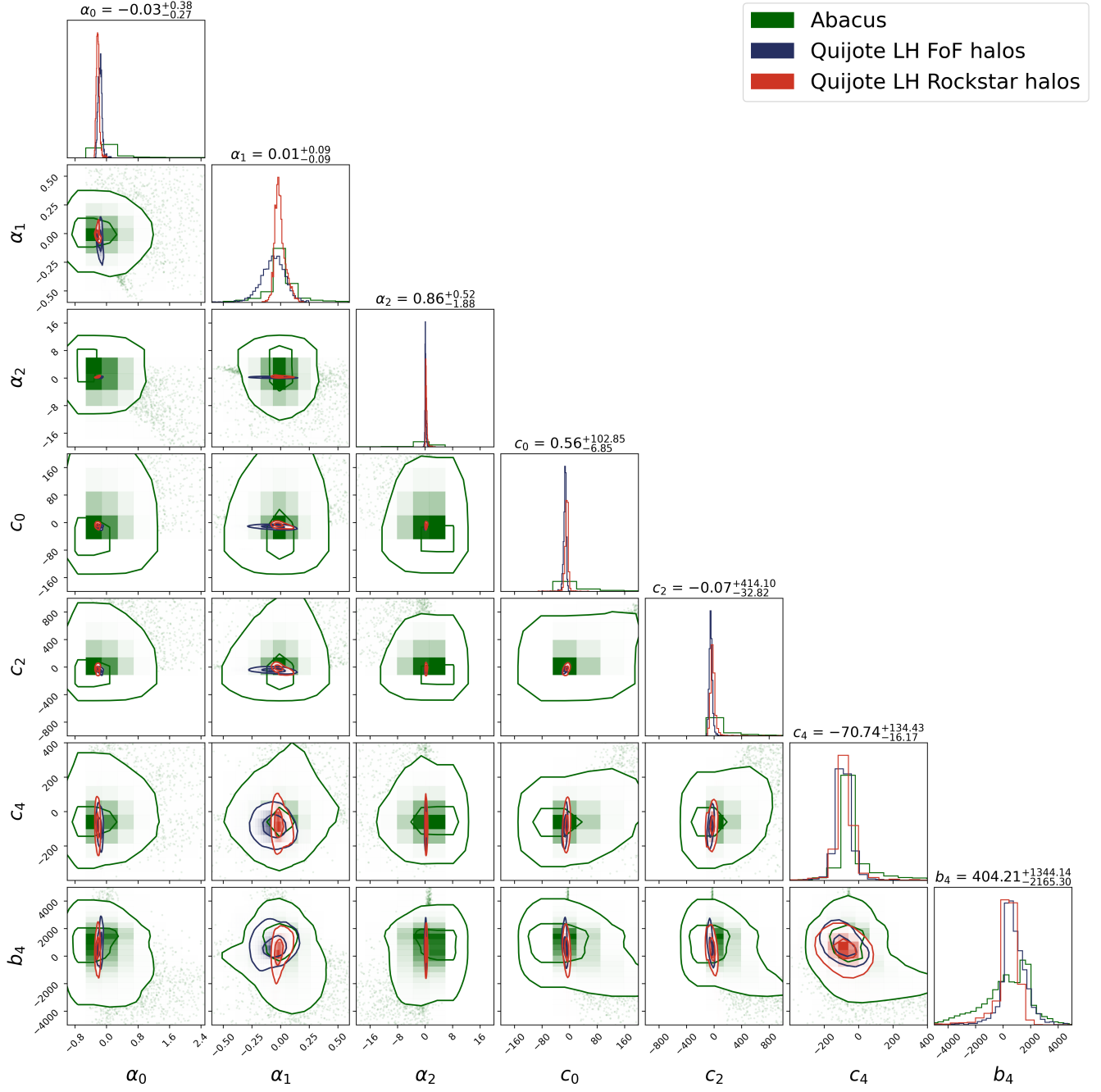


FIG. 8. The distribution of EFT stochasticity and counterterm parameters of 10500 HOD galaxy models based on the Abacus fiducial cosmology simulation $z = 0.5$ versus the halo samples from Fig. 4.

samples with a large number of satellites living in massive halos. In this case it is natural to have the hierarchy $P_{\text{err}} \sim \bar{n}_h^{-1} \gg \bar{n}_g^{-1}$, resulting in large α_0 .

As far as the stochastic counterterm α_1 is concerned, its behavior is also consistent with [126], and it can be linked with the exclusion effects. In particular, α_1 is typically positive for samples with a low satellite frac-

tion. In this case the scale-dependence associated with α_1 describes the increase of $P_{\text{err}} \simeq \bar{n}_h^{-1}$ on large scales up to \bar{n}_g^{-1} on small scales. α_1 can also be negative for samples with a large satellite fraction. This is because on large scales $P_{\text{err}} \sim \bar{n}_h^{-1}$ (the twiddle accounts for corrections due to exclusion), while on small scales $P_{\text{err}} \sim \bar{n}_g^{-1} \ll \bar{n}_h^{-1}$, implying the reduction of stochastic-

ity as one increases k .

Quite interestingly, we have found that in redshift space, the restoration of the \bar{n}_g^{-1} behavior of the noise power spectrum on small scales happens faster for the modes along the line of sight. The velocity field “assists” to recover the high- k behavior quicker by means of the redshift-space stochastic counterterm α_2 . Specifically, samples with small/large satellite fraction tend to have positive/negative α_2 , needed to reach the expected \bar{n}_g^{-1} small scale behavior. In particular, one can see that the negative tail of α_2 in fig. 8 is strongly correlated with the super-Poisson stochasticity, $\alpha_0 \gg 1$. It will be interesting to develop a better physical understanding of the peculiar behavior of α_2 in the context of the halo model along the lines of [14, 126]. We additionally study a representative extreme outlier from this regime in Appendix E.

5.3. Including information from dark matter

The equivalence principle dictates that the redshift space counterterm c_{s4} be the same for galaxies and dark matter. This information helps us reduce the number of free parameters in our fits to HOD transfer functions. We have measured the counterterm from the dark matter snapshot of **Abacus**, and used this measurement as a prior in fits to galaxies. This allowed us to significantly improve the precision of the c_4 field-level measurement and reduce the scatter in the $c_2 - b_4$ plane. We show this change in the counterterm measurements in fig. 9, where for convenience we also display b_1 . As expected, we see that the DM prior on c_{s4} has mostly affected the c_4 and b_4 counterterms that are sensitive to the $\mu \approx 1$ modes.

Since we are using the c_{s4} prior on dark matter from the **Abacus** cosmology, one may be concerned about the propagation of the cosmology dependence in this prior. To address this, we measure the standard deviation of the c_{s4} parameters from **Quijote** LH mocks, and apply it as a standard deviation to the **Abacus** dark matter c_{s4} prior in our fit of EFT parameters from the **Abacus** HODs. We find virtually no difference in the EFT parameter measurements in this case (the means and the standard deviations are affected by less than 1%), see the gray contours in fig. 9. This implies that the cosmology-dependence of c_{s4} can be neglected in practical applications.

The new counterterms and the real space parameters

presented in figs. 7, 8 constitute our final EFT parameter distribution, which we will use as SBP in our full-shape analysis.

5.4. Density estimation

To model the marginal density distribution of the EFT parameters, we use the same method as in our ref. [36]. Briefly, we use Masked Autoregressive normalizing flows [133] to approximate the density of the EFT parameters. 10% of our EFT samples are used in validation, while the rest is used for training. The flow is trained with 30 000 steps and batch size 128, using the Adam optimizer with learning rate $3 \cdot 10^{-4}$. We use **nflows**¹⁰ library, and **PyTorch** [134] for training and evaluation. All other aspects of our normalizing flow implementation and training routine are the same as in our ref. [36]. To extract optimal HOD parameters from our EFT chains from BOSS data we have also built a conditional distribution $p(\theta_{\text{HOD}}|\theta_{\text{EFT}})$, following [36]. In principle, one can use the normalizing flows to produce a conditional model for the distribution of the EFT parameters given the HOD ones, $p(\theta_{\text{EFT}}|\theta_{\text{HOD}})$, which can provide insights into physics behind the EFT parameters. We leave this for future work.

Note that we do not use b_3 in our priors as this parameter does not appear in the one-loop power spectrum and three-level bispectrum calculations which we use in our fitting models.

Note that the samples that we generated depend on the number density \bar{n} which is a measurable parameter. One possible approach is to condition the distribution to the number density. Fig. 7, however, shows that the EFT parameters for our HOD samples are consistent with a broad range of number density values, which suggests that the use of the conditional model will not significantly shrink the EFT prior density. We have validated this explicitly by producing a conditional model, and generating samples with a fixed number density $\bar{n} \approx 2 \cdot 10^{-4} [h\text{Mpc}^{-1}]^3$ similar to that of the BOSS CMASS sample. We obtained a distribution of the EFT parameters which matches the original one (where we effectively marginalize over \bar{n}) very closely. Thus, the approach of conditioning on the number density does not

¹⁰ <https://github.com/bayesiains/nflows>

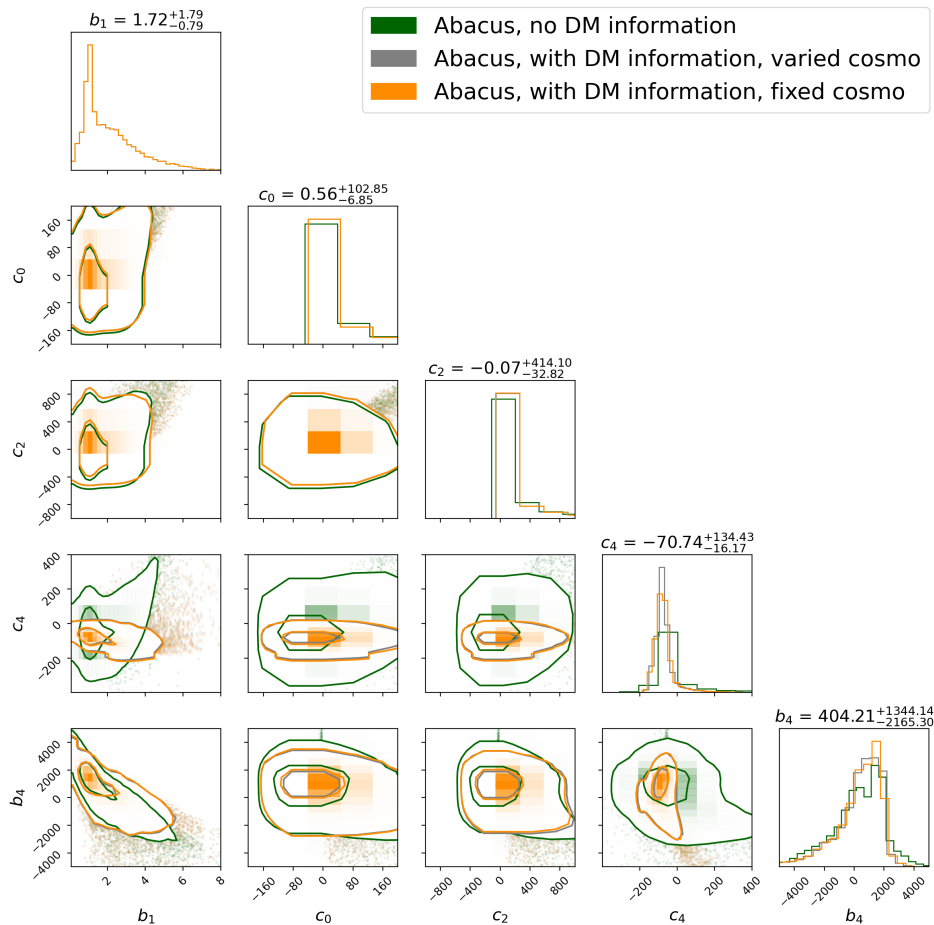


FIG. 9. The distribution of b_1 and EFT counterterms for redshift space multipoles without and with the dark matter information in the form of the c_{s4} redshift space counterterm measurement.

lead to a significant narrowing of the EFT distribution in the context of the BOSS survey, but it may be more useful for other surveys such as DESI.

5.5. Effects of Realistic Surveys

There are two effects relevant for the actual survey that we would like to discuss: the effective redshift and fiber collision corrections.

Since the actual galaxies are observed on a past light-cone, their observed power spectrum is weighted with the selection function $\bar{n}(z)$:

$$P_\ell^{\text{obs}}(k) = \frac{\int d^3r \bar{n}^2(r) P_\ell(k, z(r))}{\int d^3r \bar{n}^2(r)}. \quad (75)$$

The above integral is approximated as $P_\ell(k, z_{\text{eff}})$, where

z_{eff} is defined as

$$z_{\text{eff}} = \frac{\int d^3r \bar{n}^2(r) z(r)}{\int d^3r \bar{n}^2(r)}. \quad (76)$$

The rationale behind this approximation is that the Taylor expansion of the power spectrum around the effective redshift then starts only at a second order,

$$P_\ell^{\text{obs}}(k) = P_\ell(k, z_{\text{eff}}) + \frac{\int d^3r \bar{n}^2(r) (z - z_{\text{eff}})^2 P_\ell''(k, z_{\text{eff}})}{2 \int d^3r \bar{n}^2(r)}, \quad (77)$$

where we ignored higher order terms. It is customary to ignore the rightmost term above in cosmological analyses. In this approximation, all nuisance parameters can be treated as constants taken at the effective redshift.

A comment on the redshift dependence of our priors is in order. We have calibrated our sample of EFT parameters at $z = 0.5$, which is very close, but not exactly the same as the effective redshifts of the BOSS data that

we will use, $z_{\text{eff}} = 0.38, 0.61$ [54]. We argue now that the effects of redshift evolution are largely irrelevant for the HOD-based priors. First, as we have established, the EFT parameters for dark matter halos depend on cosmology primarily through a single parameter, σ_M . Hence, a change of σ_M due to redshift can be fully compensated by a change of the halo mass M . Hence, as long as our prior on the HOD parameter M_{cut} related to M is wide enough, its variation can effectively absorb the redshift mismatch. Second, our full HOD model with extra effects such as the assembly bias, assumes that the distribution of galaxies is determined only by properties of dark matter at a given redshift, i.e. there is no explicit dependence on the past evolution. Together with the (approximate) universality of the halo mass function, this suggests that the HOD galaxies at different redshifts should be self-similar, which implies the redshift-independence of the EFT priors.

The second important effect is the collision of optical fibers. At the power spectrum, it can be modeled with the effective window approach of [135]. It was pointed out in ref. [98, 136, 137] that on small scales the effect of this effective window can be fully absorbed by the stochastic counterterms, which makes the implementation of the full effective window model unnecessary.¹¹ Indeed, for $k > 0.02 \text{ hMpc}^{-1}$ the fiber collision effective window leads to the following typical shifts of the constant shot noise contribution:

$$\begin{aligned} z=0.61 : \quad \Delta\alpha_0^{\text{fc}} &= -0.04, \\ z=0.38 : \quad \Delta\alpha_0^{\text{fc}} &= -0.03, \end{aligned} \quad (78)$$

while the $k^2\mu^2$ counterterm shifts by $\Delta\alpha_2^{\text{fc}} = 0.06$. The shift in α_1 is too small to be robustly detected. The above numbers have been obtained for the best-fit BOSS power spectra from [12], and they are consistent with results of [135]. To implement the fiber collision shifts at the level of the priors consistently, one has to compute the galaxy power spectrum for each point in the sample, apply the effective window, and extract the shifted stochastic counterterms α_i 's. While it is straightforward to implement this, the overall effect of fiber collisions is

negligibly small to affect our results. A typical shift of $\Delta\alpha_i$ is a tiny fraction of the statistical error σ_{α_i} on these parameters from the data even when using the SBP, e.g. $\Delta\alpha_0 \simeq 0.16\sigma_{\alpha_0}$ for BOSS NGCz1. Given the smallness of the fiber collision corrections, we will ignore them in what follows.

5.6. Validation on PT Challenge simulations

We validate our simulation-based priors on the PT Challenge (PTC) simulation data [89]. First, the PTC suite provides high fidelity mock power spectrum measurements with $\sim 0.1\%$ statistical errorbars, which are ideal for precision tests of the theory model and the priors. Second, their underlying cosmology is different from *Abacus*, and hence it can be used to test our assumption that the cosmology dependence of the EFT parameters is negligible for the purpose of generating the SBP.

We fit the galaxy power spectrum monopole and quadrupole of the PTC mocks at $z = 0.61$. We choose this dataset primarily because it was used in ref. [89]. Our power spectrum likelihood is Gaussian, with the linear theory covariance computed using the total simulation volume $566 [h^{-1}\text{Mpc}]^3$ as in [89]. The hexadecapole can be easily added, but its role is negligible within ΛCDM . While the real-space proxy, and bispectrum multipoles of the same mock can be added to the datavector as well, we prefer not to do it here in order to clearly access the improvements of the $P_0 + P_2$ analysis thanks for SBP. Indeed, the bispectrum and Q_0 mostly help by breaking degeneracies between the cosmological and EFT parameters which are present at the power spectrum level. In our setup, the same degeneracies are expected to be broken by SBP. The comparison between our analysis and the traditional analysis of the $P_\ell + Q_0 + B_\ell$ data plus uninformative priors will show us how much information there is in the large-scale power spectrum once we do not have to pay the price of nuisance parameter marginalization. In addition, the comparison between the EFT parameter posteriors in both cases will serve us as a consistency test.

We compare our results with those obtained with conservative priors [12, 77],

$$\begin{aligned} b_1 &\in \text{flat}[0, 4], \quad b_2 \sim \mathcal{N}(0, 1^2), \\ b_{\mathcal{G}_2} &\sim \mathcal{N}(0, 1^2), \quad b_{\Gamma_3} \sim \mathcal{N}\left(\frac{23}{42}(b_1 - 1), 1^2\right), \end{aligned} \quad (79)$$

¹¹ The uncorrelated fiber collision contribution produces a “non-local” k^{-1} correction sizeable for $k < 0.02 \text{ hMpc}^{-1}$. This contribution can be easily included in an analysis pipeline at no extra cost because it does not depend on the galaxy power spectrum.

$$\begin{aligned} \frac{c_0}{[\text{Mpc}/h]^2} &\sim \mathcal{N}(0, 30^2), & \frac{c_2}{[\text{Mpc}/h]^2} &\sim \mathcal{N}(30, 30^2), \\ \frac{c_4}{[\text{Mpc}/h]^2} &\sim \mathcal{N}(0, 30^2), & \frac{b_4}{[\text{Mpc}/h]^4} &\sim \mathcal{N}(500, 500^2), \end{aligned} \quad (80)$$

$$\begin{aligned} \alpha_0 &\sim \mathcal{N}(0, 1^2), & \alpha_1 &\sim \mathcal{N}(0, 1^2), \\ \alpha_2 &\sim \mathcal{N}(0, 1^2). \end{aligned} \quad (81)$$

We fit the full set of nuisance parameters plus three cosmological parameters of the base Λ CDM model: the physical density of dark matter ω_{cdm} , the Hubble constant H_0 and the mass fluctuation amplitude σ_8 . The rest of the cosmological parameters are set to their true values. Since the PT challenge is ongoing, we will report here only the deviations of the cosmological parameters from their true values. In addition, we will blind the values of b_1 , b_2 and $b_{\mathcal{G}_2}$. We will show their deviations w.r.t. the values estimated from the PTC bispectrum multipoles [58] (consistent with the tree-level and one-loop monopole analyses [138, 139]). Note that unlike the cosmological parameters, these are not the true values, but rather their estimates, which are subject to their own biases and uncertainties. We will not blind the values of other parameters as we believe their knowledge will not provide a significant advantage to potential challenge participants. We use our datavector up to $k_{\text{max}} = 0.14 \text{ hMpc}^{-1}$ validated in [89]. This is lower than the baseline k_{max} for our transfer function fits and the BOSS data because of the outstandingly small statistical error of PTC data, for which the two loop corrections become important at lower momenta than in the actual data.

Our results for the full-shape analysis of PTC data with the conservative and simulation-based priors are displayed in fig. 10 and in table I. First, we have recovered the true input cosmological parameters without bias in the SBP analysis. The bias parameters b_1, b_2 are also recovered without bias, but $b_{\mathcal{G}_2}$ is found in a $\approx 4\sigma$ bias w.r.t. the bispectrum measurement. Given that the maximum of the $b_{\mathcal{G}_2}$ posterior in the conservative analysis is also shifted w.r.t. the bispectrum value, it is suggestive that this tension is a result of a statistical fluctuation. It could also be due to systematic effects, such as a bias in the bispectrum estimate or the use of the Gaussian covariance matrix in our power spectrum likelihood. Alternatively, this tension could arise due to the residual cosmology dependence of the EFT parameters which we

ignored while generating our priors. The shift of $b_{\mathcal{G}_2}$, however, does not exceed the statistical precision with which we measure this parameter from BOSS, and therefore we do not expect it to affect our final constraints at a statistically significant level.

The second important observation is that the posteriors for EFT parameters are consistent in both analysis. Moreover, as anticipated, they shrink dramatically with the SBP. As for the cosmological parameters, constraints on ω_{cdm} , H_0 and σ_8 improve by 60%, 14% and 13%, respectively. The improvements for ω_{cdm} are quite significant because SBP help break its degeneracies with α_0, α_1 and b_{Γ_3} . The improvements on ω_{cdm} and σ_8 are more significant than those coming from the addition of external datasets such as the bispectrum and the real space power spectrum proxy Q_0 [116]. This clearly illustrates the power of the SBP.

Finally, let us note that we have clearly detected both redshift-space counterterms b_4 and α_2 . They are degenerate at the power spectrum level, but the degeneracy is lifted with the SBP. While b_4 is detected even with conservative priors, a statistically significant detection of α_2 with PT Challenge data is possible only with the SBP.

All in all, we conclude that our HOD-based priors successfully pass the validation on the PT Challenge data.

6. APPLICATIONS TO BOSS

In this section we redo the EFT-based full-shape analysis of the BOSS galaxy clustering data using the SBP. Our dataset and likelihood have been extensively used in previous full-shape analysis by [12, 58], which we refer to for the technical details. We analyze BOSS DR12 galaxy clustering data, which are split across two patches of the sky, north galactic cap (NGC) and south galactic cap (SGC), and two non-overlapping redshift bins. In this work, we use the z1-z3 split used in most of the previous BOSS analysis starting with [140]. The two redshift bins z1 and z3 in this case have effective redshifts 0.38 and 0.61, respectively. This choice is done mainly to ease the comparison with previous works such as [12, 58], which used a similar split. We use the publicly available power spectrum and bispectrum measurements obtained with the window-free estimators [141, 142]. Our scale cuts are the same as in [12, 58]. In particular, we use $k_{\text{max}} = 0.2 \text{ hMpc}^{-1}$ for the power spectrum multipoles,

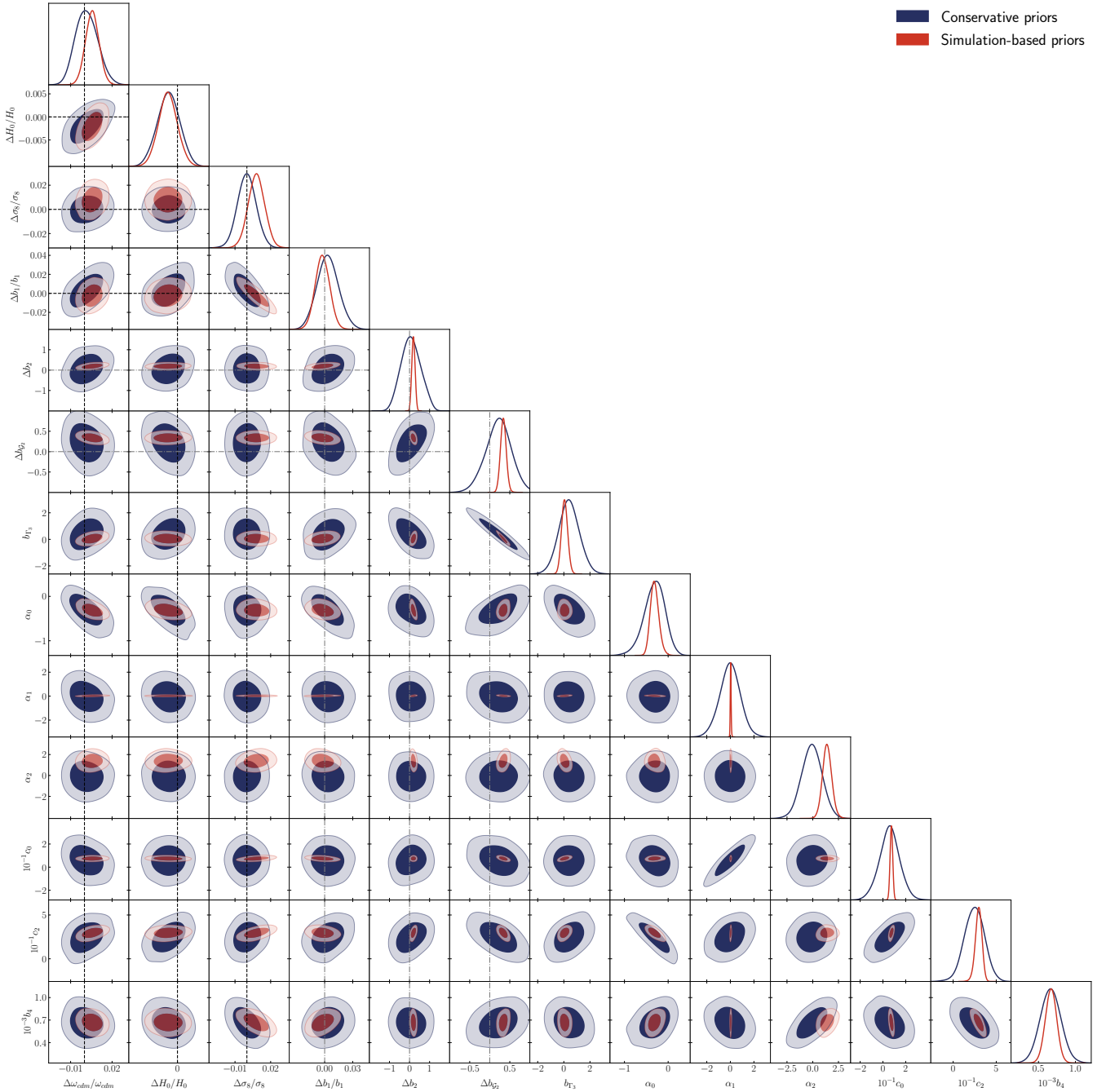


FIG. 10. Cosmological and EFT parameters extracted from the PT Challenge simulation with the usual conservative priors and the SBP derived in this work. For the cosmological parameters we show deviations from the true values, which are depicted by solid dashed lines. We show residuals of bias parameters b_1, b_2, b_{G_2} w.r.t. the PTC bispectrum measurements from [58]; the corresponding values are marked by grey dotted-dashed lines.

which is consistent with the scale cut used to fit the EFT parameters from redshift space transfer functions.

We fix the cosmological parameters to the *Planck* best-fit values [106] except ω_{cdm}, H_0 and $\ln(10^{10}A_s)$ (A_s is the amplitude of primordial scalar perturbations), which we

vary in our Markov Chain Monte Carlo (MCMC) chains. For each BOSS data chunk we use a separate set of EFT parameters. We compare our results with the analysis based on conservative priors carried out in [12] on the same data.

PTC $P_0 + P_2$ data with conservative priors					PTC $P_0 + P_2$ data with simulation-based priors				
Param	best-fit	mean $\pm\sigma$	95% lower	95% upper	Param	best-fit	mean $\pm\sigma$	95% lower	95% upper
$\frac{\Delta\omega_{cdm}}{\omega_{cdm}}$	0.00065	0.0016 $^{+0.0075}_{-0.0085}$	-0.0129	0.0178	$\frac{\Delta\omega_{cdm}}{\omega_{cdm}}$	0.0043	0.0056 \pm 0.0050	-0.0041	0.015
$\Delta H_0/H_0$	-0.0021	-0.0020 $^{+0.0024}_{-0.0024}$	-0.0068	0.0028	$\Delta H_0/H_0$	-0.024	-0.0021 \pm 0.0021	-0.0057	0.0024
$\Delta\sigma_8/\sigma_8$	-0.0015	0.0000 $^{+0.0078}_{-0.0078}$	-0.0152	0.0178	$\Delta\sigma_8/\sigma_8$	0.0077	0.0080 \pm 0.0069	-0.006	0.022
$\Delta b_1/b_1$	0.0041	0.003 $^{+0.012}_{-0.012}$	-0.0187	0.0267	$\Delta b_1/b_1$	-0.0014	-0.0024 \pm 0.0078	-0.018	0.013
Δb_2	0.045	0.07 $^{+0.48}_{-0.48}$	-0.83	1.02	Δb_2	0.19	0.193 \pm 0.081	0.03	0.35
$\Delta b_{\mathcal{G}_2}$	-0.24	0.22 $^{+0.32}_{-0.32}$	-0.42	0.84	$\Delta b_{\mathcal{G}_2}$	0.31	0.340 \pm 0.072	0.2	0.48
b_{Γ_3}	0.3243	0.3964 $^{+0.74}_{-0.79}$	-1.136	1.975	b_{Γ_3}	0.1264	0.0586 $^{+0.24}_{-0.25}$	-0.4202	0.5359
α_0	-0.2642	-0.3097 $^{+0.26}_{-0.2}$	-0.8006	0.1372	α_0	-0.3419	-0.3088 $^{+0.088}_{-0.11}$	-0.5005	-0.1093
α_1	-0.20	-0.02 $^{+0.87}_{-0.83}$	-1.8	1.687	α_1	0.02429	0.02933 $^{+0.035}_{-0.04}$	-0.04861	0.1071
α_2	0.3759	-0.09155 $^{+1}_{-1}$	-2.066	1.891	α_2	1.427	1.401 $^{+0.44}_{-0.48}$	0.4841	2.336
$10^{-1}c_0$	0.5635	0.5742 $^{+0.86}_{-0.86}$	-1.212	2.36	$10^{-1}c_0$	0.7494	0.7454 $^{+0.12}_{-0.12}$	0.5118	0.9788
$10^{-1}c_2$	2.385	2.443 $^{+1.2}_{-1.2}$	0.2061	4.778	$10^{-1}c_2$	3.102	2.946 $^{+0.42}_{-0.36}$	2.164	3.73
$10^{-3}b_4$	0.7123	0.6634 $^{+0.14}_{-0.14}$	0.3846	0.941	$10^{-3}b_4$	0.656	0.6693 $^{+0.08}_{-0.078}$	0.5118	0.8247

TABLE I. Best-fits and 1d marginalized limits for cosmological and EFT parameters from PT Challenge simulation data.

6.1. Results for BOSS NGCz1 sample

To start off, we re-analyze the BOSS NGCz1 data from [12] with $z_{\text{eff}} = 0.38$. We use the galaxy power spectrum monopole P_0 and quadrupole P_2 data from the likelihood described in [12]. The corner plot and 1d marginalized posteriors for the SBP and the conservative prior analyses are shown in fig. 11. The best-fit values and 1d marginalized limits are given in table II. The first important observation is that the SBP results are consistent with the conservative ones: both posteriors largely overlap. The second observation is that the SBP affect the posteriors of EFT parameters in this analysis in a very non-uniform way. EFT parameters $b_2, \alpha_0, \alpha_1, c_0$ are much better constrained with SBP, $b_1, b_{\mathcal{G}_2}, c_2, b_4$ show moderate improvements, while b_{Γ_3} and α_2 are less constrained now. In the latter case, the priors are not informative enough, and at the same time the power spectrum data alone cannot break the remaining degeneracies $b_4 - \alpha_2$ and $b_{\mathcal{G}_2} - b_{\Gamma_3}$, which results in worse constraints. Note that our constraint of b_1 is driven by linear redshift-space distortions in the data and not by the priors themselves. The priors only help break degeneracies between b_1, σ_8 and other nuisance parameters that appear in the non-linear regime at large wavenumbers.

The posteriors of cosmological parameters ω_{cdm} and σ_8

narrow quite noticeably as a result of using the SBP. We find no improvement on H_0 . The improvement in the case of ω_{cdm} is $\approx 30\%$. The σ_8 constraint improves by more than 60%. This is achieved by breaking the degeneracy between σ_8 and the redshift space counterterms. The strongest residual degeneracy that σ_8 has after applying the SBP is with b_{Γ_3}, b_2 and $b_{\mathcal{G}_2}$.

6.2. On the consistent choice of priors

A comment is in order on the prior choice. Overall, the priors associated with the CLASS-PT and velocileptor [101, 102] codes are consistent with the HOD-based priors and with the posteriors from the BOSS data, see fig. 11. One can also compare these priors choices with the one associated with the PyBird code [10]. While we defer a detailed comparison to a separate paper, let us make a few comments which may be relevant for the interpretation of results obtained with this code. PyBird analyses assume $b_4 = 0$ and a prior on α_2 (proportional to $c_{e,quad}$ of [10])

$$\alpha_2 \sim \mathcal{N}(0, 0.5^2) \quad , \quad (82)$$

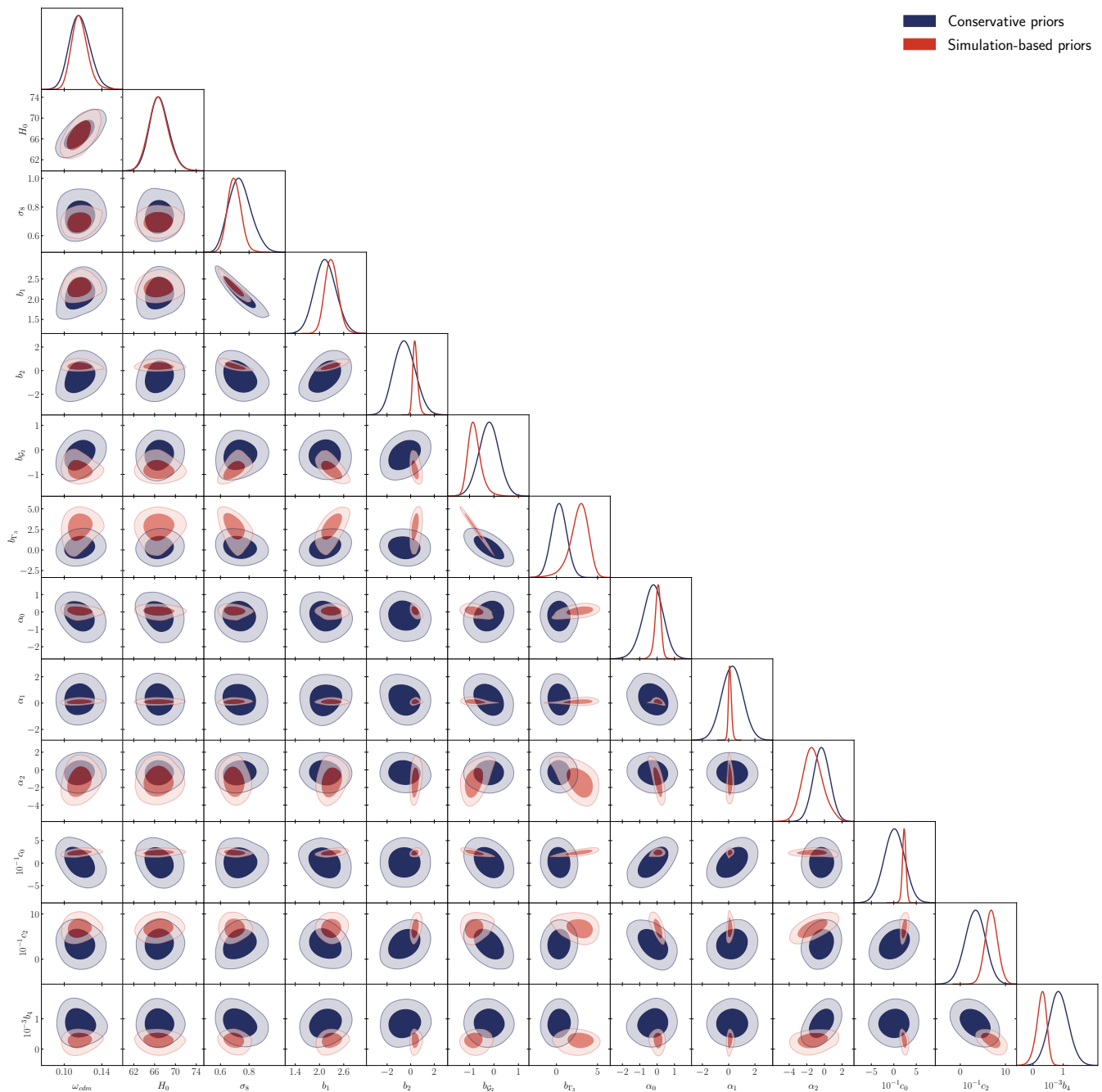


FIG. 11. Cosmological and EFT parameters extracted from the BOSS NGCz1 data with the usual conservative priors and the SBP derived in this work.

for their LOWZ sample¹² similar to our z1. Besides, [10] do not account for the effects of exclusion of dark matter halos and galaxies [126, 132] (i.e. non-Poissonian sampling) in their prior on the constant stochasticity param-

eter $c_{\epsilon,1} = \alpha_0$, for which they assume

$$\alpha_0 \sim \mathcal{N}(0, 0.1^2) ,$$

based on the fiber collision corrections only. Both our HOD samples and the actual measurements from the data strongly rule out this assumption.

The small number 0.5 in (82) is also challenging to justify from the theoretical perspective. In addition, such an

¹² Note that the values of number densities assumed in [10] do not match the ones measured from data.

BOSS NGCz1 $P_0 + P_2$ with conservative priors					BOSS NGCz1 $P_0 + P_2$ with simulation-based priors				
Param	best-fit	mean $\pm\sigma$	95% lower	95% upper	Param	best-fit	mean $\pm\sigma$	95% lower	95% upper
ω_{cdm}	0.1122	0.1167 $^{+0.01}_{-0.012}$	0.09525	0.1385	ω_{cdm}	0.1193	0.1165 $^{+0.0077}_{-0.0094}$	0.09956	0.134
H_0	66.15	66.92 $^{+1.8}_{-2}$	63.17	70.76	H_0	67.43	66.77 $^{+1.8}_{-2}$	63	70.63
$\ln(10^{10} A_s)$	3.031	2.862 $^{+0.22}_{-0.25}$	2.399	3.34	$\ln 10^{10} A_s$	2.783	2.752 $^{+0.15}_{-0.16}$	2.445	3.06
b_1	1.941	2.139 $^{+0.26}_{-0.28}$	1.624	2.669	b_1	2.216	2.298 $^{+0.15}_{-0.18}$	1.974	2.629
b_2	-1.102	-0.513 $^{+0.87}_{-0.98}$	-2.262	1.284	b_2	0.2628	0.3964 $^{+0.18}_{-0.25}$	-0.02381	0.8499
$b_{\mathcal{G}_2}$	-0.3471	-0.2069 $^{+0.43}_{-0.42}$	-1.039	0.628	$b_{\mathcal{G}_2}$	-0.7999	-0.7897 $^{+0.21}_{-0.31}$	-1.313	-0.207
b_{Γ_3}	0.1284	0.3103 $^{+0.95}_{-0.96}$	-1.561	2.183	b_{Γ_3}	2.77	2.72 $^{+1.3}_{-0.9}$	0.2394	4.921
α_0	-0.2216	-0.2489 $^{+0.62}_{-0.57}$	-1.444	0.9123	α_0	0.09192	0.04499 $^{+0.19}_{-0.16}$	-0.3444	0.4149
α_1	0.4947	0.2724 $^{+0.81}_{-0.82}$	-1.309	1.88	α_1	0.1218	0.1043 $^{+0.11}_{-0.13}$	-0.1361	0.3694
α_2	-0.4268	-0.3283 $^{+0.96}_{-0.96}$	-2.2	1.565	α_2	-1.854	-1.32 $^{+1.1}_{-1.2}$	-3.506	1.09
$10^{-1}c_0$	0.9671	0.1047 $^{+2.3}_{-2.3}$	-4.496	4.637	$10^{-1}c_0$	2.167	2.309 $^{+0.43}_{-0.42}$	1.451	3.187
$10^{-1}c_2$	4.127	3.306 $^{+2.3}_{-2.2}$	-1.187	7.731	$10^{-1}c_2$	6.098	6.878 $^{+1.4}_{-1.5}$	4.066	9.757
$10^{-3}b_4$	0.7137	0.852 $^{+0.32}_{-0.33}$	0.2073	1.506	$10^{-3}b_4$	0.3993	0.2749 $^{+0.2}_{-0.15}$	-0.09049	0.6056
Ω_m	0.3076	0.3104 $^{+0.018}_{-0.021}$	0.2726	0.3496	Ω_m	0.3116	0.3117 $^{+0.015}_{-0.019}$	0.2779	0.3469
σ_8	0.7802	0.7383 $^{+0.07}_{-0.087}$	0.5912	0.8929	σ_8	0.7197	0.6965 $^{+0.046}_{-0.049}$	0.6036	0.7898

TABLE II. Best-fits and 1d marginalized limits for cosmological and EFT parameters from BOSS NGCz1 data. The lower two rows show derived cosmological parameters.

overoptimistic prior on α_2 is not supported by data and simulations. In particular, this is evidenced from figures 25 and 26 of [10], which display a tension between the actual posteriors for $c_{e,quad}$ and the prior for this parameter. Arguments for non-zero b_4 based on the relevance of the two-loop corrections were given in [98, 99, 117]. The large value of the $k^2 P_{11}$ quadrupole counterterm from data suggests a sizeable $k^4 P_{11}$ correction as well.

In addition to these arguments, our HOD-based priors and posteriors presented in fig. 11 suggest that the prior from eq. (82) and the choice $b_4 = 0$ are inconsistent with a large sample of BOSS-like HOD models. This sample includes HODs for the PT Challenge mocks. We caution against overoptimistic priors as they can bias parameter estimation.

6.3. Results for full BOSS DR12

We reanalyze now the power spectrum multipoles from the complete BOSS DR12 data.¹³ This includes four data slices: NGCz1, SGCz1, NGCz3 and SGCz3. The results are presented in fig. 2 and table III. For comparison, we also show the *Planck* 2018 results for the Λ CDM+ m_ν model which is appropriate for comparison with the BOSS EFT full-shape likelihood [9, 98]. We see that the SBPs improve ω_{cdm} and σ_8 limits by $\approx 30\%$ and $\approx 60\%$, respectively. As before, the constraint on H_0 does not improve noticeably. Our final results nominally suggest a $\approx 5\sigma$ tension with *Planck* for σ_8 , in agreement with the recent analysis of the BOSS data [13] that used an extended dataset, consisting of the post-reconstructed BAO [143], real-space power spectrum proxy Q_0 [116], the bispectrum multipoles [58], and the galaxy-CMB lensing cross correlations [56].

It is interesting to compare our results with those

¹³ We also include the hexadecapole P_4 here using the methodology of [90].

BOSS P with conservative priors					BOSS P with simulation-based priors				
Param	best-fit	mean $\pm\sigma$	95% lower	95% upper	Param	best-fit	mean $\pm\sigma$	95% lower	95% upper
ω_{cdm}	0.1252	$0.1268^{+0.0062}_{-0.0068}$	0.114	0.1398	ω_{cdm}	0.1276	$0.1269^{+0.0045}_{-0.0046}$	0.1181	0.1363
H_0	68.64	$68.76^{+1.2}_{-1.3}$	66.29	71.27	H_0	67.61	$68.79^{+1.1}_{-1.3}$	66.47	71.22
$\ln(10^{10} A_s)$	2.805	$2.75^{+0.12}_{-0.13}$	2.504	2.994	$\ln(10^{10} A_s)$	2.544	$2.533^{+0.092}_{-0.084}$	2.354	2.712
$b_1^{(1)}$	2.236	$2.319^{+0.16}_{-0.17}$	1.997	2.648	$b_1^{(1)}$	2.675	$2.674^{+0.11}_{-0.12}$	2.443	2.9
$b_2^{(1)}$	-1.291	$-1.1^{+0.94}_{-1}$	-3.032	0.8797	$b_2^{(1)}$	0.6511	$0.8556^{+0.21}_{-0.31}$	0.3716	1.405
$b_{\mathcal{G}_2}^{(1)}$	-0.05125	$0.01557^{+0.47}_{-0.46}$	-0.9242	0.9429	$b_{\mathcal{G}_2}^{(1)}$	-0.9653	$-0.8646^{+0.23}_{-0.32}$	-1.383	-0.2882
$b_1^{(2)}$	2.386	$2.462^{+0.15}_{-0.17}$	2.143	2.79	$b_1^{(2)}$	2.758	$2.774^{+0.12}_{-0.12}$	2.531	3.016
$b_2^{(2)}$	-0.5497	$0.02503^{+0.95}_{-0.97}$	-1.876	1.949	$b_2^{(2)}$	0.835	$0.9431^{+0.21}_{-0.32}$	0.4362	1.516
$b_{\mathcal{G}_2}^{(2)}$	-0.3622	$-0.1452^{+0.5}_{-0.47}$	-1.117	0.8138	$b_{\mathcal{G}_2}^{(2)}$	-1.056	$-1.078^{+0.19}_{-0.26}$	-1.537	-0.5721
$b_1^{(3)}$	2.162	$2.218^{+0.14}_{-0.15}$	1.932	2.513	$b_1^{(3)}$	2.453	$2.47^{+0.099}_{-0.11}$	2.262	2.681
$b_2^{(3)}$	-0.7661	$-0.2975^{+0.8}_{-0.9}$	-1.975	1.431	$b_2^{(3)}$	0.5009	$0.5357^{+0.15}_{-0.21}$	0.1841	0.9123
$b_{\mathcal{G}_2}^{(3)}$	-0.44	$-0.1732^{+0.39}_{-0.4}$	-0.9581	0.6304	$b_{\mathcal{G}_2}^{(3)}$	-0.9306	$-0.9451^{+0.16}_{-0.24}$	-1.344	-0.5018
$b_1^{(4)}$	2.201	$2.243^{+0.14}_{-0.15}$	1.958	2.54	$b_1^{(4)}$	2.484	$2.468^{+0.1}_{-0.11}$	2.257	2.684
$b_2^{(4)}$	-0.2233	$-0.07458^{+0.84}_{-0.92}$	-1.805	1.69	$b_2^{(4)}$	0.5287	$0.5722^{+0.16}_{-0.22}$	0.1896	0.9783
$b_{\mathcal{G}_2}^{(4)}$	0.04152	$0.2367^{+0.41}_{-0.42}$	-0.5914	1.076	$b_{\mathcal{G}_2}^{(4)}$	-1.058	$-0.9933^{+0.19}_{-0.28}$	-1.452	-0.4821
Ω_m	0.3146	$0.317^{+0.012}_{-0.013}$	0.2928	0.3419	Ω_m	0.3282	$0.3155^{+0.0095}_{-0.011}$	0.2962	0.3364
σ_8	0.7422	$0.7288^{+0.04}_{-0.045}$	0.6458	0.8141	σ_8	0.6661	$0.6632^{+0.027}_{-0.027}$	0.6086	0.7212
S_8	0.7726	$0.749^{+0.048}_{-0.048}$	0.6593	0.8459	S_8	0.7114	$0.679^{+0.031}_{-0.035}$	0.6186	0.7466

TABLE III. Best-fits and 1d marginalized limits for cosmological and EFT parameters from BOSS data. For EFT parameters, we display the linear and quadratic bias parameters only. The lower two rows show derived cosmological parameters. The bias parameters' superscripts (1), (2), (3), (4) correspond to NGCz3, SGCz3, NGCz1, and SGCz1 samples, respectively.

of [13]. This analysis assumed conservative priors on EFT parameters as in eqs. (79-81). Their final results for Ω_m and σ_8 are consistent with ours both in terms of errorbars and the mean values. The improvement on cosmological parameters from adding more data while keeping the conservative priors are similar to the results that we get from the power spectrum alone, but with the better priors. This confirms the argument that the marginalization over EFT parameters leads to a strong degradation of constraining power [20, 144].

Our results also suggest that the σ_8 anomaly was present at a significant level already in the galaxy power spectrum, but its signal was absorbed into the EFT parameters. Once the freedom in the variation of EFT parameters is reduced, the evidence for the anomaly in the power spectrum increases. This effect was first pointed out in the analysis of [12], which found that fitting the BOSS galaxy power spectrum with the *Planck* cosmology

requires values of bias parameters that are not consistent with dark matter halo expectations. We will comment on this point in detail shortly.

A comment on the primordial spectral tilt is in order. We have fixed this parameter to the *Planck* best-fit Λ CDM value $n_s = 0.9649$ in our main analysis. To understand the impact of the SBP on measuring this parameters, we have re-done our main P_ℓ analysis with free n_s and report the results in Appendix G. We have found that the SBP somewhat reduce the preference of the BOSS data for low n_s values, and alleviate the discrepancy with *Planck* from $\approx 1.1\sigma$ to $\approx 0.9\sigma$. The best-fit value of n_s from the SBP analysis matches the *Planck* value quite closely, suggesting that the remaining 0.9σ shift above is a likely projection effect. The SBP improve the limit on n_s (and other cosmological parameters except σ_8) only marginally, by $\lesssim 10\%$. The structure growth parameter measurement, however, improves drastically,

just like in our baseline analysis, from $\sigma_8 = 0.704^{+0.044}_{-0.049}$ to $\sigma_8 = 0.660^{+0.026}_{-0.03}$.

At this point one may wonder how much the addition of other data, such as the BAO, real-space proxy Q_0 , the bispectrum can help improve cosmological constraints. Using the full dataset of [12], we found a very significant improvement in cosmological constraints. In particular, for the same choices as in the baseline P_ℓ +BAO+ Q_0 + B_0 analysis of [12], we find

$$\begin{aligned}\sigma_8 &= 0.6511 (0.6508)_{-0.018}^{+0.019}, \\ \omega_{cdm} &= 0.1221 (0.1211)_{-0.0045}^{+0.004}, \\ H_0 &= 68.05 (67.82)_{-0.8}^{+0.79}, \\ \Omega_m &= 0.312 (0.3119)_{-0.0088}^{+0.0078}.\end{aligned}\tag{83}$$

where we quote best-fit values in the parentheses. The posteriors are also shown in fig. 2. These compare favorably with the P_ℓ +BAO+ Q_0 + B_0 results obtained under the conservative priors from [12]:

$$\begin{aligned}\sigma_8 &= 0.7221 (0.7248)_{-0.037}^{+0.032}, \\ \omega_{cdm} &= 0.1262 (0.1242)_{-0.0059}^{+0.0053}, \\ H_0 &= 68.32 (68.09)_{-0.86}^{+0.83}, \\ \Omega_m &= 0.3197 (0.3176)_{-0.01}^{+0.0095}.\end{aligned}\tag{84}$$

In particular, we still see a significant ($\approx 80\%$) improvement on σ_8 , along with a $\approx 30\%$ improvement on ω_{cdm} . We have found that most of the additional improvements w.r.t. the P_ℓ SBP analysis is produced by the bispectrum. We believe that these extra improvements are due to the fact that the degeneracy directions between the EFT parameters in the bispectrum are different from those implied by the priors, and hence combining the two allows one to gain more information from the degeneracy breaking.

Nominally, the growth of structure in the P_ℓ +BAO+ Q_0 + B_0 analysis is constrained to better than 3%. However, we caution these limits are preliminary. At our new level of precision, we may have to re-calibrate the scale cuts and analyses choices for the bispectrum and Q_0 made in [12]. This requires a detailed study which we defer to a separate publication.

6.4. On the origin of the structure growth anomaly in the context of the simulation-based priors

In this section we report the results of our investigation of the origin of the low σ_8 value in our analysis. We limit

ourselves here with the main conclusions of our study, and refer an interested reader to Appendix F for technical details.

The first relevant observation that one can make is that the posteriors for b_1 are dominated by the likelihood. Although our b_1 prior is peaked at low b_1 , it does not “pull” the posterior values of this parameter to lower values. Indeed, our posteriors for b_1 are much narrower than the width of the prior, and the shape of the b_1 prior is quite flat in the range $b_1 \in [2, 3]$, relevant for the BOSS data.

The second relevant observation is that the $\approx 2\sigma$ shift of the mean value of σ_8 due to SBP is driven by the high- k end of the data. To verify this we re-analyzed the BOSS data with the conservative priors and SBP with a momentum cut $k_{\max} = 0.1 \text{ hMpc}^{-1}$, and found highly consistent results, $\sigma_8 = 0.696^{+0.044}_{-0.055}$ (conserv. priors) and $\sigma_8 = 0.677^{+0.033}_{-0.039}$ (SBP), with the difference between the means at the level of $\sim 0.5\sigma$.

Investigating the high- k part of the data, we found that it can be fitted with a high value of $\sigma_8 \approx 0.74$, but this requires highly unlikely values of the EFT parameters. Specifically, as can be appreciated from table III, the high σ_8 fit requires $b_2^{\text{NGCz3}} \approx -1$ and $b_1^{\text{NGCz3}} \approx 2.2$, which are impossible to reproduce within the HOD framework, i.e. we have no samples with these values.¹⁴ The tension further extends to other EFT parameters, such as the stochastic counterterms α_0 and α_2 . The high σ_8 fit for NGCz3 requires $\alpha_0 \approx 0.4$ and $\alpha_2 \approx -2$, which correspond to HODs with unlikely large satellite fractions. (The NGCz1 parameters quoted in table II exhibit a similar behavior.) All in all, the likelihood of EFT parameters required to fit the data at $\sigma_8 = 0.74$ appears to be quite low from the HOD modeling viewpoint.

Once the EFT parameters are restricted by the HOD-based priors, it becomes impossible to maintain a good fit to data at large σ_8 values. The lower σ_8 values we obtain appear to be “a compromise” between the HOD priors and the data likelihood. This can be estimated on the basis of the χ^2 statistics. If we consider only the likelihood of the galaxy $P_{0,2}$ data, the raw χ_{like}^2 of the best fit at $\sigma_8 = 0.67$ from the SBP analysis is notably worse

¹⁴ The impossibility of these values is dictated by the shape of the HOD for Luminous Red Galaxies [129].

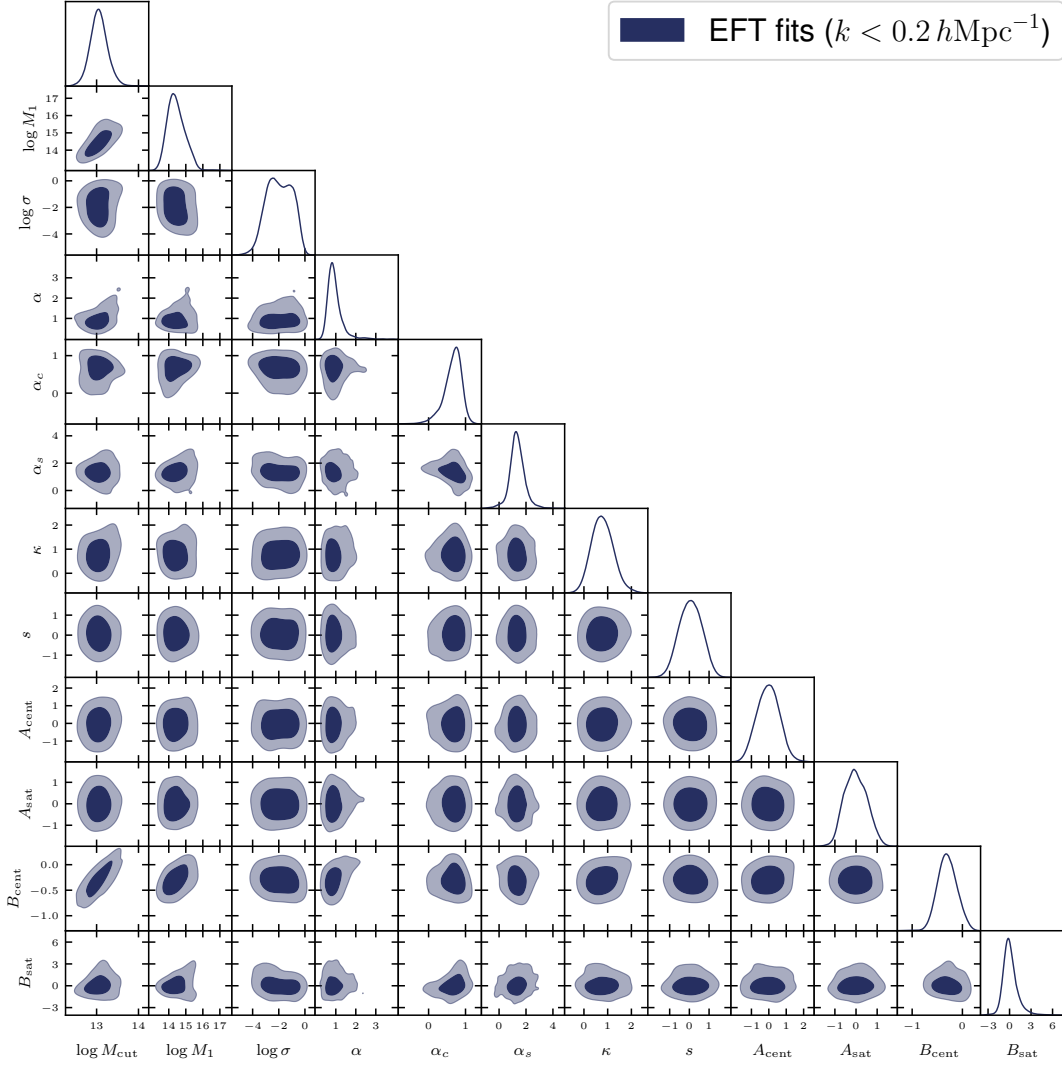


FIG. 12. Constraints on HOD parameters of the BOSS NGCz3 galaxies from the EFT parameters of the galaxy power spectrum.

than that of the conservative analysis with $\sigma_8 = 0.74$:

$$\Delta\chi_{\text{like}}^2 = \chi_{\text{like}}^2 \Big|_{\text{SBP}} - \chi_{\text{like}}^2 \Big|_{\text{cons.}} \approx 8. \quad (85)$$

However, if we compute the “effective χ^2 ” of the prior as $\chi_{\text{eff, prior}}^2 = -2 \ln \mathcal{L}_{\text{EFT}}$ (with \mathcal{L}_{EFT} being the likelihood of the EFT parameters from our sample estimated by the normalizing flow), we find a very significant improvement over the conservative analysis,

$$\Delta\chi_{\text{eff, prior}}^2 = \chi_{\text{eff, prior}}^2 \Big|_{\text{SBP}} - \chi_{\text{eff, prior}}^2 \Big|_{\text{cons.}} \approx -391. \quad (86)$$

This large improvement¹⁵ mostly comes from the very unlikely values of the $\{b_1, b_2\}$ pair (290 units of the effective

χ^2). The rest is distributed between the RSD counterterms (33 units) and the real space EFT parameters (68).

As a final note, it is worth pointing out that 6.05 out of 8 units of the χ^2 difference between the SBP and conservative best-fits in eq. (85) stem from the power spectrum monopole P_0 data, which is not sensitive to σ_8 in linear theory. Taken together with the difference in the inferred values of $b_1\sigma_8$ between the conservative and SBP analyses (see table III), the dependence of our results

confidence levels for 10 parameters (as in our $P_{0,2}$ analysis), $\Delta\chi^2 = 11.5$ (68%), 18.4 (95%), as follows from the χ^2 distribution.

¹⁵ As a point of comparison, one can use $\Delta\chi^2$ as a function of

on the high- k end, this suggest that the shifts and improvements in σ_8 constraints that we have obtained have resulted from non-linear one-loop corrections. Indeed, in principle, the one-loop corrections break the degeneracy between b_1 and σ_8 (see e.g. [99]), but this mechanism is inefficient at the power spectrum level because of the degeneracy with the bias parameters. The degeneracy with the non-linear bias parameters also affects the extraction of $b_1\sigma_8$ from the monopole data. The HOD priors provide non-perturbative information on the relations between the bias parameters, thereby breaking this degeneracy, and allowing to extract the extra σ_8 information from the amplitude of the one-loop power spectrum monopole contributions.

6.5. Learning galaxy-halo connection from EFT parameters on large scales

One interesting application of our joint sample of EFT and HOD parameters is that we can build a model for the mapping $\{\theta_{\text{EFT}}\} \rightarrow \{\theta_{\text{HOD}}\}$ and use it to convert the MCMC samples for EFT parameters from data into HOD samples. This approach allows us to constrain galaxy properties from large scales, and get insights into the optimal HOD parameters for a given galaxy population even without carrying out a full HOD-based SBI on the data. This approach also provides a consistency test between large and small scale galaxy clustering analyses.

As an concrete example, we have built a model for the distribution of HOD parameters conditioned on the EFT parameters following the methodology of [36], and generated HOD samples from the MCMC chains for BOSS NGCz3 galaxies. This sample was previously analyzed with various HOD-based SBI techniques, e.g. [32, 60]. The resulting corner plot is shown in fig. 12. The posteriors of HOD parameters are quite wide, which is expected given that they are constrained using the large scale modes only. Nevertheless, our HOD samples for threshold host halo masses M_{cut} and M_1 , and some other parameters, are narrower than the priors. Besides, we also see a marginal evidence in favour of a negative assembly bias parameter for centrals B_{sat} .

Our results are consistent with those of the HOD-based analysis utilizing the density split statistic [60]. We note, however, that in contrast to [60] we use only large scales ($k_{\text{max}} = 0.2 \text{ hMpc}^{-1}$), our HOD model is more flexi-

ble (i.e. we have additional assembly bias parameters $A_{\text{cent/sat}}$) and our priors for HOD parameters are wider than those considered in [60]. These factors resulted in the reduction of constraining power as compared to [60].

7. DISCUSSION AND OUTLOOK

We have generated the largest to date sample of EFT parameters for galaxies from HOD-based simulations. We suggest to use this sample as a prior in EFT-based full shape analyses. Our main results are listed in Sec. 2. Let us now compare our results with the literature, discuss the main lessons learned, and outline the directions for future improvement.

It has been known for a long time that the EFT-based full-shape constraints can improve dramatically with better priors on EFT parameters. For example, the constraint on the amplitude of primordial fluctuations A_s (strongly correlated with σ_8 in full-shape analysis), improves by more than a factor of 2 at $k_{\text{max}} = 0.2 \text{ hMpc}^{-1}$ once the EFT parameters are fixed [144]. In this work we found a similar, though slightly less impressive improvement on σ_8 . Therefore, our results are not so surprising. The other parameters, such as ω_{cdm} and H_0 do not respond to SBP as strongly as suggested by [144] because the eventual distribution of the EFT parameters is not narrow enough to break degeneracies relevant for these parameters. (Note that [144] assumed the perfect knowledge of all EFT parameters, which does not take place for HOD models.)

Naively, our results appear in conflict with those of ref. [30], which analyzed the same data sample as us with the HOD-based emulator, but found very minor improvements at $k_{\text{max}} \simeq 0.2 \text{ hMpc}^{-1}$ over the usual EFT analysis with conservative priors. We argue, however, that there is no contradiction between our work and ref. [30] because many technical aspects our analyses are quite different. First, [30] used an HOD-based emulator for the power spectrum only, while here we calibrate our priors from the entire galaxy field, including higher-order correlations. This way our priors include clustering information beyond the two point function. Second, [30] marginalizes over the additional constant shot noise contribution similar to our α_0 . This parameter appears to be correlated with $\ln(10^{10} A_s)$, which introduces additional uncertainties in the σ_8 limit. In our approach we assume

that α_0 is fully determined by HOD models, which provides extra information. Third, we use an extended HOD model with assembly bias parameters. It will be interesting to compare our approach with that of ref. [30] with similar analysis settings.

In terms of the final error bars, our results appear to be similar with those of simulation-based analyses of refs. [32, 60, 145]. For instance, [145] finds a 5% constraint on $f\sigma_8$ from the BOSS LOWZ sample, which is similar to our $\approx 6\%$ constraint from the analogous NGCz1 data chunk. We also find $\sim 3\%$ constraint on σ_8 from the BOSS galaxy power spectrum, which is similar to the 2.3% limit from [32]. [60] applied their pipeline to the BOSS CMASS data only, but the final constraints appear to be similar to ours in terms of the σ_8 error-bar. Note however, that our datasets are very different. While [32] uses wavelet scattering transforms, our main measurement is based purely on the two-point function. This suggests an interesting hypothesis that the small-scale beyond the two point function information in HOD-based SBI actually mostly constrains the HOD parameters. The better knowledge of HOD parameters then leads to a better cosmological parameter estimation from large scales. This picture suggests that the bulk of the cosmological information is stored in the large-scale power spectrum. It will be interesting to test this hypothesis in future.

The posteriors of our SBP-based analyses of BOSS are consistent with the traditional ones obtained with conservative priors. The priors mostly change the widths of the cosmological parameter contours, while their positions remain mostly unaffected. In particular, our analyses confirm reports of the σ_8 tension from the earlier large-scale EFT analyses of the BOSS data with conservative priors. This additionally confirms that the preference for the low σ_8 in the BOSS data is not driven by priors. It will be interesting to see if the significant tension continues to be present in the DESI data.

We note that our priors were derived for the HOD designed for luminous red galaxies. Other galaxy types, such as emission line galaxies (ELGs), require a different form of the HOD, and hence our priors may not be applicable to them. In addition, the HOD models do not include physical effects such as the baryonic feedback and the dependence on the past evolution. Therefore, it will be important to extend our priors to new galaxy types and include additional effects beyond the HOD models.

This suggests that the EFT-based analysis of public data on ELGs and quasars from eBOSS [136, 137, 146, 147] with simulation priors should be among the first extensions of our work. In addition, it will be interesting to test our priors against other galaxy formation approaches, such as hydrodynamical simulations and abundance matching.

Our sample of EFT and HOD parameters can be used to build conditional models, which can help understand the physics behind EFT parameters [36]. These conditional models can also be used to translate results of the SBI to EFT-based analyses and vice versa, which can be a useful tool to test the consistency of large-scale and small-scale parameter estimation pipelines. We leave this and other research directions for future work.

ACKNOWLEDGMENTS

We thank Ryan Abbott, Kazuyuki Akitsu, Stephen Chen, Will Detmold, Cora Dvorkin, Yosuke Kobayashi, Siddharth Mishra-Sharma, Chirag Modi, Azadeh Moradinezhad, Oliver Philcox, Marko Simonović, Fabian Schmidt, Uros Seljak, Jamie Sullivan, Masahiro Takada, Georgios Valogiannis, and Matias Zaldarriaga for useful discussions. This work is supported by the National Science Foundation under Cooperative Agreement PHY-2019786 (The NSF AI Institute for Artificial Intelligence and Fundamental Interactions, <http://iaifi.org/>). This material is based upon work supported by the U.S. Department of Energy, Office of Science, Office of High Energy Physics of U.S. Department of Energy under grant Contract Number DE-SC0012567. AO acknowledges financial support from the Swiss National Science Foundation (grant no CRSII5_193826). MWT acknowledges financial support from the Simons Foundation (Grant Number 929255).

DATA AVAILABILITY

Our work is based on the publicly available Abacus simulation [105] <https://abacussummit.readthedocs.io/en/latest/> and Quijote simulation data [86] <https://quijote-simulations.readthedocs.io/en/latest/>.

Appendix A: Time Sliced Perturbation Theory for Shifted Correlators

In this section we carry our IR resummation for the correlators of the shifted fields using time-sliced perturbation theory [78–81].

We start our review of TSPT with the integral equations for Eulerian perturbation theory of the pressureless perfect fluid in Fourier space [111],

$$\begin{aligned} \partial_\eta \delta_{\mathbf{k}} - \Theta_{\mathbf{k}} &= \int [dp]^2 \delta^{(3)}(\mathbf{k} - \mathbf{p}_{12}) \alpha(\mathbf{p}_1, \mathbf{p}_2) \Theta_{\mathbf{p}_1} \delta_{\mathbf{q}_2}, \\ \partial_\eta \Theta_{\mathbf{k}} + \frac{1}{2} \Theta_{\mathbf{k}} - \frac{3}{2} \delta_{\mathbf{k}} &= \int [dp]^2 \delta^{(3)}(\mathbf{k} - \mathbf{q}_{12}) \beta(\mathbf{p}_1, \mathbf{p}_2) \Theta_{\mathbf{p}_1} \Theta_{\mathbf{p}_2}, \end{aligned} \quad (\text{A1})$$

where $[dp] = d^3p/(2\pi)^3$, $\delta^{(3)} = (2\pi)^3 \delta_D^{(3)}$, and the non-linear kernels

$$\begin{aligned} \alpha(\mathbf{k}_1, \mathbf{k}_2) &\equiv \frac{(\mathbf{k}_1 + \mathbf{k}_2) \cdot \mathbf{k}_1}{k_1^2}, \\ \beta(\mathbf{k}_1, \mathbf{k}_2) &\equiv \frac{(\mathbf{k}_1 + \mathbf{k}_2)^2 (\mathbf{k}_1 \cdot \mathbf{k}_2)}{2k_1^2 k_2^2}. \end{aligned} \quad (\text{A2})$$

The density field δ can always be expressed in terms of Θ as

$$\begin{aligned} \delta_{\mathbf{k}} &= \delta[\Theta; \eta, \mathbf{k}] \equiv \\ &\sum_{n=1}^{\infty} \frac{1}{n!} \int [dp]^n K_n^{(r)}(\mathbf{p}_1, \dots, \mathbf{p}_n) \delta^{(3)}(\mathbf{k} - \mathbf{p}_{1\dots n}) \prod_{j=1}^n \Theta(\eta, \mathbf{p}_j), \end{aligned} \quad (\text{A3})$$

with $K_1^{(r)} = 1$. One can use representation (A3) to eliminate the density field from Eq. (A1). The final equation for the velocity divergence only reads:

$$\begin{aligned} \partial_\eta \Theta(\eta, \mathbf{k}) &= \mathcal{I}[\Theta] \equiv \\ &\sum_{n=1}^{\infty} \frac{1}{n!} \int [dq]^n I_n^{(r)}(\mathbf{p}_1, \dots, \mathbf{p}_n) \delta^{(3)}(\mathbf{k} - \mathbf{p}_{1\dots n}) \prod_{j=1}^n \Theta(\eta, \mathbf{p}_j), \end{aligned} \quad (\text{A4})$$

with the growing mode condition $I_1^{(r)} \equiv 1$. The kernels $K_n^{(r)}$ and $I_n^{(r)}$ can be calculated recursively [80].

The central object of TSPT is the generating functional for the cosmological fields velocity divergence and density fields Θ and δ :

$$\begin{aligned} \mathcal{Z}[J, J_\delta; \eta] &= \int [D\Theta] \mathcal{P}[\Theta; \eta] \exp\{J\Theta + J_\delta \delta\}, \\ J\Theta + J_\delta \delta &\equiv \int [dk] (\Theta_{\mathbf{k}} J(-\mathbf{k}) + \delta[\Theta; \eta, \mathbf{k}] J_\delta(-\mathbf{k})). \end{aligned} \quad (\text{A5})$$

Functional derivatives with respect to the sources J and J_δ produce equal-time correlation functions of Θ and δ . \mathcal{P} above is the probability density functional that satisfies the Liouville equation,

$$\frac{\partial}{\partial \eta} \mathcal{P}[\Theta; \eta] + \int [dk] \frac{\delta}{\delta \Theta(\mathbf{k})} (\mathcal{I}[\Theta; \eta] \mathcal{P}[\Theta; \eta]) = 0. \quad (\text{A6})$$

In perturbation theory one can expand $\mathcal{P}[\Theta; \eta]$ as

$$\begin{aligned} \mathcal{P}[\Theta; \eta] &= \mathcal{N}^{-1} \exp\{-W\}, \\ W &\equiv \sum_{n=1}^{\infty} \frac{1}{n!} \int [dk]^n \Gamma_n^{(r) \text{tot}}(\eta; \mathbf{k}_1, \dots, \mathbf{k}_n) \prod_{j=1}^n \Theta_{\mathbf{k}_j}, \end{aligned} \quad (\text{A7})$$

where \mathcal{N} is a normalization constant. Substituting this representation into (A6) and using Eq. (A4) we obtain the following chain of equations on the vertices,

$$\begin{aligned} &\partial_\eta \Gamma_n^{(r) \text{tot}}(\eta; \mathbf{k}_1, \dots, \mathbf{k}_n) \\ &+ \sum_{m=1}^n \frac{1}{m!(n-m)!} \sum_{\sigma} I_m^{(r)}(\eta; \mathbf{k}_1, \dots, \mathbf{k}_m) \\ &\times \Gamma_{n-m+1}^{(r) \text{tot}}(\eta; \sum_{l=1}^m \mathbf{k}_{\sigma(l)}, \mathbf{k}_{\sigma(m+1)}, \dots, \mathbf{k}_{\sigma(n)}) \\ &= \delta_D^{(3)}(\mathbf{k}_{1\dots n}) \int [dp] I_{n+1}^{(r)}(\eta; \mathbf{p}, \mathbf{k}_1, \dots, \mathbf{k}_n). \end{aligned} \quad (\text{A8})$$

The solution to this equation is decomposed into two pieces,

$$\Gamma_n^{(r) \text{tot}} = \Gamma_n^{(r)} + C_n^{(r)}, \quad (\text{A9})$$

where $\Gamma_n^{(r)}$ is the homogeneous solution, while $C_n^{(r)}$ are ‘‘counterterms’’ that stem from the inhomogeneous equations. The latter are irrelevant for IR resummation so we will ignore them in what follows.

For the Gaussian initial the vertices $\Gamma_n^{(r)}$ can be computed exactly. In particular, their time-dependence factorizes,

$$\Gamma_n^{(r)} = \delta^{(3)}(\mathbf{k}_{1\dots n}) \frac{\bar{\Gamma}_n^{(r)}}{g^2(\eta)}, \quad (\text{A10})$$

where $g(\eta) \equiv D_+(\eta)$ plays a role of the coupling constant in TSPT. The key observation that makes TSPT a useful representation is that IR singularities of Eulerian perturbation theory at low momenta are contained in $\bar{\Gamma}_n^{(r)}$. The second important fact is that only these vertices depend on the initial power spectrum, in contrast to $K_n^{(r)}$ and C_n . This allows one to identify enhanced diagrams and resum them to all orders in perturbation theory. For

the Θ auto spectrum, this leads to the following one-loop IR resummed expression:

$$P_{YY}^{1\text{-loop,IR}}(k) = P_{YY}^{\text{tree}}[e^{-\hat{\mathcal{S}}}(1 + \mathcal{S})P_{11}] + P_{YY}^{1\text{-loop}}[e^{-\hat{\mathcal{S}}}P_{11}], \quad (\text{A11})$$

where $\{YY\} = \{\Theta\Theta\}$, and the operator $\hat{\mathcal{S}}$ is formally defined as

$$\hat{\mathcal{S}}P_{11} = \int_{|\mathbf{p}| \leq \Lambda_{IR}} P_{11} \frac{(\mathbf{k} \cdot \mathbf{p})^2}{p^4} (1 - \cosh(\mathbf{p} \nabla_{k'})) P_{11}(k') \Big|_{k'=k} \quad (\text{A12})$$

This formula requires some explanation. The original works on TSPT assumed a decomposition of the linear matter power spectrum into the wiggly and smooth parts to separate the BAO from the rest of the spectrum. While the latter makes IR resummation conceptually simple, this separation is, strictly speaking, is only an approximation. But the TSPT formulas can be used even without performing the actual split. In this case, the split should be considered a formal tool for power counting. Using the notations of ref. [79], from the formal point of view, one can always “pull” P_{nw} through the operator $e^{-\hat{\mathcal{S}}}$ back to P_w because it does not change the IR power counting. Analogously, the relevant expressions for the IR enhancements in vertices $\Gamma_n^{(r)}$ can be rewritten in terms of the finite differences of the total linear power spectra. Therefore, the wiggly-smooth split is not a cornerstone part of the TSPT formalism.

The integral that appears in eq. (A24) can be transformed to position space, in which case the final IR resummed expression will be identical to that of Lagrangian EFT [79]. That said, we will continue with the wiggly-smooth split in what follows because while being approximate, it offers a very significant computational advantage. Ref. [77] suggested that the error associated with this split, while being formally small, can be absorbed into the nuisance parameters.¹⁶ Hence, in order to match the CLASS-PT values of EFT parameters, we have to use the wiggly-smooth decomposition for consistency.

IR resummation of the density field is very similar to that of the velocity divergence. Once we establish that the kernels eq. (A3) do not have IR singularities, it follows straightforwardly that they can only come from vertices of the velocity field. Their resummation yields the same formula as (A11) but with $\{YY\} = \{\delta\delta\}$.

¹⁶ This is confirmed by comparison with numerical simulations such as PT Challenge.

The bias tracers can be described in TSPT in full analogy with the matter density field δ . To that end one rewrites the bias expansion as

$$\delta_g(\mathbf{k}) = \delta_g[\Theta; \eta, \mathbf{k}] \equiv \sum_{n=1}^{\infty} \frac{1}{n!} \int [dq]^n M_n^{(r)}(\mathbf{p}_1, \dots, \mathbf{p}_n) \delta^{(3)}(\mathbf{k} - \mathbf{p}_{1\dots n}) \prod_{j=1}^n \Theta(\eta, \mathbf{p}_j), \quad (\text{A13})$$

and finds that the Eulerian bias kernels $M_n^{(r)}$ do not contain IR singularities. This is the consequence of the fact that the bias expansion must satisfy the equivalence principle. As a result of that, only the diagrams that contain the vertices $\bar{\Gamma}_n$ have to be resummed. This produces the same result as (A11) but with $\{YY\} = \{gg\}$.

The formal generating functional for correlators of the shifted fields is given by

$$Z[J_{\bar{1}}, J_{\Delta\delta_g}; \eta] = \int [\mathcal{D}\Theta] \mathcal{P}[\Theta; \eta] \exp \left\{ J_{\bar{1}} \tilde{\delta}_1 + J_{\Delta\delta_g} \Delta\delta_g \right\}. \quad (\text{A14})$$

From the above discussion it is clear that in order to show that the algorithm (A11) applies to the shifted operator field, it is sufficient to demonstrate that the kernels that appear in an analog of eq. (A13) for shifted operators are IR safe. Plugging the ansatz

$$\tilde{\delta}_1(\mathbf{k}) = \tilde{\delta}_1[\Theta; \eta, \mathbf{k}] \equiv \sum_{n=1}^{\infty} \frac{1}{n!} \int [dq]^n L_n^{(r)}(\mathbf{p}_1, \dots, \mathbf{p}_n) \delta^{(3)}(\mathbf{k} - \mathbf{p}_{1\dots n}) \prod_{j=1}^n \Theta(\eta, \mathbf{p}_j), \quad (\text{A15})$$

we find a sequence of IR safe expressions

$$L_1^{(r)} = \tilde{K}_1 = 1, \quad L_2^{(r)} = 2 \left(\tilde{K}_2 - G_2 \right) = \frac{8}{7} \left(1 - \frac{(\mathbf{k}_1 \cdot \mathbf{k}_2)^2}{k_1^2 k_2^2} \right), \quad (\text{A16})$$

etc., where \tilde{K}_2 are Eulerian kernels for $\tilde{\delta}_1$ and G_2 is the velocity divergence kernel in standard perturbation theory [111].

As for the $\Delta\delta_g = \delta_g - b_1 \tilde{\delta}_1$ field, it is a difference of two terms whose series expansions (A15) and (A13) are IR safe, and hence TSPT $\Delta\delta_g$ kernels $\Delta M_n^{(r)}$ are IR safe as well. This implies that eq. (A11) describes the end result of IR resummation for both $\langle \tilde{\delta}_1 \tilde{\delta}_1 \rangle$ and $\langle \Delta\delta_g \tilde{\delta}_1 \rangle$ correlators that appear in the transfer function calculations.

Let us discuss now redshift space distortions in TSPT. The key idea is to consider the redshift space coordinate mapping ($v_z = \hat{z} \cdot \mathbf{v}$, with v being the matter velocity field \mathbf{v}),

$$\mathbf{s} = \mathbf{x} + \hat{z}v_z/(aH), \quad (\text{A17})$$

as a flow in a second time \mathcal{T} that ranges from 0 to $1/(aH)$,

$$\mathbf{s} = \mathbf{x} + \hat{z}v_z\mathcal{T}. \quad (\text{A18})$$

The initial conditions in this fictitious flow correspond to real space fields. The fields at $\mathcal{T} = 1/(aH)$ are redshift space fields $\Theta^{(s)}$ and $\delta^{(s)}$. The flow then satisfies the usual free hydrodynamical equations,

$$\begin{aligned} \partial_{\mathcal{F}}\delta_{\mathbf{k}}^{(s)} - \frac{k_z^2}{k^2}\Theta_{\mathbf{k}}^{(s)} &= \int [dp]^2 \delta^{(3)}(\mathbf{k} - \mathbf{p}_{12}) \alpha^{(s)}(\mathbf{p}_1, \mathbf{p}_2) \Theta_{\mathbf{p}_1}^{(s)} \delta_{\mathbf{p}_2}^{(s)}, \\ \partial_{\mathcal{F}}\Theta_{\mathbf{k}}^{(s)} &= \int [dq]^2 \delta^{(3)}(\mathbf{k} - \mathbf{p}_{12}) \beta^{(s)}(\mathbf{p}_1, \mathbf{p}_2) \Theta_{\mathbf{p}_1}^{(s)} \Theta_{\mathbf{p}_2}^{(s)}, \end{aligned} \quad (\text{A19})$$

where $\mathcal{F} = f\mathcal{T}aH$ and

$$\begin{aligned} \alpha^{(s)}(\mathbf{p}_1, \mathbf{p}_2) &\equiv \frac{p_{1,z}(p_{1,z} + p_{2,z})}{p_1^2}, \\ \beta^{(s)}(\mathbf{p}_1, \mathbf{p}_2) &\equiv \frac{(\mathbf{p}_1 + \mathbf{p}_2)^2 p_{1z} p_{2z}}{2p_1^2 p_2^2}. \end{aligned} \quad (\text{A20})$$

The above flow induces the transformation of the TSPT generating function similar to the transformation produced by the usual cosmological evolution. The new (redshift space) generating functional will now have vertices

$$\begin{aligned} &\partial_{\mathcal{F}}\Gamma_n^{(s)tot}(\mathcal{F}; \mathbf{k}_1, \dots, \mathbf{k}_n) \\ &+ \sum_{m=1}^n \frac{1}{(n-m)!m!} \sum_{\sigma} I_m^{(s)}(\mathbf{k}_{\sigma(1)}, \dots, \mathbf{k}_{\sigma(m)}) \\ &\Gamma_{n-m+1}^{(s)tot}\left(\mathcal{F}; \sum_{l=1}^m \mathbf{k}_{\sigma(l)}, \mathbf{k}_{\sigma(m+1)}, \dots, \mathbf{k}_{\sigma(n)}\right) \\ &= \delta^{(3)}\left(\sum_{i=1}^n \mathbf{k}_i\right) \int [dp] I_{n+1}^{(s)}(\mathcal{F}; \mathbf{p}, \mathbf{k}_1, \dots, \mathbf{k}_n), \end{aligned} \quad (\text{A21})$$

where the r.h.s. stems from the fictitious Eulerian dynamics equation (A19) for the redshift space velocity divergence $\Theta^{(s)}$:

$$\begin{aligned} \partial_{\mathcal{F}}\Theta_{\mathbf{k}}^{(s)} &= \\ &\sum_{n=1}^{\infty} \frac{1}{n!} \int [dp]^n \delta^{(3)}(\mathbf{k} - \mathbf{p}_{1\dots n}) I_n^{(s)}(\mathbf{p}_1, \dots, \mathbf{p}_n) \Theta_{\mathbf{p}_1}^{(s)} \dots \Theta_{\mathbf{p}_n}^{(s)}. \end{aligned} \quad (\text{A22})$$

This new fictitious dynamics generates new IR divergences, which can be traced back to the fact that the redshift-space mapping depends on the velocity w.r.t. the observer's frame, which violates the equivalence principle. This introduces additional IR singularities in vertices $\Gamma_n^{(s)}$ that are defined just like in eq. (A9). The redshift space density kernels $\mathcal{M}_n^{(s)}$ are IR safe. The IR enhancements from the vertices can be IR resummed in the diagrammatic expansion, yielding the result

$$\begin{aligned} P_{YY}^{1-\text{loop,IR}}(k) &= P_{YY}^{\text{tree}}[e^{-\hat{\mathcal{S}}^{(s)}}(1 + \mathcal{S}^{(s)})P_{11}] \\ &+ P_{YY}^{1-\text{loop}}[e^{-\hat{\mathcal{S}}^{(s)}}P_{11}], \end{aligned} \quad (\text{A23})$$

where $\{YY\} = \{\Theta\Theta\}$, and the operator $\hat{\mathcal{S}}^{(s)}$ is given by

$$\begin{aligned} \hat{\mathcal{S}}^{(s)}P_{11} &= P^{ab}P^{cd}k^a k^c \times \\ &\int_{p \leq \Lambda_{\text{IR}}} [dp] P_{11}(p) \frac{p^b p^d}{p^4} (1 - \cosh(\mathbf{p}\nabla_{k'})) P_{11}(k') \Big|_{k'=k}, \end{aligned} \quad (\text{A24})$$

where $P_{ab} = \delta_{ab} + f\hat{z}_a\hat{z}_b$. As before, if we use the wiggly-smooth split, it produces a simple expression, which can be further simplified using method of [80], leading to the damping factor (44).

IR resummation of the matter and galaxy density fields in redshift space takes the same form as eq. (A23) by virtue of the fact that their redshift space TSPT kernels are IR safe.

As far as the shifted operators are concerned, it is convenient to treat our forward model as a redshift space mapping of a particular Eulerian biased tracer in real space. The bias expansion for this tracer depends on the line-of-sight just like in the case of selection effects [148] or the Lyman alpha forest [149, 150]. Then it is easy to show that the TSPT kernels of the shifted operators $L_n^{(s)}$ and $\Delta M_n^{(r)}$ are IR safe since the shifted fields do not break the equivalence principle. This leads to eq. (43) for their correlators, analogous to the galaxy density field in redshift space.

Alternatively, instead of doing the redshift space mapping with the full velocity field (A17), one can consider a mapping with the Zel'dovich velocity, as we do in our redshift space forward model. This can be interpreted as a fictitious flow

$$\mathbf{s} = \mathbf{x} + \hat{z}v_z^{\text{ZA}}\mathcal{T}, \quad (\text{A25})$$

where v^{ZA} is the velocity in the Zel'dovich approximation. The TSPT equations for this fictitious Zel'dovich

flow will be the same as (A19). This implies that our Zel’dovich flow will automatically capture IR singularities in the fictitious evolution. This is not surprising as the IR enhancements precisely appear from the Zel’dovich displacements. Then one can compute the flow of the kernels of the shifted operators $L_n^{(s)}$ and $\Delta M_n^{(r)}$, find that they are IR safe, and carry out the IR resummation in the usual way.

Appendix B: On the accuracy of the perturbative description for the galaxy density field in redshift space

This section pursues two main goals. On the practical side, we would like to determine k_{\max} for our fits of P_{err} in redshift space, which should yield the stochastic counterterms $\alpha_{0,1,2}$. From the conceptual side, we would like to understand what is the reach of the perturbative field for galaxies and redshift space, and whether there is any sign of the breakdown of EFT for galaxies on large scales, similar to the reports of the flattening of the stochastic power spectrum for the dark matter density field in ref. [151].

To answer these questions, we used HOD mocks produced for the large **Abacus** boxes, which helps us reduce the residual statistical scatter in our field-level calculations. For concreteness, we focus on one particular HOD model similar to that of the BOSS CMASS sample. The results are similar for other HOD models from our sample.

The noise power spectrum is shown in fig. 13. As expected in theory, it is given by the white noise constant power on very large scales. On quasilinear scales the noise depends both on the wavevector norm k and its cosine with the line-of-sight μ . Its power spectrum has the theoretically expected scaling $k^2\mu^2$ up to $k \approx 0.2 \text{ hMpc}^{-1}$, see the right panel of fig. 13. For $k > 0.2 \text{ hMpc}^{-1}$ the noise becomes more shallow, suggesting that higher order corrections may become important. This is the first piece of evidence that the choice of $k_{\max} = 0.2 \text{ hMpc}^{-1}$ is an adequate one.

At a second step, we study the dependence of our α_2 measurements on k_{\max} . We find that α_2 exhibits significant scale dependence, see the left panel of fig. 14. On large scales the main source of the scale dependence is the statistical scatter, while on small scales it is pro-

duced by higher order EFT corrections. To understand better where the scale dependence due to the higher order corrections actually starts, we consider the redshift-space part of the noise:

$$P_{\text{err}} - \frac{1}{\bar{n}} \left(\alpha_0 + \alpha_1 \frac{k^2}{[0.45 \text{ hMpc}^{-1}]^2} \right) = P_{\text{err}}^{\text{FoG}}(k, \mu), \quad (\text{B1})$$

and calculate numerically the slope $n_{\alpha_2}^{\text{eff}}$ of this spectrum in k space,

$$n_{\alpha_2}^{\text{eff}} \equiv \frac{d \ln P_{\text{err}}^{\text{FoG}}(k, \mu)}{d \ln k}. \quad (\text{B2})$$

The numerical slope from the data is displayed in the right panel of fig. 14. The $n_{\alpha_2}^{\text{eff}}(k_{\max})$ curve becomes much smoother if we consider cumulative static averages of $n_{\alpha_2}^{\text{eff}}$ up to k_{\max} , shown as the “mean of data.” We see that the mean of $n_{\alpha_2}^{\text{eff}}$ crosses the theoretically expected value 2 around $k_{\max} \approx 0.2 \text{ hMpc}^{-1}$. This is the second piece of evidence that confirms our baseline choice.

Finally, fig. 15 shows the residual between P_{err} and the EFT model with the values of α_2 and α_0, α_1 extracted at our baseline scale cuts 0.2 hMpc^{-1} and 0.4 hMpc^{-1} , respectively. First, we see that on large scales the EFT model perfectly predicts the measured noise power spectrum. The residuals between the theory and the data scale as k^4 , which is precisely the prediction for the higher order corrections. We find that the relevant EFT cutoff scales for the noise power spectrum are $k_S \approx 0.45 \text{ hMpc}^{-1}$ in redshift space and $k_R \approx 1.45 \text{ hMpc}^{-1}$ in real space.

Fig. 15 shows that the noise power spectrum can be well described by the EFT derivative expansion even for wavenumbers larger than 0.2 hMpc^{-1} (0.4 hMpc^{-1}) in redshift (real) space provided that the appropriate higher order corrections are taken into account. Thus, unlike the dark matter case [151], we do not see evidence for the shallower shape of the noise power spectrum on the quasi-linear scales in the case of galaxies.

We point out, however, that around the EFT cutoff, $k \approx 0.4 \text{ hMpc}^{-1}$, the derivative expansion for the noise power spectrum breaks down. Modeling the non-trivial scale-dependence of the stochastic noise at this scale may pose a serious challenge to the phenomenological “hybrid EFT” approaches e.g. [59].

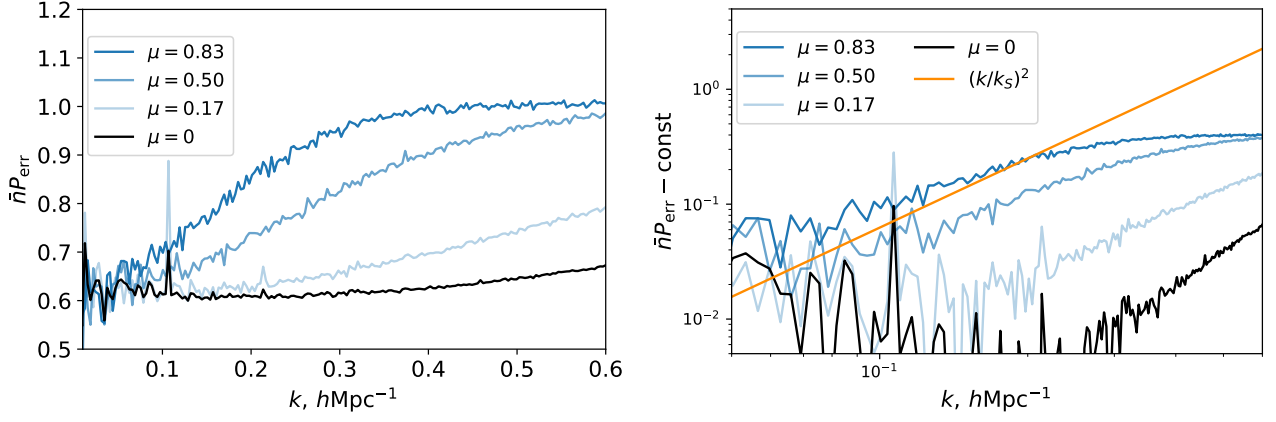


FIG. 13. The noise power spectrum in redshift space (left panel), and its behavior after subtracting the constant white noise contribution (right panel).

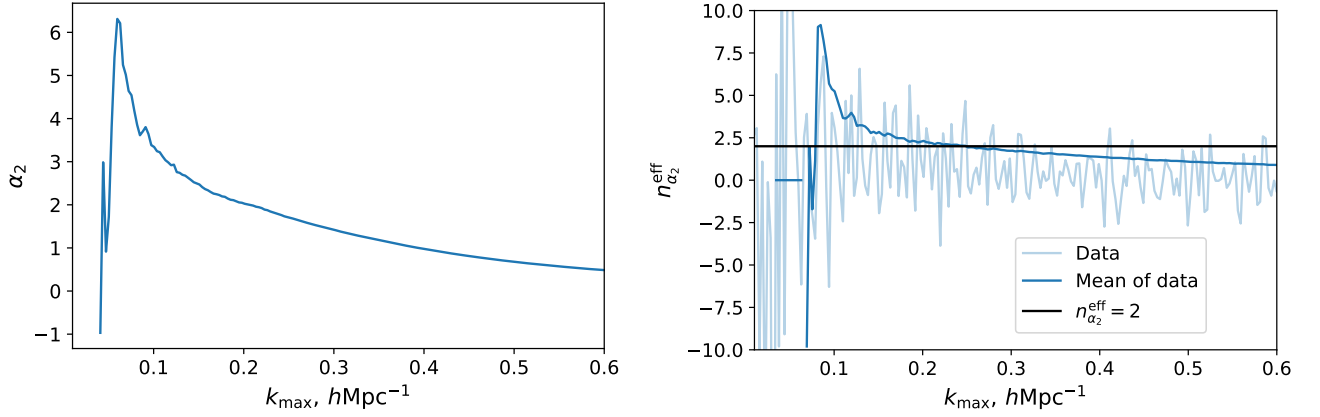


FIG. 14. Left panel: the fit of α_2 from the error power spectrum as a function of k_{max} . Right panel: the effective slope of the redshift space part of the noise power spectrum $n_{\alpha_2}^{\text{eff}}$ as a function of k_{max} measured from the data, along with the cumulative mean up to k_{max} , and the EFT prediction $n_{\alpha_2}^{\text{eff}} = 2$.

Appendix C: Analytic proof of the approximate cosmology-independence of the HOD priors

Let us present an analytic proof that the cosmology-dependence of the HOD-based priors can be absorbed into the HOD parameters. Our proof will rely on four key assumptions:

1. the HMF is universal (i.e. depends only on the peak height ν),
2. the EFT parameters of halos depends only the peak height,
3. the standard real-space HOD parametrization (73)
4. power-law cosmology with $P_{11} \propto k^n$.

First, let us derive the relationship between the EFT parameters of halos and HOD galaxies. We start by writing down the perturbed number density of halos as

$$n_h(\mathbf{x}) = \frac{d\bar{n}_h}{d \ln M} (1 + \delta_h(\mathbf{x})), \quad (\text{C1})$$

where $\frac{d\bar{n}_h}{dM}$ is the halo mass function. Given an average HOD $\langle N_g \rangle$, we can obtain a similar expression for galaxies

$$n_g(\mathbf{x}) = \int dM \frac{d\bar{n}_h}{dM} \langle N_g \rangle_M (1 + \delta_h(\mathbf{x})), \quad (\text{C2})$$

with $\bar{n}_g = \int dM \frac{d\bar{n}_h}{dM} \langle N_g \rangle_M$, from which it immediately follows that

$$\delta_g = \frac{n_g(\mathbf{x})}{\bar{n}_g} - 1 = \frac{1}{\bar{n}_g} \int dM \frac{d\bar{n}_h}{dM} \langle N_g \rangle_M \delta_h(\mathbf{x}), \quad (\text{C3})$$

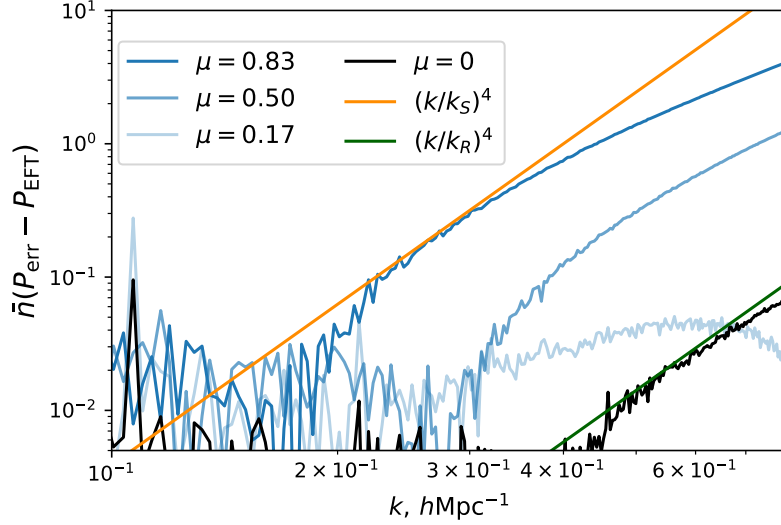


FIG. 15. The residuals between the noise power spectrum of the BOSS-like HOD simulation and the next-to-leading order EFT model from eq. (36). Straight lines show the predicted slopes of the residuals for the next-to-next-to leading EFT corrections.

implying

$$b_{\mathcal{O}}^g = \frac{1}{\bar{n}_g} \int dM \frac{d\bar{n}_h}{dM} \langle N_g \rangle b_{\mathcal{O}}^h(M). \quad (\text{C4})$$

Following the analytic halo models, let us assume that the HMF depends only on the peak height $\nu = \frac{\delta_c}{\sigma_M(z)}$. This relation defines the map between M and ν . Changing the variables in the mass integral (C4) we obtain

$$b_{\mathcal{O}_a}^g = \frac{1}{\bar{n}_g} \int d\nu \frac{d\bar{n}_h}{d\nu}(\nu) \langle N_g \rangle_{M(\nu)} b_{\mathcal{O}_a}^h(\nu), \quad (\text{C5})$$

where we took into account that the halo bias parameters depend on M via ν , see eq. (70). Note that $\bar{\rho}$ in the HMF is canceled by the denominator \bar{n}_g .

It is easy to show now that for the standard HOD, the expression above is approximately cosmology-independent. To that end, let us assume a power-law universe,

$$P_{11}(k) = \frac{2\pi^2}{k_{\text{NL}}^3} \frac{k^n}{k_{\text{NL}}^n}. \quad (\text{C6})$$

The amplitude of the linear matter power spectrum scales with redshift as $P_{11} \propto D_+^2(z)$, implying

$$k_{\text{NL}} = k_{\text{NL}}(z=0) D_+^{-\frac{2}{3+n}}(z). \quad (\text{C7})$$

The filtered mass variance in this cosmology is given by

$$\begin{aligned} \sigma_M^2(z) &= \frac{9 \cdot 2^{-n} (1+n) \Gamma(n-1)}{n-3} \frac{\sin\left(\frac{\pi n}{2}\right)}{(k_{\text{NL}} R)^{n+3}}, \\ &= \left(\tilde{M}_{\text{NL}}/M\right)^{\frac{n+3}{3}}, \end{aligned} \quad (\text{C8})$$

where the cosmology dependence is captured by

$$\tilde{M}_{\text{NL}} \equiv \left(\frac{9 \cdot 2^{-n} (1+n) \Gamma(n-1) \sin\left(\frac{\pi n}{2}\right)}{n-3} \right)^{\frac{3}{n+3}} \frac{4\pi \Omega_m \rho_c}{3k_{\text{NL}}^3}, \quad (\text{C9})$$

and we used $4\pi R^3 \rho_c \Omega_m / 3 = M$. The peak height is given by

$$\nu = \delta_c \left(\frac{M}{\tilde{M}_{\text{NL}}} \right)^{\frac{n+3}{6}} \equiv \left(\frac{M}{M_{\text{NL}}} \right)^{\frac{n+3}{6}}, \quad M = M_{\text{NL}} \nu^{\frac{6}{n+3}}. \quad (\text{C10})$$

We can use the above formulas to change the variables from M to ν in the integral (C5), so that the galaxy bias parameters become universal. Using the standard HOD parametrization (73), we obtain the following re-mapping for the centrals:

$$\begin{aligned} \langle N_c \rangle &= \frac{1}{2} \left[1 + \text{Erf} \left(\frac{\ln(M/M_{\text{cut}})}{\ln 10 \sqrt{2} \sigma} \right) \right] \\ &= \frac{1}{2} \left[1 + \text{Erf} \left(\frac{\ln(\nu/\nu_{\text{cut}})}{\ln 10 \sqrt{2} \sigma'} \right) \right], \end{aligned} \quad (\text{C11})$$

where we defined

$$\begin{aligned} \nu_{\text{cut}} &\equiv \frac{\delta_c}{\sigma_{M_{\text{cut}}}} = \left(\frac{M_{\text{cut}}}{M_{\text{NL}}} \right)^{\frac{3+n}{6}}, \\ \sigma' &= \frac{6}{n+3} \sigma. \end{aligned} \quad (\text{C12})$$

This shows that the bias parameters of the centrals are universal: they depend on cosmology and redshift only

via combinations σ' and ν_{cut} , and hence a change in cosmology can be fully compensated by an adjustment of the HOD parameters. In this sense the cosmology-dependence is degenerate with the HOD parameters. In particular, since $M_{\text{NL}} \propto \sigma_8^{\frac{6}{n+3}}$, the change in σ_8 is equivalent to a rescaling of ν_{cut} as

$$\nu_{\text{cut}} \rightarrow \nu'_{\text{cut}} = \nu_{\text{cut}} \frac{\sigma_8}{\sigma'_8}. \quad (\text{C13})$$

In fact, the rescaling above removes the $\sigma_8(z)$ dependence *exactly* even in a Λ CDM cosmology, as it simply follows from the definition of the peak height parameter.

As for the satellites, using the mapping (C10) we find

$$\langle N_s \rangle = \langle N_c \rangle \left(\frac{\nu^{\frac{6}{n+3}} - \kappa \nu_{\text{cut}}^{\frac{6}{n+3}}}{M_1/M_{\text{NL}}} \right)^\alpha. \quad (\text{C14})$$

The first relevant observation is that one can completely absorb the dependence on M_{NL} , which captures the sensitivity to the mass fluctuation amplitude $\sigma_8(z)$ at the redshift of interest,

$$M'_1 = M_1/M_{\text{NL}}, \quad (\text{C15})$$

while the rest of it is absorbed into ν_{cut} through (C13). Thus, we have shown that the dependence on the amplitude $\sigma_8(z)$ can be absorbed into the HOD parameters *exactly*.

In general, however, it is impossible to fully absorb the dependence of the satellite HOD on the power spectrum slope n by M_1 , α , and κ . One way out is to introduce an additional HOD parameter β in (C14),

$$\frac{6}{n+3} \rightarrow \beta, \quad (\text{C16})$$

However, let us recall that for the satellites the physically interesting regime is $M \gg \kappa M_{\text{cut}}$. In this case the cosmology dependence can be absorbed into M_1 and α completely,

$$\langle N_s \rangle \approx \langle N_c \rangle \left(\frac{\nu^{\frac{6\alpha}{n+3}}}{(M_1/M_{\text{NL}})^\alpha} \right) \equiv \frac{\nu^{\alpha'}}{\nu_1^{\alpha'}}. \quad (\text{C17})$$

Let us note that our discussion suggests that the breaking of the cosmology universality seems to be an artifact of the usual HOD parametrization. From the approximate universality of the HMF, it is more natural to *define* the HOD models in terms of the peak height, in which case the cosmology-independence will be manifest. Therefore, the residual cosmology dependence of

the EFT parameters of the HOD galaxies may simply be an unphysical artifact of the standard phenomenological parametrization.

Let us estimate now a typical shift of the HOD parameters needed to absorb the cosmology dependence. Let us fix M_{cut} and consider two cosmologies with different σ_8 . Let us compute now how much do we need to shift M_{cut} to compensate for the change in σ_8 . We have

$$M_{\text{cut}} = M_{\text{NL}} \nu_{\text{cut}}^{\frac{6}{n+3}} \quad (\text{C18})$$

Now we want to find $\nu'_{\text{cut}}^{\frac{6}{n'+3}}$ that gives the same $b_{\mathcal{O}_a}^g$. For that we need to have the same HOD as a function of ν in both cosmologies. For the centrals we have

$$\frac{n'+3}{6} \ln(\nu/\nu'_{\text{cut}}) = \frac{n+3}{6} \ln(\nu/\nu_{\text{cut}}), \quad (\text{C19})$$

i.e. $\nu_{\text{cut}} = \nu'_{\text{cut}}$ since we assume that the effective tilt does not change, $n' = n$. We get

$$M'_{\text{cut}} = \frac{M'_{\text{NL}}}{M_{\text{NL}}} M_{\text{cut}} = \left(\frac{\sigma'_8}{\sigma_8} \right)^{\frac{6}{n+3}} M_{\text{cut}}. \quad (\text{C20})$$

Since we are sampling $\log M_{\text{cut}}$, we find

$$\log M'_{\text{cut}} - \log M_{\text{cut}} = \frac{6}{n+3} \log \left(\frac{\sigma'_8}{\sigma_8} \right). \quad (\text{C21})$$

For $\sigma'_8 = 0.7$, $\sigma_8 = 0.8$, and $n = -2$ we get

$$\log M'_{\text{cut}} - \log M_{\text{cut}} = -0.34, \quad (\text{C22})$$

which is a very moderate shift that is much smaller than the width of our prior on $\log M_{\text{cut}}$.

Appendix D: Additional test of cosmology independence of HOD priors

In this section we study how much the HOD-based EFT parameters change under the variation of the underlying cosmology. To that end we select three cosmological models from the large **Abacus** boxes: the fiducial one, the one with a higher $\sigma_8 = 0.86$, and the one with a lower $\sigma_8 = 0.75$. The fiducial large box has the same cosmology as our baseline **Abacus** mocks, and hence it will serve us as a control sample. We chose the boxes with very different σ_8 because it is very closely related to σ_M , which dominates the response of EFT parameters to cosmology.

As a next step, we make 10 samples of HOD parameters from our priors and produce 10 galaxy catalogs for

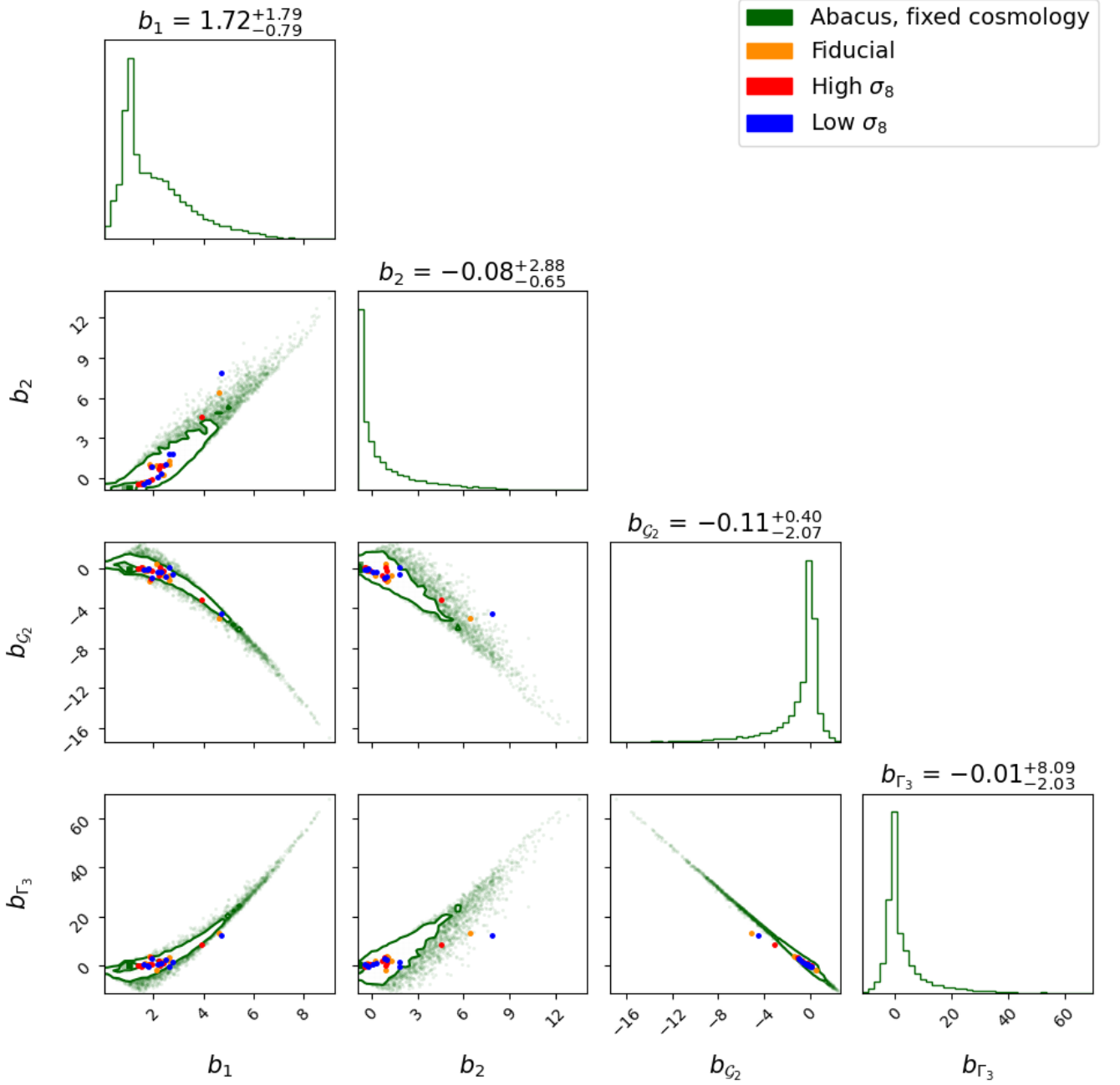


FIG. 16. The baseline distribution of EFT parameters for a fixed cosmology (our baseline distribution), along with a sample of 10 HOD models from three large **Abacus** boxes: the fiducial one (`cosm000`), which we use as a control sample, the one with low $\sigma_8 = 0.75$ (`cosm004`), and the one with high $\sigma_8 = 0.86$ (`cosm003`). The HOD parameters are the same for each cosmology.

each cosmology. Then we measure the corresponding EFT parameters. Our results for the bias parameters b_1, b_2, b_{G_2} and b_{Γ_3} shown in fig. 16. The picture is similar for other parameters.

First, we see that all samples lie within the baseline distribution spanned by variations of HOD parameters

at a fixed cosmology. Second, we see that for a fixed HOD model, the variation of cosmology has a relative small effect. In particular, the typical spread of EFT parameters due to cosmology variation is smaller than the spread due to the HOD variation. Also note that our test confirms the basic intuition gained in our study of

dark matter halos: lowering/raising σ_8 for a fixed HOD is equivalent to raising/lowering the host halo mass parameters, respectively.

We have one outlier HOD model in each cosmology sample, with $b_1 \approx 4$. We see that the spread is somewhat larger for this parameter, although the low and high σ_8 points are still quite close to the fiducial one. This suggests that the variation of cosmology might be important at the tails of the distribution. However, the corresponding values of the EFT parameters, e.g. $b_1 \simeq 5$, $b_2 \simeq 9$, are far away from the ones we probe with BOSS, $b \simeq 2.5$, $b_2 \simeq 2$, which suggests that this should not have a significant effect on our main results.

All in all, we conclude that the variation of cosmology is a weaker effect than the variation of HOD for the purposes of the prior generation.

Appendix E: Additional plots and tests

Fig. 17, 18 display the EFT parameters of dark matter halos from: (a) FoF and (b) Rockstar catalogs of the Quijote LH simulations, (c) FoF catalogs of the fiducial Quijote simulation and (d) CompaSO catalogs the fiducial Abacus simulation. Note that the distribution of the galaxy bias parameters is very similar across all the halo finders. However, CompaSO and Rockstar produce slightly more consistent results for α_1 and c_2 .

In fig. 19 we display field-level transfer functions and the noise power spectra for an HOD sample with extreme values of EFT parameters. This sample has $\log_{10} M_{\text{cut}} \approx 14$ and $\log_{10} M_1 \approx 13$ ($\kappa \approx 0.5$) and $\alpha_s \approx 2$ at the edges of the priors of the HOD parameters that we sample. Physically, this sample has very few centrals, but a gigantic number of satellites, resulting in the satellite fraction $\approx 93\%$. The number density of the satellites in this sample is a factor of $\mathcal{O}(10)$ greater than the number density of the centrals. Thus, we have a highly biased tracer with low number density. Since the number density of satellites is an order of magnitude greater than the number density of centrals, we obtain $P_{\text{err}} \sim \frac{1}{\bar{n}_c} \sim \mathcal{O}(10) \frac{1}{\bar{n}_g}$ from the arguments of [126] and in full agreement with the measurements. We point out, however, that the real space transfer functions are smooth up to $k_{\text{max}} \approx 0.5 \text{ hMpc}^{-1}$, so this sample does not require any modification of the fitting procedure in real space.

In addition, the sample also features a very large satellite velocity bias. Together with an extremely large satellite fraction this generates a very strong fingers-of-God suppression, which can be seen both in the transfer function of $\beta_1(k, \mu)$ and the error power spectrum P_{err} in redshift space. In particular, we see that the fingers-of-God for this sample lead to $\sim 100\%$ corrections already $k \sim 0.2 \text{ hMpc}^{-1}$, and thus become non-perturbative around our fiducial k_{max} . To obtain more robust results, in principle, one should use $k_{\text{max}} = 0.1 \text{ hMpc}^{-1}$ for this sample. However, such extreme catalogs constitute only 0.3% of our HOD sample, and hence modify only the very tail of the distribution, which we do not expect to model well with the normalizing flows anyway.

All in all, while the EFT parameters of this sample appear quite extreme, it has a physically sound behavior. While this sample does not appear to match any observationally relevant galaxy population, it represents a physically plausible scenario.

Appendix F: The origin of low σ_8 preference in the BOSS analysis

In this appendix we investigate the origin of the preference for low σ_8 in our SBP analysis and also get insights into the extra information brought by the SBP.

As a first step, we locate the k range of data that drives the constraints. To this end we re-analyze the baseline BOSS power spectrum dataset P_ℓ restricted to modes $k < 0.1 \text{ hMpc}^{-1}$. We carry out both the conservative and HOD-informed analyses. The 1D marginalized constraints from these analyses are presented in table IV (only the linear and quadratic bias parameters are shown), while the corner plot for cosmological parameters is displayed in fig. 20.

We see that the results are highly consistent: the posteriors of H_0 and σ_8 largely overlap and have comparable widths. The $\omega_{\text{cdm}}(\Omega_m)$ constraint is visibly worse in the conservative case. This is expected given that this parameter is measured from the shape of the matter power spectrum monopole at the high k end of the allowed data range [95, 98, 152]. The shape information is strongly degenerate with the nuisance parameters for $k < 0.1 \text{ hMpc}^{-1}$ which results in poor constraints in the conservative analysis. This also explains the improvement that we get in the SBP analysis thanks for better

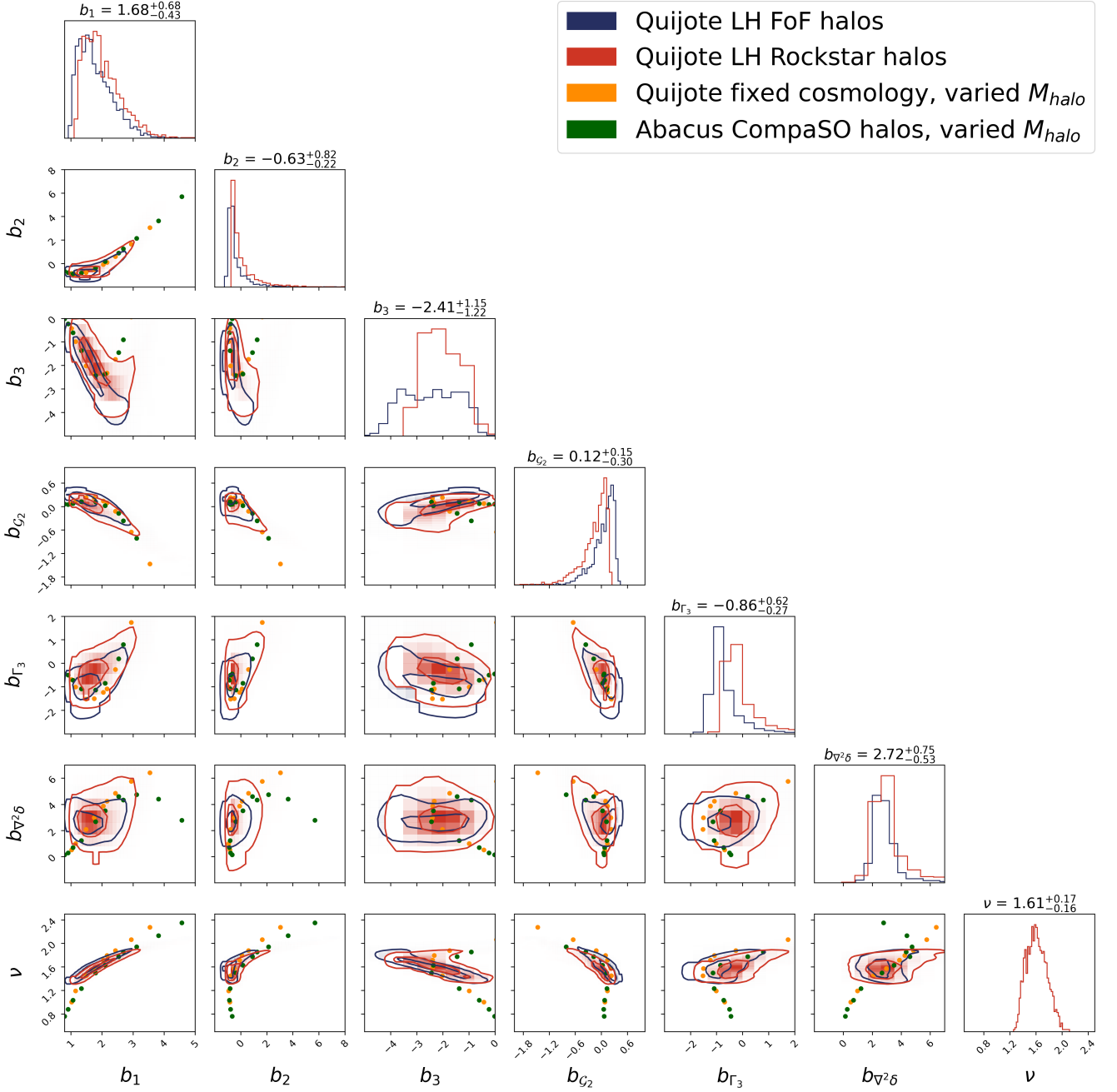


FIG. 17. Same as fig. 6 but with the Rockstar halos from Quijote LH simulations.

priors on nuisance parameters.

An important point here is that in both analyses the σ_8 posteriors are much wider than those of our baseline analysis at $k_{\max} = 0.2 \text{ hMpc}^{-1}$, which implies that our main constraints are driven by the momentum range $0.1 < k/(\text{hMpc}^{-1}) < 0.2$. Fig. 20 also implies that the shift of σ_8 between the conservative analysis and the SBP analysis at $k_{\max} = 0.2 \text{ hMpc}^{-1}$ in fig. 2 stems from the

same large wavenumber end of the data.

To understand further what drives this difference, let us plot take a look at the best-fitting curves from the conservative and SBP analyses. We consider the largest data sample NGCz3, which dominates the final constraints. The best-fit curves, data, and their residuals are presented in fig. 21. For better visibility, we offset the residual points of the SBI analysis along the k

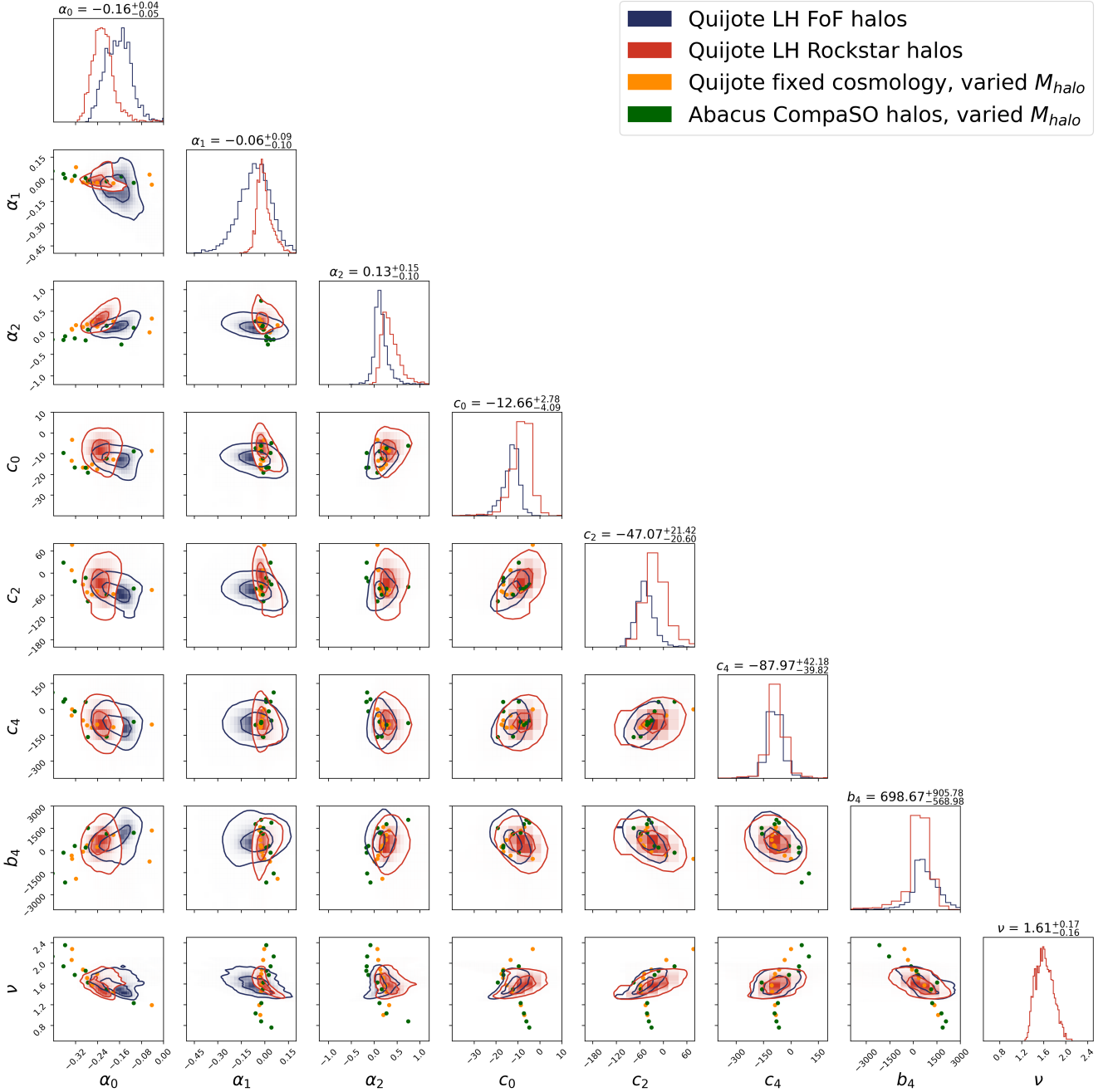


FIG. 18. Same as fig. 17 but for the stochasticity parameters and redshift-space EFT counterterms.

axis. We see that most of the difference between the two best-fits is generated at the level of P_0 data for $0.1 < k/(h\text{Mpc}^{-1}) < 0.2$. This suggests that the main source of information on σ_8 in SBP is not the quadrupole, but actually the monopole. To further verify this, we calculate the χ^2 difference between the SBP and conservative best-fits. We obtain

$$\chi_{\text{like}}^2 \Big|_{\text{SBP}} = 84.96, \quad \chi_{\text{like}}^2 \Big|_{\text{cons}} = 76.97, \quad (\text{F1})$$

where “like” means that we only included the data likelihood in our calculation (i.e. ignored the priors). At face value, the SBP fit is notably worse. This can be visually confirmed by looking at the bottom panel of fig. 21, where we see somewhat larger residuals in the SBP analysis for the monopole around $k \simeq 0.17 h\text{Mpc}^{-1}$. Note that 6.05 out of 8 total units of χ^2 difference stem from the monopole part of the likelihood.

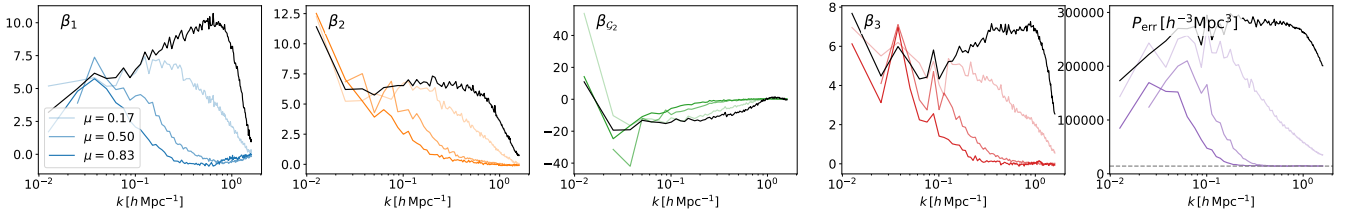


FIG. 19. Same as fig. 3 but for an outlier HOD sample with extreme values of EFT parameters.

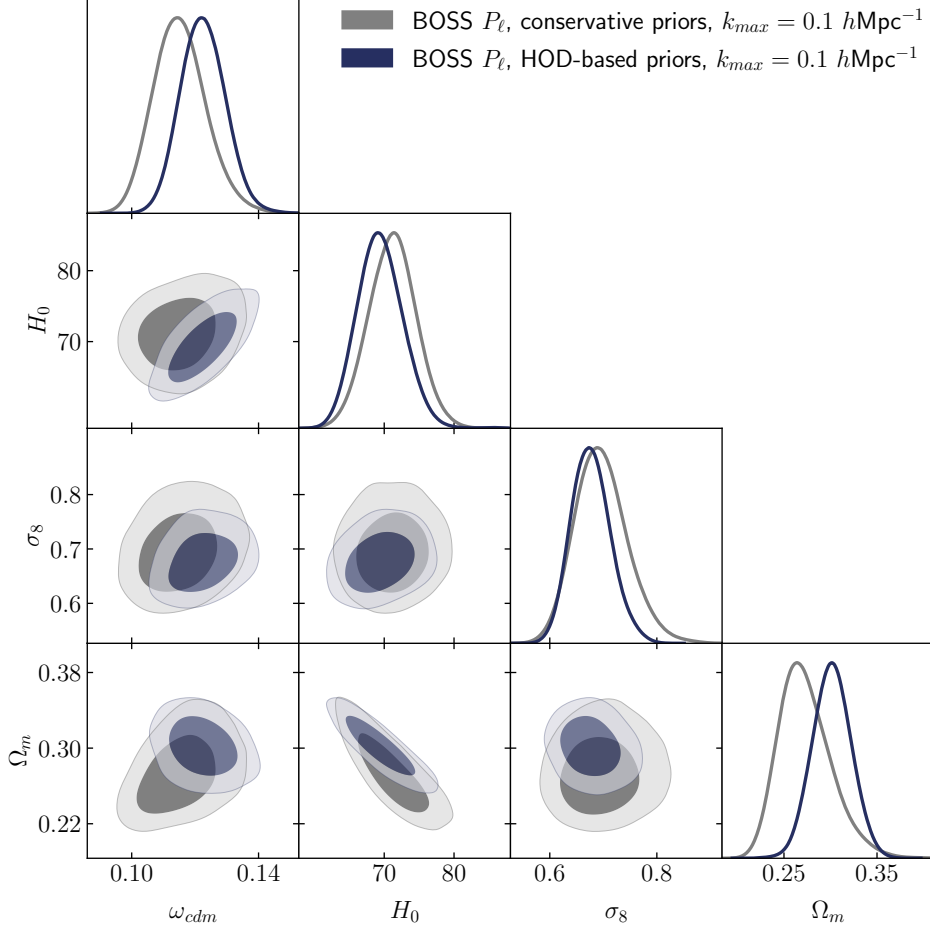


FIG. 20. Cosmological parameters from the EFT-based full shape analysis of the BOSS power spectrum with conservative and informative simulation-based priors on EFT parameters for the data cut $k_{\max} = 0.1 \text{ hMpc}^{-1}$.

To understand the impact of the prior, we display the best-fitting EFT parameters in both analyses on the background of the HOD-based priors in fig. 22. As before, we use the NGCz3 sample in our discussion, noting that the picture is qualitatively the same for other samples of the BOSS data. The first important observation is that the best-fitting value of b_2 from the conservative analysis is incompatible with the HOD models. The second important observation is that the conserva-

tive analysis prefers values of stochastic parameters that correspond to a rather exotic HOD model with $\alpha_0 \sim 0.4$ and $\alpha_2 \sim -2$, which corresponds to HOD samples with a relatively large satellite fraction.

To get a quantitative measure of the role of the priors, let us introduce the effective χ^2 statistic of the prior, $\chi_{\text{eff,prior}}^2 = -2 \ln \mathcal{L}_{\text{EFT}}$, where \mathcal{L}_{EFT} is the likelihood of the EFT parameters from our HOD samples estimated by the normalizing flows. In this case we find that the

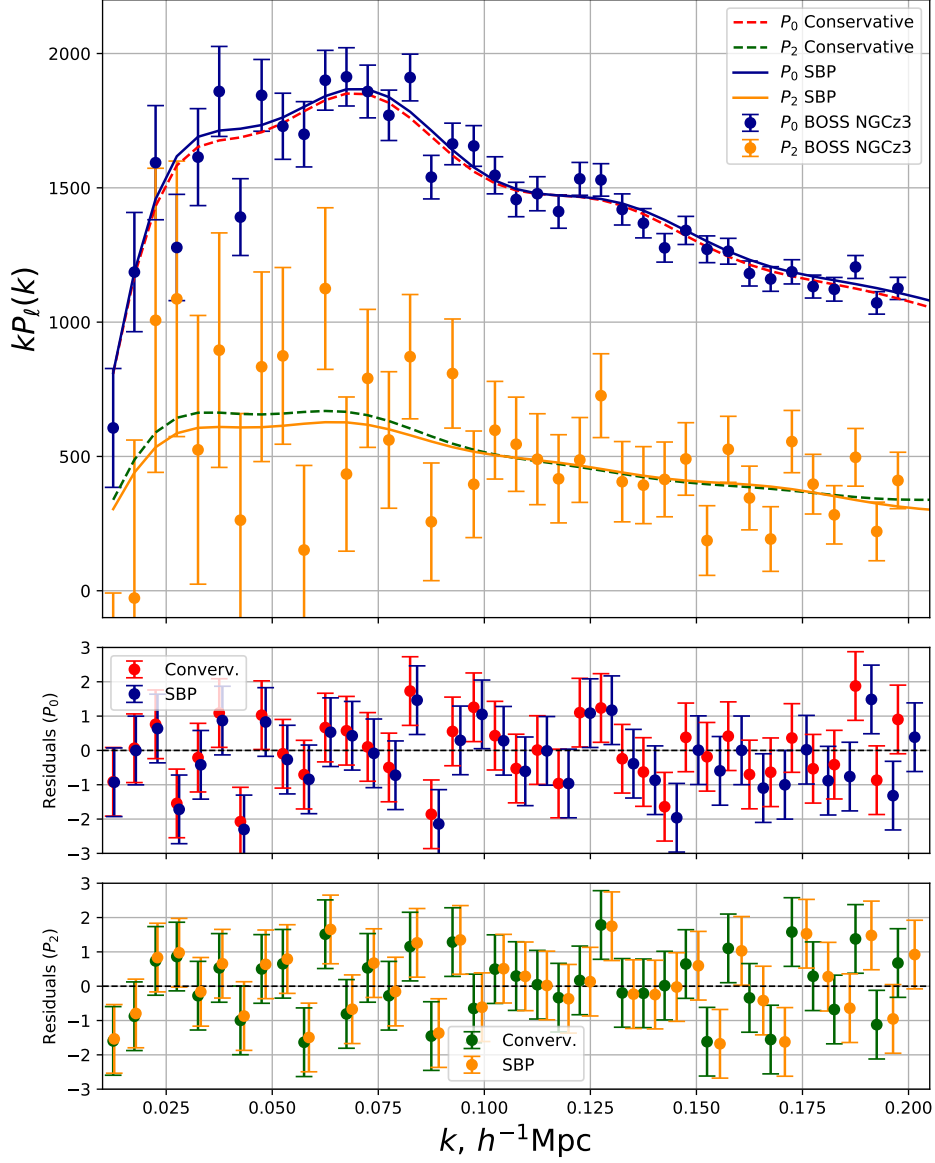


FIG. 21. *Upper panel*: BOSS NGCz3 power spectrum monopole and quadrupole data ($z = 0.61$) along the best-fit models from the analyses with conservative and simulation-based priors. Below are the residuals between the models and the data for the monopole (*central panel*) and the quadrupole (*lower panel*) data.

best-fit EFT parameters needed to fit the BOSS data for a cosmology with $\sigma_8 = 0.74$ have a very low probability as compared to the best-fitting parameters of the SBP analysis. Namely, we find

$$\Delta\chi_{\text{eff, prior}}^2 = \chi_{\text{eff, prior}}^2 \Big|_{\text{SBP}} - \chi_{\text{eff, prior}}^2 \Big|_{\text{cons.}} \approx -391, \quad (\text{F2})$$

which can be roughly interpreted as a $\sim 36\sigma$ tension w.r.t. the best-fit values from the SBP analysis, as follows from the χ^2 distribution for 10 parameters. Most of this difference is generated by the unlikely combina-

tion of $\{b_1, b_2\}$. Indeed, if we keep all other parameter fixed, but replace $\{b_1, b_2\}$ with the SBP best-fit values ($b_1 \simeq 2.6$, $b_2 \simeq 0.6$), we obtain

$$\Delta\chi_{\text{eff, prior}}^2 = \chi_{\text{eff, prior}}^2 \Big|_{\text{SBP}} - \chi_{\text{eff, prior}}^2 \Big|_{\text{cons.} + \{b_1, b_2\}} \approx -101, \quad (\text{F3})$$

i.e. alleviating the tension down to 9σ . The rest of this tension can be attributed to the unlikely combination of remaining real-space parameters (68 units of χ^2 , or $\approx 6\sigma$) and RSD counterterms (33 units of χ^2 , or $\approx 3\sigma$).

It was already pointed out in [12] that fitting the BOSS

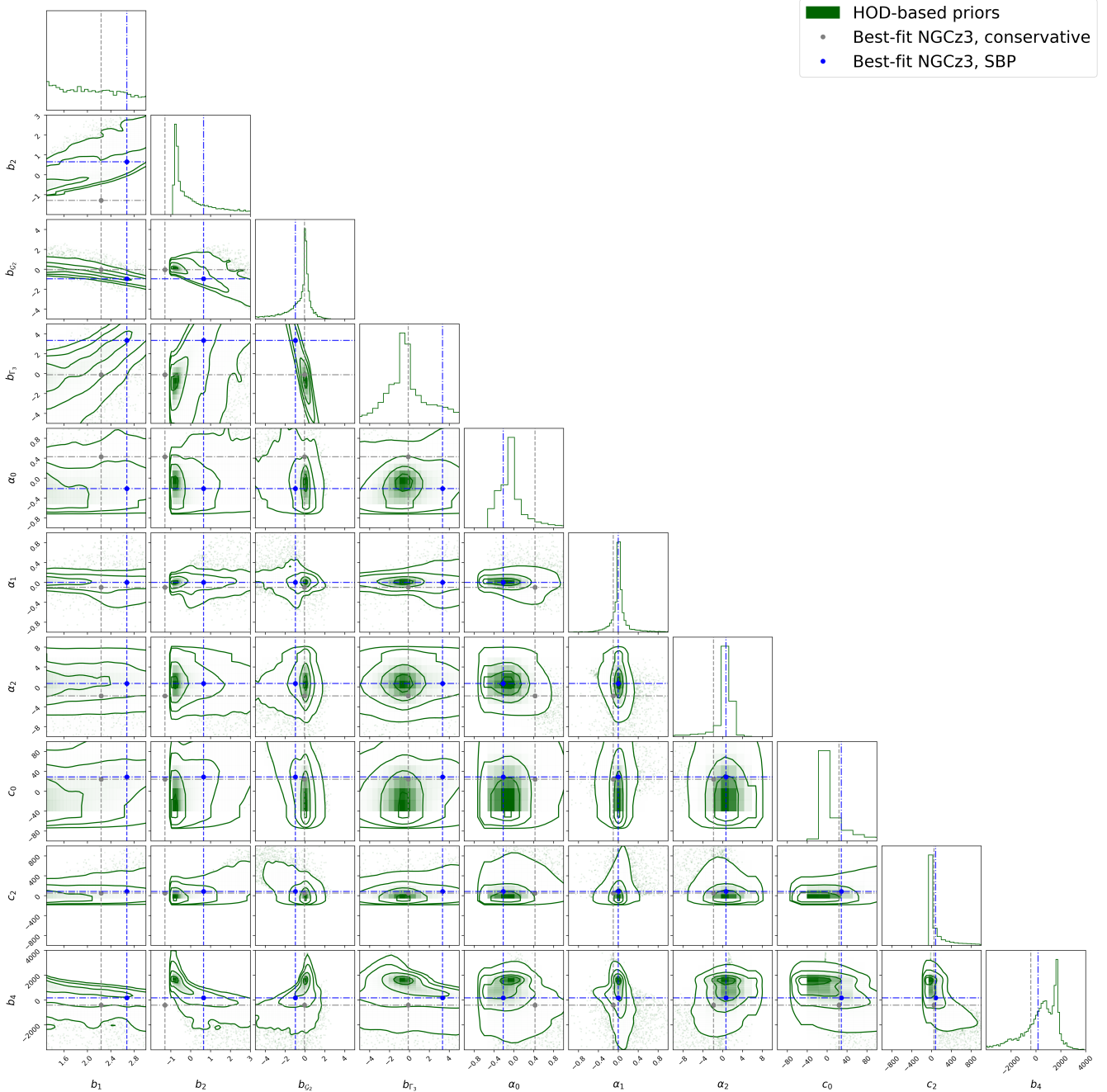


FIG. 22. Best-fit values of EFT parameters from the BOSS NGCz3 sample in the conservative (gray dots) and simulation-based prior analysis (blue dots). The green density on the background depicts the HOD-based priors.

power spectrum data in a cosmology with *Planck*-like σ_8 requires uncommon combinations of EFT parameters that appear in tension with the halo-based predictions. Once the bispectrum data was included in [12], the optimal values of σ_8 went down as the bispectrum of BOSS by itself ruled out the unlikely combination of $\{b_1, b_2\}$ preferred by the power spectrum with the conservative

priors. In our work, we keep seeing the drift towards low σ_8 as we impose stronger restrictions on the EFT parameters. These restrictions come from the field-level EFT priors, which effectively bring in higher order information, e.g. measurements of b_2, b_{G_2} etc. If we treat EFT parameters not a nuisances, but as physical parameters that can be predicted by the HOD models, the most

likely fit to the galaxy power spectrum data is the one with $\sigma_8 \approx 0.66$.

Appendix G: BOSS analysis with free n_s

The results of the MCMC analysis with the free index of scalar primordial fluctuations n_s are shown in fig. 23 and table V.

-
- [1] A. Aghamousa *et al.* (DESI), (2016), [arXiv:1611.00036 \[astro-ph.IM\]](#).
- [2] R. Laureijs *et al.* (EUCLID), (2011), [arXiv:1110.3193 \[astro-ph.CO\]](#).
- [3] v. Ivezić *et al.* (LSST), *Astrophys. J.* **873**, 111 (2019), [arXiv:0805.2366 \[astro-ph\]](#).
- [4] R. Akeson *et al.*, (2019), [arXiv:1902.05569 \[astro-ph.IM\]](#).
- [5] Y. B. Zeldovich, *Astron. Astrophys.* **5**, 84 (1970).
- [6] D. Baumann, A. Nicolis, L. Senatore, and M. Zaldarriaga, *JCAP* **1207**, 051 (2012), [arXiv:1004.2488 \[astro-ph.CO\]](#).
- [7] J. J. M. Carrasco, M. P. Hertzberg, and L. Senatore, *JHEP* **09**, 082 (2012), [arXiv:1206.2926 \[astro-ph.CO\]](#).
- [8] M. M. Ivanov, (2022), [arXiv:2212.08488 \[astro-ph.CO\]](#).
- [9] M. M. Ivanov, M. Simonović, and M. Zaldarriaga, *Phys. Rev. D* **101**, 083504 (2020), [arXiv:1912.08208 \[astro-ph.CO\]](#).
- [10] G. D’Amico, J. Gleyzes, N. Kokron, D. Markovic, L. Senatore, P. Zhang, F. Beutler, and H. Gil-Marín, (2019), [arXiv:1909.05271 \[astro-ph.CO\]](#).
- [11] S.-F. Chen, Z. Vlah, and M. White, *JCAP* **02**, 008 (2022), [arXiv:2110.05530 \[astro-ph.CO\]](#).
- [12] O. H. E. Philcox and M. M. Ivanov, *Phys. Rev. D* **105**, 043517 (2022), [arXiv:2112.04515 \[astro-ph.CO\]](#).
- [13] S.-F. Chen, M. M. Ivanov, O. H. E. Philcox, and L. Wenzl, (2024), [arXiv:2406.13388 \[astro-ph.CO\]](#).
- [14] M. Maus *et al.*, (2024), [arXiv:2404.07312 \[astro-ph.CO\]](#).
- [15] T. Baldauf, L. Mercolli, M. Mirbabayi, and E. Pajer, *JCAP* **1505**, 007 (2015), [arXiv:1406.4135 \[astro-ph.CO\]](#).
- [16] T. Baldauf, L. Mercolli, and M. Zaldarriaga, *Phys. Rev. D* **92**, 123007 (2015), [arXiv:1507.02256 \[astro-ph.CO\]](#).
- [17] T. Konstandin, R. A. Porto, and H. Rubira, *JCAP* **11**, 027 (2019), [arXiv:1906.00997 \[astro-ph.CO\]](#).
- [18] G. Cabass, M. M. Ivanov, O. H. E. Philcox, M. Simonović, and M. Zaldarriaga, (2022), [arXiv:2201.07238 \[astro-ph.CO\]](#).
- [19] G. Cabass, M. M. Ivanov, O. H. E. Philcox, M. Simonović, and M. Zaldarriaga, (2022), [arXiv:2204.01781 \[astro-ph.CO\]](#).
- [20] G. Cabass, M. M. Ivanov, O. H. E. Philcox, M. Simonovic, and M. Zaldarriaga, (2022), [arXiv:2211.14899 \[astro-ph.CO\]](#).
- [21] S. McAlpine *et al.*, *Astron. Comput.* **15**, 72 (2016), [arXiv:1510.01320 \[astro-ph.GA\]](#).
- [22] V. Springel *et al.*, *Mon. Not. Roy. Astron. Soc.* **475**, 676 (2018), [arXiv:1707.03397 \[astro-ph.GA\]](#).
- [23] C. Hernández-Aguayo *et al.*, *Mon. Not. Roy. Astron. Soc.* **524**, 2556 (2023), [arXiv:2210.10059 \[astro-ph.CO\]](#).
- [24] R. H. Wechsler and J. L. Tinker, *Ann. Rev. Astron. Astrophys.* **56**, 435 (2018), [arXiv:1804.03097 \[astro-ph.GA\]](#).
- [25] A. A. Berlind and D. H. Weinberg, *Astrophys. J.* **575**, 587 (2002), [arXiv:astro-ph/0109001](#).
- [26] A. V. Kravtsov, A. A. Berlind, R. H. Wechsler, A. A. Klypin, S. Gottloeber, B. Allgood, and J. R. Primack, *Astrophys. J.* **609**, 35 (2004), [arXiv:astro-ph/0308519](#).
- [27] Z. Zheng, A. A. Berlind, D. H. Weinberg, A. J. Benson, C. M. Baugh, S. Cole, R. Dave, C. S. Frenk, N. Katz, and C. G. Lacey, *Astrophys. J.* **633**, 791 (2005), [arXiv:astro-ph/0408564](#).
- [28] A. P. Hearin, A. R. Zentner, F. C. van den Bosch, D. Campbell, and E. Tollerud, *Mon. Not. Roy. Astron. Soc.* **460**, 2552 (2016), [arXiv:1512.03050 \[astro-ph.CO\]](#).
- [29] E. Krause *et al.* (Beyond-2pt), (2024), [arXiv:2405.02252 \[astro-ph.CO\]](#).
- [30] Y. Kobayashi, T. Nishimichi, M. Takada, and H. Miyatake, *Phys. Rev. D* **105**, 083517 (2022), [arXiv:2110.06969 \[astro-ph.CO\]](#).
- [31] C. Cuesta-Lazaro *et al.*, (2023), [arXiv:2309.16539 \[astro-ph.CO\]](#).
- [32] G. Valogiannis, S. Yuan, and C. Dvorkin, *Phys. Rev. D* **109**, 103503 (2024), [arXiv:2310.16116 \[astro-ph.CO\]](#).
- [33] C. Hahn, M. Eickenberg, S. Ho, J. Hou, P. Lemos, E. Massara, C. Modi, A. Moradinezhad Dizgah, L. Parker, and B. R.-S. Blancard, (2023), [arXiv:2310.15243 \[astro-ph.CO\]](#).
- [34] J. Hou, A. Moradinezhad Dizgah, C. Hahn, M. Eickenberg, S. Ho, P. Lemos, E. Massara, C. Modi, L. Parker, and B. R.-S. Blancard, *Phys. Rev. D* **109**, 103528 (2024), [arXiv:2401.15074 \[astro-ph.CO\]](#).

BOSS P_ℓ with conservative priors					BOSS P_ℓ with simulation-based priors				
Param	best-fit	mean $\pm\sigma$	95% lower	95% upper	Param	best-fit	mean $\pm\sigma$	95% lower	95% upper
ω_{cdm}	0.1162	0.1152 $^{+0.0076}_{-0.0092}$	0.09881	0.1321	ω_{cdm}	0.1184	0.1225 \pm 0.0071	0.1108	0.1366
H_0	72.76	71.19 $^{+3.4}_{-3.4}$	64.38	78	H_0	67.73	69.4 $^{+3.0}_{-3.5}$	63.35	76.11
$\ln(10^{10} A_s)$	2.791	2.74 $^{+0.15}_{-0.16}$	2.43	3.045	$\ln(10^{10} A_s)$	2.59	2.61 $^{+0.11}_{-0.13}$	2.378	2.863
$b_1^{(1)}$	2.138	2.252 $^{+0.19}_{-0.21}$	1.864	2.652	$b_1^{(1)}$	2.566	2.521 $^{+0.2}_{-0.11}$	2.378	2.863
$b_2^{(1)}$	0.3709	-0.1467 $^{+1}_{-1}$	-2.161	1.879	$b_2^{(1)}$	0.05728	0.4491 $^{+0.27}_{-0.39}$	-0.1404	1.108
$b_{\mathcal{G}_2}^{(1)}$	-0.05285	-0.3078 $^{+0.62}_{-0.56}$	-1.506	0.8285	$b_{\mathcal{G}_2}^{(1)}$	-0.905	-0.8697 $^{+0.22}_{-0.32}$	-1.412	-0.2802
$b_1^{(2)}$	2.314	2.453 $^{+0.2}_{-0.23}$	2.032	2.883	$b_1^{(2)}$	2.772	2.672 $^{+0.18}_{-0.12}$	2.329	2.945
$b_2^{(2)}$	0.03068	-0.02749 $^{+1}_{-1}$	-1.976	1.952	$b_2^{(2)}$	0.4222	0.5347 $^{+0.21}_{-0.27}$	0.09803	0.9904
$b_{\mathcal{G}_2}^{(2)}$	0.2339	-0.007196 $^{+0.65}_{-0.63}$	-1.275	1.261	$b_{\mathcal{G}_2}^{(2)}$	-1.083	-1.014 $^{+0.17}_{-0.25}$	-1.454	-0.5176
$b_1^{(3)}$	2.066	2.173 $^{+0.18}_{-0.2}$	1.806	2.555	$b_1^{(3)}$	2.471	2.409 $^{+0.16}_{-0.11}$	2.074	2.650
$b_2^{(3)}$	-0.06066	0.3916 $^{+0.94}_{-0.94}$	-1.443	2.258	$b_2^{(3)}$	0.06239	0.1654 $^{+0.17}_{-0.31}$	-0.248	0.839
$b_{\mathcal{G}_2}^{(3)}$	-0.5721	-0.5128 $^{+0.55}_{-0.5}$	-1.563	0.5285	$b_{\mathcal{G}_2}^{(3)}$	-0.7845	-0.7237 $^{+0.16}_{-0.2}$	-1.096	-0.308
$b_1^{(4)}$	2.173	2.266 $^{+0.18}_{-0.21}$	1.877	2.666	$b_1^{(4)}$	2.498	2.417 $^{+0.16}_{-0.11}$	2.102	2.658
$b_2^{(4)}$	0.009038	0.01678 $^{+1}_{-1}$	-1.948	1.985	$b_2^{(4)}$	0.07228	0.2367 $^{+0.18}_{-0.29}$	-0.1902	0.7457
$b_{\mathcal{G}_2}^{(4)}$	-0.1313	0.1145 $^{+0.56}_{-0.55}$	-0.9952	1.238	$b_{\mathcal{G}_2}^{(4)}$	-0.8219	-0.7656 $^{+0.18}_{-0.19}$	-1.131	-0.3997
Ω_m	0.2619	0.273 $^{+0.022}_{-0.033}$	0.2199	0.3315	Ω_m	0.3069	0.301 \pm 0.021	0.2610	0.3419
σ_8	0.7223	0.6967 $^{+0.044}_{-0.055}$	0.6002	0.7966	σ_8	0.651	0.677 $^{+0.033}_{-0.039}$	0.6071	0.7507

TABLE IV. Same as table III but for $k_{\max} = 0.1 h\text{Mpc}^{-1}$.

- [35] J. M. Sullivan, U. Seljak, and S. Singh, *JCAP* **11**, 026 (2021), [arXiv:2104.10676 \[astro-ph.CO\]](#).
- [36] M. M. Ivanov, C. Cuesta-Lazaro, S. Mishra-Sharma, A. Obuljen, and M. W. Toomey, (2024), [arXiv:2402.13310 \[astro-ph.CO\]](#).
- [37] G. Cabass, O. H. E. Philcox, M. M. Ivanov, K. Akitsu, S.-F. Chen, M. Simonović, and M. Zaldarriaga, (2024), [arXiv:2404.01894 \[astro-ph.CO\]](#).
- [38] A. Obuljen, M. Simonović, A. Schneider, and R. Feldmann, *Phys. Rev. D* **108**, 083528 (2023), [arXiv:2207.12398 \[astro-ph.CO\]](#).
- [39] C. Modi and O. H. E. Philcox, (2023), [arXiv:2309.10270 \[astro-ph.CO\]](#).
- [40] C. Modi, S.-F. Chen, and M. White, *Mon. Not. Roy. Astron. Soc.* **492**, 5754 (2020), [arXiv:1910.07097 \[astro-ph.CO\]](#).
- [41] N. Kokron, J. DeRose, S.-F. Chen, M. White, and R. H. Wechsler, *Mon. Not. Roy. Astron. Soc.* **505**, 1422 (2021), [arXiv:2101.11014 \[astro-ph.CO\]](#).
- [42] M. Pellejero-Ibanez, R. E. Angulo, M. Zennaro, J. Stuecker, S. Contreras, G. Arico, and F. Maion, *Mon. Not. Roy. Astron. Soc.* **520**, 3725 (2023), [arXiv:2207.06437 \[astro-ph.CO\]](#).
- [43] D. Baradaran, B. Hadzhiyska, M. J. White, and N. Sailer, (2024), [arXiv:2406.13079 \[astro-ph.CO\]](#).
- [44] N. Kokron, J. DeRose, S.-F. Chen, M. White, and R. H. Wechsler, *Mon. Not. Roy. Astron. Soc.* **514**, 2198 (2022), [arXiv:2112.00012 \[astro-ph.CO\]](#).
- [45] J. F. Donoghue, E. Golowich, and B. R. Holstein, *Dynamics of the Standard Model*, 2nd ed., Cambridge Monographs on Particle Physics, Nuclear Physics and Cosmology (Cambridge University Press, 2023).
- [46] J. F. Donoghue, M. M. Ivanov, and A. Shkerin, (2017), [arXiv:1702.00319 \[hep-th\]](#).
- [47] S. Park, R. Gupta, B. Yoon, S. Mondal, T. Bhattacharya, Y.-C. Jang, B. Joó, and F. Winter (Nucleon Matrix Elements (NME)), *Phys. Rev. D* **105**, 054505 (2022), [arXiv:2103.05599 \[hep-lat\]](#).
- [48] R. Abbott, W. Detmold, M. Illa, A. Parreño, R. J. Perry, F. Romero-López, P. E. Shanahan, and M. L. Wagman, (2024), [arXiv:2406.09273 \[hep-lat\]](#).
- [49] R. Abbott, W. Detmold, F. Romero-López, Z. Davoudi, M. Illa, A. Parreño, R. J. Perry, P. E. Shanahan, and M. L. Wagman (NPLQCD), *Phys. Rev. D* **108**, 114506 (2023), [arXiv:2307.15014 \[hep-lat\]](#).

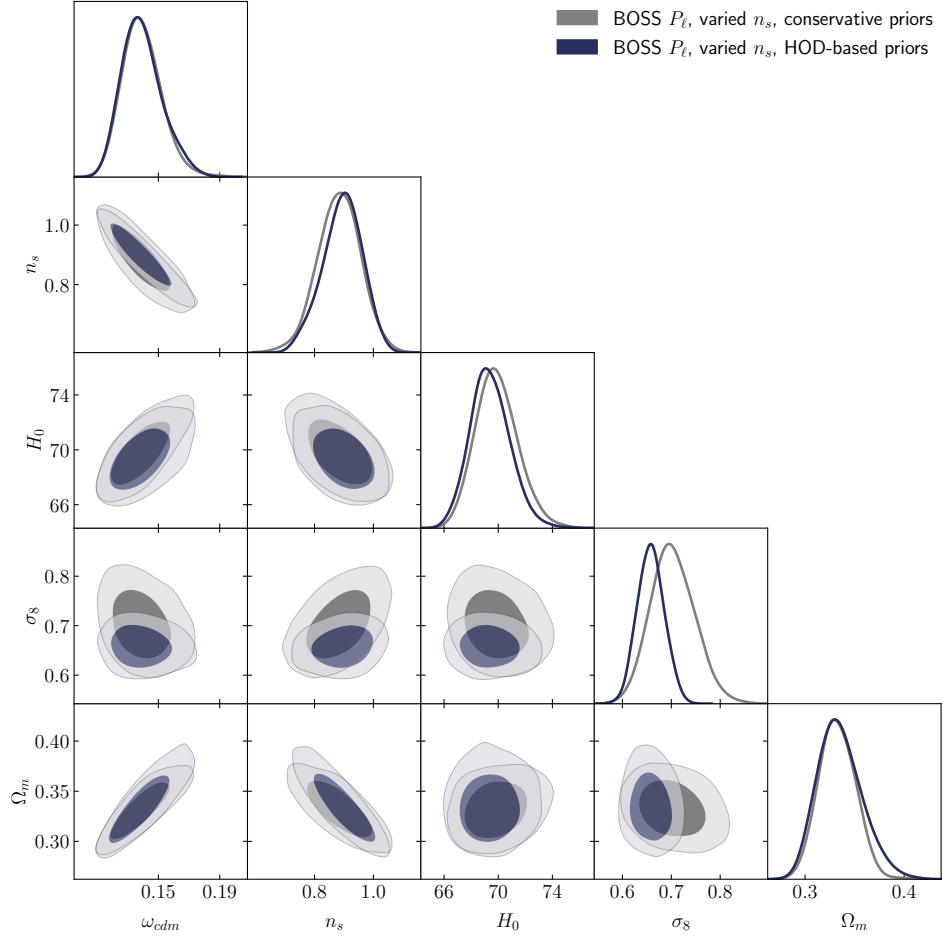


FIG. 23. Same as fig. 2, but with the varied primordial spectral tilt n_s .

- [50] Y. He and M. Kruczenski, (2023), [arXiv:2309.12402](#) [hep-th].
- [51] Y. He and M. Kruczenski, (2024), [arXiv:2403.10772](#) [hep-th].
- [52] Y. Akrami *et al.* (Planck), *Astron. Astrophys.* **641**, A9 (2020), [arXiv:1905.05697](#) [astro-ph.CO].
- [53] A. Moradinezhad Dizgah, M. Biagetti, E. Sefusatti, V. Desjacques, and J. Noreña, *JCAP* **05**, 015 (2021), [arXiv:2010.14523](#) [astro-ph.CO].
- [54] S. Alam *et al.* (BOSS), *Mon. Not. Roy. Astron. Soc.* **470**, 2617 (2017), [arXiv:1607.03155](#) [astro-ph.CO].
- [55] S. Yuan, L. H. Garrison, D. J. Eisenstein, and R. H. Wechsler, *Mon. Not. Roy. Astron. Soc.* **515**, 871 (2022), [arXiv:2203.11963](#) [astro-ph.CO].
- [56] S.-F. Chen, M. White, J. DeRose, and N. Kokron, *JCAP* **07**, 041 (2022), [arXiv:2204.10392](#) [astro-ph.CO].
- [57] J. U. Lange, A. P. Hearin, A. Leauthaud, F. C. van den Bosch, E. Xhakaj, H. Guo, R. H. Wechsler, and J. DeRose, (2023), [10.1093/mnras/stad473](#), [arXiv:2301.08692](#) [astro-ph.CO].
- [58] M. M. Ivanov, O. H. E. Philcox, G. Cabass, T. Nishimichi, M. Simonović, and M. Zaldarriaga, *Phys. Rev. D* **107**, 083515 (2023), [arXiv:2302.04414](#) [astro-ph.CO].
- [59] M. P. Ibáñez, R. E. Angulo, and J. A. Peacock, (2024), [arXiv:2407.07949](#) [astro-ph.CO].
- [60] E. Paillas *et al.*, (2023), [arXiv:2309.16541](#) [astro-ph.CO].
- [61] N. Sailer *et al.*, (2024), [arXiv:2407.04607](#) [astro-ph.CO].
- [62] S. Chen *et al.*, (2024), [arXiv:2407.04795](#) [astro-ph.CO].
- [63] M. Schmittfull, M. Simonović, V. Assassi, and M. Zaldarriaga, *Phys. Rev. D* **100**, 043514 (2019), [arXiv:1811.10640](#) [astro-ph.CO].
- [64] M. Schmittfull, M. Simonović, M. M. Ivanov, O. H. E. Philcox, and M. Zaldarriaga, *JCAP* **05**, 059 (2021), [arXiv:2012.03334](#) [astro-ph.CO].
- [65] S. Foreman, A. Obuljen, and M. Simonović, (2024), [arXiv:2405.18559](#) [astro-ph.CO].
- [66] M. Schmittfull, T. Baldauf, and U. Seljak, *Phys. Rev. D* **91**, 043530 (2015), [arXiv:1411.6595](#) [astro-ph.CO].

BOSS P_ℓ with conservative priors					BOSS P_ℓ with simulation-based priors				
Param	best-fit	mean $\pm\sigma$	95% lower	95% upper	Param	best-fit	mean $\pm\sigma$	95% lower	95% upper
ω_{cdm}	0.13	$0.1393^{+0.011}_{-0.015}$	0.1138	0.1668	ω_{cdm}	0.1292	$0.1379^{+0.0094}_{-0.014}$	0.116	0.1642
H_0	68.15	$69.89^{+1.5}_{-1.7}$	66.71	73.19	H_0	68.49	$69.36^{+1.4}_{-1.6}$	66.44	72.34
$\ln(10^{10} A_s)$	2.788	$2.631^{+0.15}_{-0.16}$	2.312	2.954	$\ln(10^{10} A_s)$	2.574	$2.475^{+0.11}_{-0.11}$	2.262	2.699
n_s	0.9271	$0.8834^{+0.076}_{-0.072}$	0.7337	1.035	n_s	0.9641	$0.9029^{+0.075}_{-0.052}$	0.7652	1.014
$b_1^{(1)}$	2.234	$2.355^{+0.16}_{-0.17}$	2.02	2.689	$b_1^{(1)}$	2.609	$2.649^{+0.12}_{-0.12}$	2.412	2.877
$b_2^{(1)}$	-0.6257	$-1.155^{+0.96}_{-1}$	-3.109	0.8529	$b_2^{(1)}$	0.6053	$0.8918^{+0.22}_{-0.35}$	0.3547	1.51
$b_{\mathcal{G}_2}^{(1)}$	-0.005441	$-0.1835^{+0.53}_{-0.5}$	-1.231	0.8589	$b_{\mathcal{G}_2}^{(1)}$	-0.8512	$-0.7847^{+0.23}_{-0.39}$	-1.363	-0.0856
$b_1^{(2)}$	2.361	$2.491^{+0.16}_{-0.17}$	2.163	2.821	$b_1^{(2)}$	2.688	$2.75^{+0.13}_{-0.13}$	2.503	2.995
$b_2^{(2)}$	-0.154	$0.00792^{+0.96}_{-0.98}$	-1.905	1.942	$b_2^{(2)}$	0.759	$0.9353^{+0.23}_{-0.34}$	0.3907	1.528
$b_{\mathcal{G}_2}^{(2)}$	-0.07998	$-0.2719^{+0.54}_{-0.51}$	-1.337	0.77	$b_{\mathcal{G}_2}^{(2)}$	-0.9797	$-1.044^{+0.19}_{-0.29}$	-1.531	-0.4928
$b_1^{(3)}$	2.164	$2.247^{+0.14}_{-0.15}$	1.956	2.545	$b_1^{(3)}$	2.39	$2.451^{+0.11}_{-0.11}$	2.237	2.669
$b_2^{(3)}$	-0.4313	$-0.3574^{+0.84}_{-0.9}$	-2.078	1.404	$b_2^{(3)}$	0.4266	$0.5404^{+0.16}_{-0.22}$	0.1692	0.9514
$b_{\mathcal{G}_2}^{(3)}$	-0.2832	$-0.2694^{+0.43}_{-0.41}$	-1.127	0.5689	$b_{\mathcal{G}_2}^{(3)}$	-0.8925	$-0.8974^{+0.16}_{-0.29}$	-1.371	-0.346
$b_1^{(4)}$	2.201	$2.273^{+0.14}_{-0.15}$	1.985	2.574	$b_1^{(4)}$	2.423	$2.451^{+0.11}_{-0.11}$	2.236	2.668
$b_2^{(4)}$	0.1618	$-0.1207^{+0.87}_{-0.93}$	-1.879	1.685	$b_2^{(4)}$	0.4614	$0.5707^{+0.17}_{-0.22}$	0.1977	0.9661
$b_{\mathcal{G}_2}^{(4)}$	0.1992	$0.2019^{+0.43}_{-0.44}$	-0.6637	1.073	$b_{\mathcal{G}_2}^{(4)}$	-1.02	$-0.9687^{+0.19}_{-0.29}$	-1.433	-0.4442
Ω_m	0.3298	$0.3325^{+0.019}_{-0.02}$	0.2953	0.3704	Ω_m	0.323	$0.3331^{+0.017}_{-0.025}$	0.2932	0.3815
σ_8	0.7403	$0.7036^{+0.044}_{-0.049}$	0.6119	0.7972	σ_8	0.6831	$0.6604^{+0.026}_{-0.03}$	0.6084	0.715

TABLE V. Same as table III but with the varied tilt of the primordial scalar fluctuations n_s .

- [67] T. Lazeyras and F. Schmidt, *JCAP* **1809**, 008 (2018), [arXiv:1712.07531 \[astro-ph.CO\]](#).
- [68] M. M. Abidi and T. Baldauf, *JCAP* **1807**, 029 (2018), [arXiv:1802.07622 \[astro-ph.CO\]](#).
- [69] F. Schmidt, F. Elsner, J. Jasche, N. M. Nguyen, and G. Lavaux, *JCAP* **01**, 042 (2019), [arXiv:1808.02002 \[astro-ph.CO\]](#).
- [70] F. Elsner, F. Schmidt, J. Jasche, G. Lavaux, and N.-M. Nguyen, *JCAP* **01**, 029 (2020), [arXiv:1906.07143 \[astro-ph.CO\]](#).
- [71] G. Cabass and F. Schmidt, *JCAP* **04**, 042 (2020), [arXiv:1909.04022 \[astro-ph.CO\]](#).
- [72] F. Schmidt, (2020), [arXiv:2009.14176 \[astro-ph.CO\]](#).
- [73] F. Schmidt, G. Cabass, J. Jasche, and G. Lavaux, *JCAP* **11**, 008 (2020), [arXiv:2004.06707 \[astro-ph.CO\]](#).
- [74] T. Lazeyras, A. Barreira, and F. Schmidt, *JCAP* **10**, 063 (2021), [arXiv:2106.14713 \[astro-ph.CO\]](#).
- [75] J. Stadler, F. Schmidt, and M. Reinecke, *JCAP* **10**, 069 (2023), [arXiv:2303.09876 \[astro-ph.CO\]](#).
- [76] N.-M. Nguyen, F. Schmidt, B. Tucci, M. Reinecke, and A. Kostić, (2024), [arXiv:2403.03220 \[astro-ph.CO\]](#).
- [77] A. Chudaykin, M. M. Ivanov, O. H. E. Philcox, and M. Simonović, *Phys. Rev. D* **102**, 063533 (2020), [arXiv:2004.10607 \[astro-ph.CO\]](#).
- [78] D. Blas, M. Garny, M. M. Ivanov, and S. Sibiryakov, *JCAP* **1607**, 052 (2016), [arXiv:1512.05807 \[astro-ph.CO\]](#).
- [79] D. Blas, M. Garny, M. M. Ivanov, and S. Sibiryakov, *JCAP* **1607**, 028 (2016), [arXiv:1605.02149 \[astro-ph.CO\]](#).
- [80] M. M. Ivanov and S. Sibiryakov, *JCAP* **1807**, 053 (2018), [arXiv:1804.05080 \[astro-ph.CO\]](#).
- [81] A. Vasudevan, M. M. Ivanov, S. Sibiryakov, and J. Lesgourgues, *JCAP* **09**, 037 (2019), [arXiv:1906.08697 \[astro-ph.CO\]](#).
- [82] M. Crocce and R. Scoccimarro, *Phys. Rev. D* **77**, 023533 (2008), [arXiv:0704.2783 \[astro-ph\]](#).
- [83] L. Senatore and M. Zaldarriaga, *JCAP* **1502**, 013 (2015), [arXiv:1404.5954 \[astro-ph.CO\]](#).
- [84] T. Baldauf, M. Mirbabayi, M. Simonović, and M. Zaldarriaga, *Phys. Rev. D* **92**, 043514 (2015), [arXiv:1504.04366 \[astro-ph.CO\]](#).

- [85] M. Simonovic, T. Baldauf, M. Zaldarriaga, J. J. Carrasco, and J. A. Kollmeier, *JCAP* **1804**, 030 (2018), [arXiv:1708.08130 \[astro-ph.CO\]](#).
- [86] F. Villaescusa-Navarro *et al.*, *Astrophys. J. Suppl.* **250**, 2 (2020), [arXiv:1909.05273 \[astro-ph.CO\]](#).
- [87] U. Seljak, *Mon. Not. Roy. Astron. Soc.* **318**, 203 (2000), [arXiv:astro-ph/0001493](#).
- [88] A. Cooray and R. K. Sheth, *Phys. Rept.* **372**, 1 (2002), [arXiv:astro-ph/0206508](#).
- [89] T. Nishimichi, G. D'Amico, M. M. Ivanov, L. Senatore, M. Simonović, M. Takada, M. Zaldarriaga, and P. Zhang, *Phys. Rev. D* **102**, 123541 (2020), [arXiv:2003.08277 \[astro-ph.CO\]](#).
- [90] A. Chudaykin, K. Dolgikh, and M. M. Ivanov, *Phys. Rev. D* **103**, 023507 (2021), [arXiv:2009.10106 \[astro-ph.CO\]](#).
- [91] M. M. Ivanov, E. McDonough, J. C. Hill, M. Simonović, M. W. Toomey, S. Alexander, and M. Zaldarriaga, *Phys. Rev. D* **102**, 103502 (2020), [arXiv:2006.11235 \[astro-ph.CO\]](#).
- [92] A. He, M. M. Ivanov, R. An, and V. Gluscevic, *Astrophys. J. Lett.* **954**, L8 (2023), [arXiv:2301.08260 \[astro-ph.CO\]](#).
- [93] D. Camarena, F.-Y. Cyr-Racine, and J. Houghteling, *Phys. Rev. D* **108**, 103535 (2023), [arXiv:2309.03941 \[astro-ph.CO\]](#).
- [94] A. He, R. An, M. M. Ivanov, and V. Gluscevic, *Phys. Rev. D* **109**, 103527 (2024), [arXiv:2309.03956 \[astro-ph.CO\]](#).
- [95] A. Chudaykin and M. M. Ivanov, *JCAP* **11**, 034 (2019), [arXiv:1907.06666 \[astro-ph.CO\]](#).
- [96] K. K. Rogers, R. Hložek, A. Laguë, M. M. Ivanov, O. H. E. Philcox, G. Cabass, K. Akitsu, and D. J. E. Marsh, *JCAP* **06**, 023 (2023), [arXiv:2301.08361 \[astro-ph.CO\]](#).
- [97] W. L. Xu, J. B. Muñoz, and C. Dvorkin, *Phys. Rev. D* **105**, 095029 (2022), [arXiv:2107.09664 \[astro-ph.CO\]](#).
- [98] M. M. Ivanov, M. Simonović, and M. Zaldarriaga, *JCAP* **05**, 042 (2020), [arXiv:1909.05277 \[astro-ph.CO\]](#).
- [99] A. Chudaykin, M. M. Ivanov, and M. Simonović, *Phys. Rev. D* **103**, 043525 (2021), [arXiv:2009.10724 \[astro-ph.CO\]](#).
- [100] N. Aghanim *et al.* (Planck), *Astron. Astrophys.* **607**, A95 (2017), [arXiv:1608.02487 \[astro-ph.CO\]](#).
- [101] S.-F. Chen, Z. Vlah, and M. White, *JCAP* **07**, 062 (2020), [arXiv:2005.00523 \[astro-ph.CO\]](#).
- [102] S.-F. Chen, Z. Vlah, E. Castorina, and M. White, *JCAP* **03**, 100 (2021), [arXiv:2012.04636 \[astro-ph.CO\]](#).
- [103] G. D'Amico, L. Senatore, and P. Zhang, *JCAP* **01**, 006 (2021), [arXiv:2003.07956 \[astro-ph.CO\]](#).
- [104] P. A. R. Ade *et al.* (Planck), *Astron. Astrophys.* **594**, A13 (2016), [arXiv:1502.01589 \[astro-ph.CO\]](#).
- [105] N. A. Maksimova, L. H. Garrison, D. J. Eisenstein, B. Hadzhiyska, S. Bose, and T. P. Satterthwaite, *Mon. Not. Roy. Astron. Soc.* **508**, 4017 (2021), [arXiv:2110.11398 \[astro-ph.CO\]](#).
- [106] N. Aghanim *et al.* (Planck), (2018), [arXiv:1807.06209 \[astro-ph.CO\]](#).
- [107] B. Hadzhiyska, D. Eisenstein, S. Bose, L. H. Garrison, and N. Maksimova, *Mon. Not. Roy. Astron. Soc.* **509**, 501 (2021), [arXiv:2110.11408 \[astro-ph.CO\]](#).
- [108] V. Assassi, D. Baumann, D. Green, and M. Zaldarriaga, *JCAP* **1408**, 056 (2014), [arXiv:1402.5916 \[astro-ph.CO\]](#).
- [109] V. Desjacques, D. Jeong, and F. Schmidt, *Phys. Rept.* **733**, 1 (2018), [arXiv:1611.09787 \[astro-ph.CO\]](#).
- [110] A. Perko, L. Senatore, E. Jennings, and R. H. Wechsler, (2016), [arXiv:1610.09321 \[astro-ph.CO\]](#).
- [111] F. Bernardeau, S. Colombi, E. Gaztanaga, and R. Scoccimarro, *Phys. Rept.* **367**, 1 (2002), [arXiv:astro-ph/0112551 \[astro-ph\]](#).
- [112] D. Blas, M. Garny, and T. Konstandin, *JCAP* **09**, 024 (2013), [arXiv:1304.1546 \[astro-ph.CO\]](#).
- [113] R. Scoccimarro and J. Frieman, *Astrophys. J. Suppl.* **105**, 37 (1996), [arXiv:astro-ph/9509047](#).
- [114] R. Scoccimarro and J. Frieman, *Astrophys. J.* **473**, 620 (1996), [arXiv:astro-ph/9602070](#).
- [115] L. Senatore and M. Zaldarriaga, (2014), [arXiv:1409.1225 \[astro-ph.CO\]](#).
- [116] M. M. Ivanov, O. H. E. Philcox, M. Simonović, M. Zaldarriaga, T. Nishimichi, and M. Takada, *Phys. Rev. D* **105**, 043531 (2022), [arXiv:2110.00006 \[astro-ph.CO\]](#).
- [117] P. Taule and M. Garny, *JCAP* **11**, 078 (2023), [arXiv:2308.07379 \[astro-ph.CO\]](#).
- [118] N. Hand, Y. Feng, F. Beutler, Y. Li, C. Modi, U. Seljak, and Z. Slepian, *Astron. J.* **156**, 160 (2018), [arXiv:1712.05834 \[astro-ph.IM\]](#).
- [119] J. C. Jackson, *Mon. Not. Roy. Astron. Soc.* **156**, 1P (1972), [arXiv:0810.3908 \[astro-ph\]](#).
- [120] A. J. Benson, S. Cole, C. S. Frenk, C. M. Baugh, and C. G. Lacey, *Mon. Not. Roy. Astron. Soc.* **311**, 793 (2000), [arXiv:astro-ph/9903343](#).
- [121] W. H. Press and P. Schechter, *Astrophys. J.* **187**, 425 (1974).
- [122] M. M. Ivanov, A. A. Kaurov, and S. Sibiryakov, *JCAP* **1903**, 009 (2019), [arXiv:1811.07913 \[astro-ph.CO\]](#).
- [123] R. K. Sheth and G. Tormen, *Mon. Not. Roy. Astron. Soc.* **308**, 119 (1999), [arXiv:astro-ph/9901122](#).
- [124] J. L. Tinker, A. V. Kravtsov, A. Klypin, K. Abazajian, M. S. Warren, G. Yepes, S. Gottlober, and D. E. Holz, *Astrophys. J.* **688**, 709 (2008), [arXiv:0803.2706 \[astro-ph.CO\]](#).

- ph].
- [125] T. Lazeyras, C. Wagner, T. Baldauf, and F. Schmidt, *JCAP* **1602**, 018 (2016), arXiv:1511.01096 [astro-ph.CO].
- [126] T. Baldauf, U. Seljak, R. E. Smith, N. Hamaus, and V. Desjacques, *Phys. Rev. D* **88**, 083507 (2013), arXiv:1305.2917 [astro-ph.CO].
- [127] Y. Li and R. E. Smith, (2024), arXiv:2411.18722 [astro-ph.CO].
- [128] S. Yuan, L. H. Garrison, B. Hadzhiyska, S. Bose, and D. J. Eisenstein, *Mon. Not. Roy. Astron. Soc.* **510**, 3301 (2022), arXiv:2110.11412 [astro-ph.CO].
- [129] M. M. Ivanov *et al.*, (2024), arXiv:2412.01888 [astro-ph.CO].
- [130] B. Reid *et al.*, *Mon. Not. Roy. Astron. Soc.* **455**, 1553 (2016), arXiv:1509.06529 [astro-ph.CO].
- [131] A. G. Adame *et al.* (DESI), *JCAP* **02**, 021 (2025), arXiv:2404.03002 [astro-ph.CO].
- [132] R. Casas-Miranda, H. J. Mo, R. K. Sheth, and G. Boerner, *Mon. Not. Roy. Astron. Soc.* **333**, 730 (2002), arXiv:astro-ph/0105008.
- [133] G. Papamakarios, T. Pavlakou, and I. Murray, “Masked autoregressive flow for density estimation,” (2018), arXiv:1705.07057 [stat.ML].
- [134] A. Paszke, S. Gross, F. Massa, A. Lerer, J. Bradbury, G. Chanan, T. Killeen, Z. Lin, N. Gimelshein, L. Antiga, *et al.*, *Advances in neural information processing systems* **32** (2019).
- [135] C. Hahn, R. Scoccimarro, M. R. Blanton, J. L. Tinker, and S. A. Rodríguez-Torres, *Mon. Not. Roy. Astron. Soc.* **467**, 1940 (2017), arXiv:1609.01714 [astro-ph.CO].
- [136] M. M. Ivanov, (2021), arXiv:2106.12580 [astro-ph.CO].
- [137] A. Chudaykin and M. M. Ivanov, (2022), arXiv:2210.17044 [astro-ph.CO].
- [138] M. M. Ivanov, O. H. E. Philcox, T. Nishimichi, M. Simonović, M. Takada, and M. Zaldarriaga, *Phys. Rev. D* **105**, 063512 (2022), arXiv:2110.10161 [astro-ph.CO].
- [139] O. H. E. Philcox, M. M. Ivanov, G. Cabass, M. Simonović, M. Zaldarriaga, and T. Nishimichi, *Phys. Rev. D* **106**, 043530 (2022), arXiv:2206.02800 [astro-ph.CO].
- [140] F. Beutler *et al.* (BOSS), *Mon. Not. Roy. Astron. Soc.* **466**, 2242 (2017), arXiv:1607.03150 [astro-ph.CO].
- [141] O. H. E. Philcox, *Phys. Rev. D* **103**, 103504 (2021), arXiv:2012.09389 [astro-ph.CO].
- [142] O. H. E. Philcox, (2021), arXiv:2107.06287 [astro-ph.CO].
- [143] O. H. E. Philcox, M. M. Ivanov, M. Simonović, and M. Zaldarriaga, *JCAP* **05**, 032 (2020), arXiv:2002.04035 [astro-ph.CO].
- [144] D. Wadekar, M. M. Ivanov, and R. Scoccimarro, *Phys. Rev. D* **102**, 123521 (2020), arXiv:2009.00622 [astro-ph.CO].
- [145] J. U. Lange, A. P. Hearin, A. Leauthaud, F. C. van den Bosch, H. Guo, and J. DeRose, *Mon. Not. Roy. Astron. Soc.* **509**, 1779 (2021), arXiv:2101.12261 [astro-ph.CO].
- [146] A. de Mattia *et al.*, *Mon. Not. Roy. Astron. Soc.* **501**, 5616 (2021), arXiv:2007.09008 [astro-ph.CO].
- [147] R. Neveux *et al.* (eBOSS), *Mon. Not. Roy. Astron. Soc.* **499**, 210 (2020), arXiv:2007.08999 [astro-ph.CO].
- [148] V. Desjacques, D. Jeong, and F. Schmidt, *JCAP* **1812**, 035 (2018), arXiv:1806.04015 [astro-ph.CO].
- [149] M. M. Ivanov, *Phys. Rev. D* **109**, 023507 (2024), arXiv:2309.10133 [astro-ph.CO].
- [150] M. M. Ivanov, M. W. Toomey, and N. G. Karaçaylı, (2024), arXiv:2405.13208 [astro-ph.CO].
- [151] T. Baldauf, E. Schaan, and M. Zaldarriaga, *JCAP* **03**, 007 (2016), arXiv:1507.02255 [astro-ph.CO].
- [152] O. H. E. Philcox, B. D. Sherwin, G. S. Farren, and E. J. Baxter, *Phys. Rev. D* **103**, 023538 (2021), arXiv:2008.08084 [astro-ph.CO].